Competition of magnetic and superconducting ordering in one–dimensional generalized Hubbard models

Inaugural-Dissertation

zur

Erlangung des Doktorgrades

der Mathematisch-Naturwissenschaftlichen Fakultät

der Universität zu Köln

vorgelegt von

Christian Dziurzik

aus Dramatal (Polen)

Köln 2003

Institut für Theoretische Physik der Universtität zu Köln
Zülpicher Straße 77, 50937 Köln, Germany

Berichterstatter

Prof. Dr. J. Zittartz

Priv.-Doz. Dr. A. Schadschneider

Prof. Dr. E. Müller-Hartmann

Tag der mündlichen Prüfung

11.02.2004

Contents

Preface

The quest to understand the physics of strongly correlated fermion systems belongs to the most challenging and active fields in condensed matter physics. Various experiments on high-temperature superconductors (HTSC), heavy-fermion alloys and organic materials with their often reduced dimensionality have shown that strong interactions are a central ingredient for the understanding of their physical properties.

The aim of condensed matter theory is to understand the macroscopic behaviour of $\sim 10^{23}$ interacting fermion systems, starting from a detailed microsopic description of the individual particles and the way they interact. However, the description is restricted to the theoretical models that capture all the necessary ingredients to discuss the physical behaviour one seeks to understand.

Historically, the theoretical basis for understanding the behaviour of electrons in solids is based on Landau's *Fermi-liquid theory* in which the electrons are expressed in terms of *quasi-particles*, describing single particle excitations of the non-interacting system, and in addition in terms of collective excitations. However, in some new metallic systems, such as the HTSC, several anomalous properties have been observed indicating that the Fermi-liquid theory does not provide a suitable description. Apart from the HTSC, this general picture of interacting quasi-particles is known to break down in one-dimensional metallic systems in which the concept of a *Tomonaga-Luttinger liquid* with purely collective excitations obeying Bose rather than Fermi statistics is successfully applied.

Numerous (lattice) models have been developed and studied in order to explain these various manifestations of strongly correlated electron behaviour. The most prominent one is the *Hubbard model*, where the motion of electrons is controlled by the hopping amplitude t, in competition with the on-site Coulomb interaction U. The discovery of the HTSC compounds in 1986 has revitalized the investigation of the Hubbard model, since several mechanisms proposed to explain the HTSC invoke properties of the two-dimensional Hubbard model and probably also some one-dimensional aspects are relevant.

Despite of its simplicity only a few rigorous results exist (in any dimension). Hence it is very constructive to consider the one-dimensional counterpart, because analytical as well as numerical tools are much more elaborated in one dimension. Moreover, quantum fluctuations and collective effects are generically strong in low dimensional systems providing a fascinating and challenging area for theoretical physicists.

A great variety of non-perturbative analytical and numerical techniques for low dimensional correlated systems have been developed, having their strengths and limitations. For instance, the one-dimensional Hubbard model can be solved ex-

actly by the *Bethe ansatz*, but more realistic models including further interactions are no longer integrable. Other techniques like *bosonization* give a reliable description of the physics only in the weak-coupling limit. However, in combination with (exact) numerical tools bosonization becomes a powerful technique.

Due to the rapid evolution of computer technology, a considerable progress in the development of new numerical algorithms has been made. Perhaps the most important one is the *density matrix renormalization group* (DMRG) method which was developed by White in 1992. This numerical technique, which is the main tool of the present thesis, leads to highly accurate results for the low-energy physics of one-dimensional quantum systems. The DMRG algorihm is based on the following simple but effective concept: the ground-state wavefunction as well as the low energy excitations of a large interacting chain are obtained by increasing the lattice size iteratively, starting with a small one that can be diagonalized exactly. The exponentially growing Hilbert space is controlled by a renormalization procedure in which 'less important' degrees of freedom are integrated out.

Motivated by the discovery of *triplet superconductivity* (TS) in Sr_2RuO_4 as well as the coexistence of the TS phase with ferromagnetism in UGe_2, $URhGe$ and $ZrZn2$ and the indication that the quasi-one-dimensional conductors (Bechgaard salts) $(TMTSF)_2ClO_4$ and $(TMTSF)_2PF_6$ under pressure are triplet superconductors we study a rather simple extension of the Hubbard model with transverse (XY-type) anisotropy showing close proximity of triplet superconducting and ferromagnetically ordered phases.

Layout of the Thesis

Chapter 1 starts with an overview of interacting electrons in one dimension based on the concept of a Tomonaga-Luttinger (TL) liquid which is described in the framework of a weak-coupling continuum limit approach. The TL and Luther-Emery (LE) theory of an interacting gas model is used for the interpretation of our numerical results.

Chapter 2 is dedicated to the Hubbard model and its extensions. Starting with the derivation of Hubbard's *tight-binding* approximation of electrons in a Coulomb potential, we summarize basic properties of these lattice models. In one dimension, where the (extended) Hubbard model belongs to the universality class of either a TL liquid or a LE phase, the pure Hubbard model is exactly solvable by the Bethe ansatz. We give an outline of this technique and close with a discussion of some extended versions of the Hubbard model exhibiting 'superconducting' phases, characterized by dominant pair correlations.

Chapter 3 gives a detailed description of White's density matrix renormalization group method and its historical context, beginning with the Lanczos algorithm which is applied within our DMRG routine. After outlining the two types of algorithms and its improvements, we show how to evaluate (fermionic) local expectation values and correlation functions. Finally, the relation to the matrix product ansatz and some extensions of the DMRG method will be disccused.

Chapter 4 presents our numerical results for the Hubbard model with transverse spin-exchange. At first, we reflect the weak-coupling phase diagram using the

bosonization technique and continue with the analysis of our numerical data for the half-filled case confirming the bosonization results. Additionally, we discuss a new phase, which is absent in the weak-coupling investigation, and close this part with a discussion of the phase diagram for the half-filled model. Afterwards, DMRG data for the quarter-filled band are analyzed, as a basis for further studies. **Chapter 5** contains the conclusion of this thesis and gives perspectives for further research on the presented topic.

1. Interacting electrons in 1D

Why are solids in one dimension so special? Already the topology of the Fermi surface which is described by only two discrete points in one dimension and a continuous sphere in more than one dimension indicates that one dimensional interacting systems might behave different. In two and three dimensions the low-energy physics of interacting fermions is well described by the *Fermi liquid* theory developed by Landau [1, 2, 3]. However, in one dimension Landau's theory breaks down and the unusual physical behaviour is characterized by the so-called *Tomonaga-Luttinger liquid*, a name coined by Haldane [4]. The basic model in this context is usually called Tomonaga-Luttinger model [5, 6] and was solved exactly by applying the *bosonization method* [7].

After outlining the collapse of Fermi liquid theory in 1D, the description of the Luttinger liquid as a universality class of gapless one dimensional interacting systems will be the subject of the following sections. In addition, a universality class characterized by a gap in the spin excitation spectrum will be discussed. The corresponding model is called *Luther-Emery* model [8].

1.1. Fermi liquid theory and its breakdown

In Landau's theory the fundamental degrees of freedom of the system are *quasi-particles* which allow a one-to-one correspondence between non-interacting and weakly interacting systems. This is possible because weak interaction in principle does not destroy the Fermi surface, i.e. the shape of the momentum distribution function $n_\sigma(\mathbf{k})$ changes, but the finite discontinuity at the Fermi surface $|\mathbf{k}| = k_F$ remains (cf. with the left-hand side of Fig. 1.1).

This discontinuity can be explained on the microscopic level in terms of Green's functions. In the non-interacting case the one-particle Green's function

$$G_0(\mathbf{k}, \omega) = \frac{1}{\omega + i\delta - \varepsilon_0(\mathbf{k})} \tag{1.1}$$

has a pole on the real axis describing a single-particle excitation with a well defined dispersion $\omega = \varepsilon_0(\mathbf{k})$. Note that the corresponding spectral function is simply a delta-function, i.e. $A_0(\mathbf{k}, \omega) = \delta(\omega - \varepsilon_0(\mathbf{k}))$. However, if interactions are switched on, then the Green's function has the modified form

$$G(\mathbf{k}, \omega) = \frac{1}{\omega + i\delta - \varepsilon_0(\mathbf{k}) - \Sigma(\mathbf{k}, \omega)}, \tag{1.2}$$

where the difference between the non-interacting and interacting Green's functions is expressed through the self-energy $\Sigma(\mathbf{k}, \omega)$ which contains all many-body effects.

Now the single-particle excitations are given by the poles of $G(\mathbf{k}, \omega)$ while the self-energy $\Sigma(\mathbf{k}, \omega)$ provides the damping of these excitations. However, a single solution which is characterized by only one pole with finite residue

$$z_{\mathrm{k}}^{-1} = 1 - \left.\frac{\partial \Sigma}{\partial \omega}\right|_{\omega=0, k=k_F} \leq 1, \tag{1.3}$$

implies a normal Fermi liquid. The amplitude z_{k} gives the magnitude of the discontinuity of the momentum distribution function at the Fermi surface (cf. with the left-hand side of Fig. 1.1). The corresponding Green's function becomes

$$G(\mathbf{k}, \omega) = G_{\mathrm{incoh}}(\mathbf{k}, \omega) + \frac{z_{\mathrm{k}}}{\omega - \varepsilon(\mathbf{k}) + \mathrm{i}/\tau_{\mathrm{k}}}, \tag{1.4}$$

after expanding the self-energy to second order around the Fermi surface. Of course, it is essential that $\Sigma(\mathbf{k}, \omega)$ has an analytic expansion about $\omega = 0$ and $|\mathbf{k}| = k_F$. For long timescales

$$\tau_{\mathrm{k}}^{-1} = -z_{\mathrm{k}} \operatorname{Im} \Sigma(k, \omega = 0) \to 0 \quad (k \to k_F) \tag{1.5}$$

the second term of Eq. (1.4) gives a broadened delta-peak in the spectral function, whereas $G_{\mathrm{incoh}}(\mathbf{k}, \omega)$ corresponds to a smooth *incoherent background*. The damped peak at the energy $\varepsilon(\mathbf{k}) \propto \varepsilon_0(\mathbf{k}) z_{\mathrm{k}}$ expresses the fact that excitations have the character of quasi-particles. The breakdown of the Fermi liquid theory in

Figure 1.1.: The figure shows a qualitative plot of the single-particle momentum distribution function $n_\sigma(k)$ at temperature $T = 0$. Left: finite discontinuity at the Fermi momentum k_F for a system of interacting fermions in more than one dimension (FL: Fermi liquid). Right: absence of a discontinuity in an interacting system in one dimension (TLL: Tomonaga-Luttinger liquid). The dashed lines show the non-interacting case.

1D is signalled by either the appearance of multiple solutions indicated by multiple poles or if $z_{\mathrm{k}} = 0$, manifesting a continuous momentum distribution function, as illustrated in the right-hand side of Fig. 1.1.

1.2. The concept of Tomonaga-Luttinger liquid

In the limit of weakly interacting fermions only states close to the two Fermi points $\pm k_F$ are important. For this reason it is possible to linearize the spectrum

$\varepsilon(k)$ around $\pm k_F$ which is leading to two branches of particles, the *right movers* and the *left movers*. Note that in a simple lattice model (see Sec. 2.1 for details) one would have $\varepsilon(k) = -2t\cos(k)$, where t describes the motion of particles to neighbouring lattice sites. In the continuum-limit theory one then obtains four scattering processes which describe the interaction among these particles. Two scattering processes characterize the Tomonaga-Luttinger (TL) model which can be solved exactly within the framework of the bosonization technique. The determined TL parameters describe the physics of this model. This will be the subject of the following parts.

1.2.1. Free electrons in continuum limit

The microscopic Hamiltonian describing non-interacting electrons has the well-known form

$$\mathcal{H}_0 = \sum_{k,\sigma} \varepsilon(k) c_{k,\sigma}^\dagger c_{k,\sigma} \,, \tag{1.6}$$

where $c_{k,\sigma}$ and $c_{k,\sigma}^\dagger$ are the standard annihilation and creation operators for an electron with momentum k and spin $\sigma = \{\uparrow, \downarrow\}$, expressed in second quantization. The summation over k is limited to the first Brillouin zone $[-\pi/a_0, \pi/a_0]$, where a_0 is the lattice spacing. Note that each momentum state k can be filled by two electrons of opposite spins (Pauli principle), thus $k = 2\pi/L \times n$ with $n = 0, \pm 1, \pm 2 \ldots, \pm(L/2 - 1), L/2$ has to be used (here with $a_0 = 1$). The quantity L is the total number of lattice sites.

In the continuum limit ($a_0 \to 0$) the Brillouin zone extends to $[-\infty, \infty]$ and the annihilation and creation operators are mapped to analogous fermionic fields. For instance, the field operator of the corresponding annihilation operator $c_{k,\sigma}$ and its inverse transformation are given by

$$\psi_\sigma(x) = \frac{1}{\sqrt{L}} \sum_{k=-\infty}^{+\infty} e^{ikx} c_{k,\sigma} \quad \text{and} \quad c_{k,\sigma} = \frac{1}{\sqrt{L}} \int_{-L/2}^{+L/2} dx\, e^{-ikx} \psi_\sigma(x)\,, \tag{1.7}$$

where the momentum $k = 2\pi/L \times n$ is not bounded, i.e. $n = 0, \pm 1, \pm 2 \ldots$. The continuous variable x is related to the discrete lattice site n through $x \to na_0$.

In the weak-coupling approach one assumes that the low energy physics is only relevant near the two Fermi points $\pm k_F$. Therefore, it is possible to linearize the energy spectrum $\varepsilon(k) = v_F(k - k_F)$ for right movers and $\varepsilon(k) = -v_F(k + k_F)$ for left movers with

$$v_F = \left.\frac{\partial \varepsilon(k)}{\partial k}\right|_{k=k_F} \propto \left.\frac{\partial \cos(k)}{\partial k}\right|_{k=k_F}\,, \tag{1.8}$$

which expresses the relation between the linearized spectrum and the lattice one. Moreover, one decomposes the sum in expression (1.7) into two parts, corresponding to $k > 0$ and $k < 0$, and then shifts each sum by $\pm k_F$ so that $k = 0$

corresponds to the Fermi points:

$$
\begin{aligned}
\psi_\sigma(x) &= \frac{1}{\sqrt{L}} \sum_{k>0} e^{ikx} c_{k,\sigma} + \frac{1}{\sqrt{L}} \sum_{k<0} e^{ikx} c_{k,\sigma} \\
&= \frac{1}{\sqrt{L}} \sum_{k=-k_F}^{+\infty} e^{i(k+k_F)x} c_{k+k_F,\sigma} + \frac{1}{\sqrt{L}} \sum_{k=-\infty}^{+k_F} e^{i(k-k_F)x} c_{k-k_F,\sigma} \\
&\equiv e^{ik_F x} \psi_{R,\sigma}(x) + e^{-ik_F x} \psi_{L,\sigma}(x)
\end{aligned}
\tag{1.9}
$$

The smooth field operators ψ_R and ψ_L describe right- and left-movers with mean momenta centered around $\pm k_F$. By using formula (1.9) the real space counterpart of the free fermion Hamiltonian (1.6) then reads

$$
\mathcal{H}_0 = -i v_F \int_{-L/2}^{+L/2} dx \sum_\sigma \left(\psi_{R,\sigma}^\dagger(x) \partial_x \psi_{R,\sigma}(x) - \psi_{L,\sigma}^\dagger(x) \partial_x \psi_{L,\sigma}(x) \right) .
\tag{1.10}
$$

For the derivation one must note the following: the cross terms between left and right components will make no contribution because the smooth left and right fields have no overlap if the fluctuations around $\pm k_F$ are assumed to be small. Finally, a first order Taylor expansion has been applied

$$
\psi_{\eta,\sigma}(x + a_0) \approx \psi_{\eta,\sigma}(x) + a_0 \partial_x \psi_{\eta,\sigma}(x)
\tag{1.11}
$$

for each branch $\eta \in \{R, L\}$ of the dispersion curve. Sometimes we will use the notation $\eta \in \{+1, -1\}$ instead of R and L and furthermore $\sigma \in \{+1, -1\}$ instead of $\uparrow$ and $\downarrow$.

1.2.2. Scattering processes

Due to the special topology of the one-dimensional Fermi surface, the space for *collisions* between particles is strongly limited compared to higher dimensional systems. By energy and momentum conservation alone, the corresponding low-energy scattering processes, restricted to the two Fermi points $\pm k_F$, can be classified into four different types. These four species of collisions are illustrated in Fig. 1.2. Next, the coupling constants for electrons with parallel spins will be denoted by the subscript '$\parallel$' and those with anti-parallel spins by '$\perp$'. Following [9], the scattering process with coupling g_4 describes *forward* scattering, where all four participating electrons belong to a single branch. Using the smooth field operators ψ_R and ψ_L the Hamiltonian reads

$$
\mathcal{H}_{\text{int}}^{g_4} \propto \sum_{\sigma,\sigma'} \frac{1}{2} \left(g_{4\parallel} \, \delta_{\sigma,\sigma'} + g_{4\perp} \, \delta_{\sigma,-\sigma'} \right) \sum_\eta \psi_{\eta,\sigma}^\dagger \psi_{\eta,\sigma'}^\dagger \psi_{\eta,\sigma'} \psi_{\eta,\sigma} .
\tag{1.12}
$$

The *dispersion*, characterized by g_2, corresponds to similar events but involves electrons on both branches. The interacting Hamiltonian has the form

$$
\mathcal{H}_{\text{int}}^{g_2} \propto \sum_{\sigma,\sigma'} \left(g_{2\parallel} \, \delta_{\sigma,\sigma'} + g_{2\perp} \, \delta_{\sigma,-\sigma'} \right) \psi_{R,\sigma}^\dagger \psi_{L,\sigma'}^\dagger \psi_{L,\sigma'} \psi_{R,\sigma} .
\tag{1.13}
$$

Figure 1.2.: The four scattering processes in the so-called *g-ology* nomenclature for right-moving (solid lines) and left-moving (dashed lines) electrons in one dimension. In all these processes the spin dependence is suppressed.
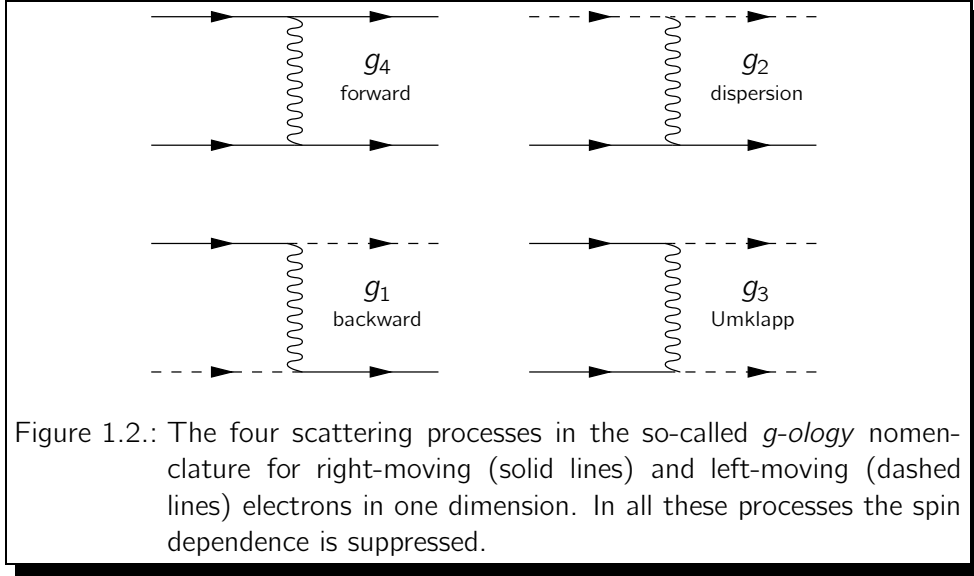
Note that in both processes the associated momentum transfer is small. The g_1 event describes *backward* scattering, where each electron changes branch but keeps its spin. This contribution is given by

$$\mathcal{H}_{\text{int}}^{g_1} \propto \sum_{\sigma,\sigma'} \left(g_{1\parallel}\, \delta_{\sigma,\sigma'} + g_{1\perp}\, \delta_{\sigma,-\sigma'} \right) \psi_{R,\sigma}^\dagger \psi_{L,\sigma'}^\dagger \psi_{R,\sigma'} \psi_{L,\sigma} . \qquad (1.14)$$

The momentum transfer is of order $2k_F$. Finally, the *Umklapp* process (two left electrons become right electrons or vice-versa) is denoted by g_3 and is important only if the band is half-filled, i.e. only if $4k_F$ is equal to a reciprocal lattice vector. The process is expressed by the term

$$\mathcal{H}_{\text{int}}^{g_3} \propto \sum_{\sigma,\sigma'} \frac{1}{2} \left(g_{3\parallel}\, \delta_{\sigma,\sigma'} + g_{3\perp}\, \delta_{\sigma,-\sigma'} \right) \sum_{\eta} \psi_{\eta,\sigma}^\dagger \psi_{\eta,\sigma'}^\dagger \psi_{-\eta,\sigma'} \psi_{-\eta,\sigma} . \qquad (1.15)$$

Since the effect of $g_{1\parallel}$ is indistinguishable from that of $g_{2\parallel}$, one may set $g_{1\parallel} = 0$ without loss of generality. A spin-rotationally invariant model further reduces the number of independent couplings. Note that scattering processes of type g_2 and g_4 do not break symmetries. In contrast, the Umklapp process g_3 breaks the conservation of individual charge currents and a charge gap opens if the interactions are attractive ($g_3 < 0$). Similarly, the attractive backscattering process $g_1 < 0$ breaks the conservation of individual spin currents and a gap in the spin excitation spectrum opens.

A detailed renormalization group analysis of this *interacting gas model* is given by Sólyom [9]. For particular combinations of these coupling constants exact solutions are known. On the one hand there is the gapless Tomonaga-Luttinger (TL) model and on the other hand there is the Luther-Emery (LE) model having a gap in the spin excitation spectrum. Both models can be solved exactly by expressing the fermionic field operators in terms of boson operators [7, 8].

1.2.3. Bosonic representation of the TL model

The TL model is a particular model of the interacting Fermi gas, Eqs. (1.12)-(1.15) and Eq. (1.10), in which the bosonization technique yields an exact solution. The Hamiltonian of the TL model for spin-1/2 particles reads

$$\mathcal{H}_{TL} = \mathcal{H}_0 + \mathcal{H}_{int}^{g_2} + \mathcal{H}_{int}^{g_4} \tag{1.16}$$

$$= -iv_F \int dx \sum_{\sigma,\eta} \eta \, \psi_{\eta,\sigma}^\dagger(x) \partial_x \psi_{\eta,\sigma}(x)$$

$$+ \int dx \sum_{\sigma,\sigma'} \left(g_{2\parallel} \delta_{\sigma,\sigma'} + g_{2\perp} \delta_{\sigma,-\sigma'} \right) \psi_{R,\sigma}^\dagger(x) \psi_{L,\sigma'}^\dagger(x) \psi_{L,\sigma'}(x) \psi_{R,\sigma}(x)$$

$$+ \int \frac{dx}{2} \sum_{\sigma,\sigma',\eta} \left(g_{4\parallel} \delta_{\sigma,\sigma'} + g_{4\perp} \delta_{\sigma,-\sigma'} \right) \psi_{\eta,\sigma}^\dagger(x) \psi_{\eta,\sigma'}^\dagger(x) \psi_{\eta,\sigma'}(x) \psi_{\eta,\sigma}(x) \, .$$

A bosonic formulation of (1.16) is described by two independent bosonic fields, one representing the charge and the other the spin degrees of freedom. The fermionic field operators $\psi_{\eta,\sigma}$ are represented by bosonic operators $\Phi_{\eta,\sigma}$ via the identity [10]

$$\psi_{\eta,\sigma}(x) = \frac{1}{\sqrt{2\pi\alpha}} F_{\eta,\sigma} \exp\left[i\Phi_{\eta,\sigma}(x)\right] , \tag{1.17}$$

where α is a short distance cut-off that is taken to zero at the end of the calculation and the so-called *Klein factors* $F_{\eta,\sigma}$ are responsible for reproducing the correct anticommutation relations between different fermionic species. The bosonic fields $\Phi_{\eta,\sigma}$, which obey

$$\left[\Phi_{\eta,\sigma}(x), \Phi_{\eta',\sigma'}^\dagger(x')\right] = -i\pi \, \delta_{\eta,\eta'} \, \delta_{\sigma,\sigma'} \, \text{sign}(x - x') \, , \tag{1.18}$$

in turn are combinations of bosonic fields ϕ_μ and their conjugate momenta $\partial_x\theta_\mu$, where the subscript denotes charge ($\mu = c$) or spin ($\mu = s$) degrees of freedom. The relation is given by

$$\Phi_{\eta,\sigma} = \sqrt{\frac{\pi}{2}} \left[(\theta_c - \eta\phi_c) + \sigma(\theta_s - \eta\phi_s) \right] , \tag{1.19}$$

where ϕ_μ and θ_μ satisfy the following commutation relation

$$\left[\phi_\mu(x), \theta_{\mu'}(x')\right] = \frac{i}{2}\delta_{\mu,\mu'} \, \text{sign}(x - x') \, . \tag{1.20}$$

From a physical point of view, ϕ_c and ϕ_s are the phases of the charge density wave (CDW) and spin density wave (SDW) fluctuations, i.e.

$$\rho(x) \approx \sqrt{\frac{2}{\pi}}\partial_x\phi_c(x) \quad \text{and} \quad S^z(x) \approx \sqrt{\frac{1}{2\pi}}\partial_x\phi_s(x) \, , \tag{1.21}$$

whereas θ_c describes the superconducting phase (see chapter 4 for details). The Hamiltonian can now be expressed as a sum of two decoupled pieces of bosonic oscillators involving either charge or spin density wave eigenmodes

$$\mathcal{H}_{TL}^B = \int dx \sum_{\mu=c,s} \left(\frac{v_\mu K_\mu}{2}[\partial_x\theta_\mu(x)]^2 + \frac{v_\mu}{2K_\mu}[\partial_x\phi_\mu(x)]^2 \right) . \tag{1.22}$$

In terms of the parameters $g_{ic} \equiv g_{i\parallel} + g_{i\perp}$ and $g_{is} \equiv g_{i\parallel} - g_{i\perp}$ ($i = 2, 4$) the charge and spin velocities are

$$v_\mu = v_F \sqrt{\left(1 + \frac{g_{4\mu}}{2\pi v_F}\right)^2 - \left(\frac{g_{2\mu}}{2\pi v_F}\right)^2} \, . \qquad (1.23)$$

One spectacular consequence is the so-called *spin-charge separation* (cf. with Eq. (1.22)) which is completely absent in higher dimensions. In this description this is due to the fact that spin and charge density modes propagate with different velocities ($v_s \neq v_c$) and therefore will separate with time. The parameters K_μ, which determine the decay behaviour of the correlation functions, are

$$K_\mu = \sqrt{\frac{2\pi v_F + g_{4\mu} - g_{2\mu}}{2\pi v_F + g_{4\mu} + g_{2\mu}}} \, . \qquad (1.24)$$

Note that the properties of the TL model are completely described by the set of parameters $\{v_\mu, K_\mu\}$.

1.2.4. Single- and two-particle correlation functions

In this section we give a summary of the correlation functions from which the physical properties of the TL model may be obtained. Here we will restrict ourselves to the $SU(2)$ spin-invariant model with $K_s = 1$.

From our previous discussion of spin-charge separation it is already obvious that the TL system is *not* a Fermi liquid. This can be made more precise. After applying the Fourier transformation on the single-particle Green's function $G_\sigma(x, t)$ the corresponding momentum distribution function in the vicinity of the Fermi surface reads

$$n_\sigma(k) \approx n_\sigma(k_F) - \text{const.} \times \text{sign}(k - k_F)|k - k_F|^\gamma \, , \qquad (1.25)$$

where the exponent γ has the explicit form

$$\gamma = \frac{1}{4}\left(K_c + K_c^{-1} - 2\right) \geq 0 \, . \qquad (1.26)$$

Note that for any nonvanishing interaction ($K_c \neq 1$) the discontinuity at k_F is absent, i.e. $n_\sigma(k)$ is continuous (cf. with section 1.1).

The coefficient K_c also determines the long-distance decay behaviour of all other correlation functions $\langle \mathcal{O}^\dagger(x)\mathcal{O}(x') \rangle$ in which the order parameter $\mathcal{O}$ describes an instability of the systems. The relevant operators which can take on non-zero expectation values are the $2k_F$ CDW and SDW instabilities and the singlet (SS) and triplet (TS) superconducting operators. An explicit fermionic and bosonic expression will be discussed in chapter 4.

The asymptotic shape of the correspondig correlation functions can be calculated exactly (see [11] and references therein). In detail, one obtains

  1. for the density-density correlation (similar to CDW)

$$\langle \rho(0)\rho(r) \rangle \sim \frac{A_0}{r^2} + \frac{A_1 \cos(2k_F r)}{r^{1+K_c}} + \frac{A_2 \cos(4k_F r)}{r^{4K_c}} + \dots \, , \qquad (1.27)$$

2. for the spin-spin correlation (similar to SDW)

$$\langle S^z(0)S^z(r)\rangle \sim \frac{B_0}{r^2} + \frac{B_1\cos(2k_F r)}{r^{1+K_c}} + \dots, \tag{1.28}$$

3. for the singlet-pair correlation

$$\langle \mathcal{O}_{SS}^\dagger(0)\mathcal{O}_{SS}(r)\rangle \sim \frac{C_0}{r^{1+K_c^{-1}}} + \frac{C_1\cos(2k_F r)}{r^{K_c+K_c^{-1}}} + \dots \tag{1.29}$$

4. and for the triplet-pair correlation

$$\langle \mathcal{O}_{TS}^\dagger(0)\mathcal{O}_{TS}(r)\rangle \sim \frac{D_0}{r^{1+K_c^{-1}}} + \frac{D_1\cos(2k_F r)}{r^{K_c+K_c^{-1}+2}} + \dots. \tag{1.30}$$

The constant coefficients A_i, B_i, C_i and D_i are model dependent. The *algebraic* decay of each correlation function is characterized by the exponent K_c only. For $K_c < 1$ spin or charge density fluctuations will be enhanced, while for $K_c > 1$ pairing fluctuations will dominate.
Note that logarithmic corrections, sometimes included in the above formulae [12], have not been taken into account because they are not important as long as one is only interested in the asymptotics $r \gg 1$ of the correlations.
In general, 1D quantum-systems with short-range interaction and gapless excitations are critical at zero temperature. In such a case, various correlation functions show *power-law* decay. Otherwise, i.e. in the presence of a gap (cf. with Sec. 1.3), they may decay *exponentially* and the corresponding *correlation length* ξ is determined by the gap. Closing of a gap indicates a divergent correlation length. In the limit $\xi \to \infty$ the corresponding correlations show *power-law* decay. Note that long-range order (LRO) in 1D quantum-systems at finite temperature $T > 0$ is forbidden by the Mermin-Wagner theorem [13]. This statement is also valid for $T = 0$ [14] as long as the models are described by continuous symmetries. However, models with a discrete symmetry (cf. with chapter 4) admit LRO even in 1D. Therefore, 1D phases are best characterized by the asymptotic behaviour of the correlation functions.

1.3. The Luther-Emery phase

The TL model is very restrictive since the interaction parameters g_2 and g_4 are associated with a small momentum transfer whereas any realistic model with interaction of type

$$\mathcal{H}_{int} = \frac{1}{L} \sum_{k,k',q,\sigma,\sigma'} V(q)c_{k+q,\sigma}^\dagger c_{k'-q,\sigma'}^\dagger c_{k',\sigma'} c_{k,\sigma} \tag{1.31}$$

also contains contributions with $q \geq 2k_F$. Note that the choice of parameters under which the numbers of right and left movers are conserved is essential in guaranteeing the exact solvability of this model.

Additional terms like g_1 or g_3 destroy the symmetry because they change the individual particle numbers. The Hamiltonian of the TL model (1.22) in which processes like

$$\mathcal{H}^{\text{B}}_{g_{1\perp}} = \frac{g_{1\perp}}{2(\pi\alpha)^2} \int dx \cos(\sqrt{8\pi}\phi_s) \quad \text{or} \tag{1.32}$$

$$\mathcal{H}^{\text{B}}_{g_{3\perp}} = \frac{g_{3\perp}}{2(\pi\alpha)^2} \int dx \cos(\sqrt{8\pi}\phi_c) \tag{1.33}$$

are included is, in general, no longer exactly solvable but a renormalization group (RG) analysis permits important insights about the influence of such terms.
For simplicity, let us focus on a spin-independent Hamiltonian (1.12)–(1.14) with $g_{i\parallel} = g_{i\perp} = g_i$ ($i = 1, 2, 4$) which can be realized in a $SU(2)$ symmetric model. The RG flow equations for cut-off dependent interactions $g_i(\ell)$ are quite simple [9] and translate into

$$\frac{d}{d\ell} g_1(\ell) = -\frac{1}{\pi v_F} g_1^2(\ell) \quad \text{and} \tag{1.34}$$

$$\frac{d}{d\ell} g_2(\ell) = -\frac{1}{2\pi v_F} g_1^2(\ell) . \tag{1.35}$$

after short-distance degrees of freedom have been integrated out. Note that g_4 is not renormalized and that $g_1(\ell)$ can be determined from the first equation only

$$g_1(\ell) = \frac{g_1}{1 + \ell \frac{g_1}{\pi v_F}} \tag{1.36}$$

where g_1 is the starting value. Furthermore, it is easy to see that

$$g_1(\ell) - 2g_2(\ell) = g_1 - 2g_2 \tag{1.37}$$

holds by subtracting twice the second equation from the first in Eq. (1.34). There are two different types of flow:

❶ For $g_1 \geq 0$ one renormalizes to the fixed line $g_1^* = 0$ and $g_2^* = g_2 - g_1/2$, where the notation $g_i^* \equiv g_i(\ell \to \infty)$ was used. The *fixed point* Hamiltonian is a TL model with repulsive interactions in which the g_1-interaction is irrelevant.

❷ For $g_1 < 0$ the solution (1.36) shows that $g_1(\ell)$ *diverges* at a finite value of ℓ, i.e. long before reaching this point the perturbational analysis breaks down. However, one should notice that, well before the divergence, one has left the weak-coupling regime where Eq. (1.34) and (1.35) are valid. Therefore, one should not overinterpret the divergence and just remember that the RG scales to strong coupling.

When $g_{1\parallel} = g_{1\perp} < 0$, the system is described by the presence of a finite spin gap Δ_s. Further RG investigations show that the gap remains for all $g_{1\perp} < 0$ and $|g_{1\perp}| > g_{1\parallel}$. For the anisotropic case, Luther and Emery have shown that for the

particular point $K_s = 1/2$ the model is exactly solvable. At this point a new set of spinless fermions can be defined

$$\Psi_\eta \equiv \frac{1}{\sqrt{2\pi\alpha}} F_\eta \exp[i\sqrt{\pi/2}(\theta_s - 2\eta\phi_s)] \tag{1.38}$$

and the spin part of the corresponding *refermionized* Hamiltonian then reads

$$\mathcal{H}_s = -iv_s \sum_\eta \eta \Psi_\eta^\dagger \partial_x \Psi_\eta + \Delta_s(\Psi_R^\dagger \Psi_L + \text{h.c.}) . \tag{1.39}$$

This Hamiltonian is easy to diagonalize and the exact result indicates an energy spectrum

$$E_s = \sqrt{v_s^2 k^2 + \Delta_s^2} \quad \text{with a finite gap} \quad \Delta_s \sim \frac{|g_{1\perp}|}{2\pi\alpha} . \tag{1.40}$$

This gap has drastic consequences for the physical properties, i.e. correlations such as SDW and triplet pairing are *not* critical and decay exponentially with correlation length $\xi_s = v_s/\Delta_s$, whereas CDW and SS correlators are enhanced compared to the case with no spin gap.

Figure 1.3.: Phase diagram in the $g_{1\perp}$-K_c plane for a 1D interacting gas model in the absence of Umklapp scattering (from [15]). Correlations indicated in parentheses have the same exponents as the dominant ones but are logarithmically weaker. At $g_{1\perp} \geq 0$ the system belongs to the TL liquid with gapless excitations, whereas the shaded region ($g_{1\perp} < 0$) contains the spin gapped phases. Here, fluctuations appearing in parentheses diverge with a smaller power-law exponent than the dominant ones.

Without logarithmic corrections their asymptotic form explicitly reads [8]

1. for the density-density correlation

$$\langle \rho(0)\rho(r) \rangle \sim \frac{A_0}{r^2} + \frac{A_1 \cos(2k_F r)}{r^{K_c}} + \frac{A_2 \cos(4k_F r)}{r^{4K_c}} + \dots \tag{1.41}$$

2. and for the singlet pairing correlation

$$\langle \mathcal{O}_{SS}^{\dagger}(0)\mathcal{O}_{SS}(r)\rangle \sim \frac{C_0}{r^{K_c^{-1}}} + \frac{C_1}{r^{K_c + K_c^{-1}}} + \dots . \tag{1.42}$$

Note that these properties are not restricted to the solvable parameter values only. Figure 1.3 shows the phase diagram in parameter space characterized by dominating correlation functions. From that figure one can conclude that a TL liquid as well as the *Luther-Emery* (LE) phase become superconducting for $K_c > 1$. Otherwise the CDW or the SDW correlations dominate.

1.4. Determination of K_μ and v_μ

In the previous sections we have seen that the complete low energy physics of a weakly-interacting electron model is determined by the parameters K_μ and v_μ only. Various *lattice* models like the (attractive or non half-filled) Hubbard model or the $t - J$ model belong to the universality class of either a TL liquid or the spin gapped LE phase. Thus all these coefficients may be useful for strongly correlated models too.

One possibility to compute K_μ and v_μ is to use their relations to spin and charge compressibilities. More precisely, for the charge degree of freedom the ratio v_c/K_c can be calculated by the variation of ground state energy [12]

$$\frac{1}{L}\frac{\partial^2 E_0(n)}{\partial n^2} = \frac{\pi}{2}\frac{v_c}{K_c}, \tag{1.43}$$

where $n = N/L$ is the band filling depending on the number of electrons N and the lattice size L. Note that the quantity is the inverse of the compressibility κ. The finite-size approximation of it, useful for numerical computation, is given by

$$\kappa = \frac{L}{N^2}\left(\frac{E_0(L, N+2) + E_0(L, N-2) - 2E_0(L, N)}{4}\right)^{-1}. \tag{1.44}$$

The charge velocity v_c can be obtained from the low-energy spectrum $E(k)$ in the following way

$$v_c = \frac{\partial E(k)}{\partial k}\bigg|_{k=0}. \tag{1.45}$$

The discretized pendant of this derivation, necessary for finite systems, reads

$$v_c = \frac{E_0(L, N, S^z = 0, k = 2\pi/L) - E_0(L, N, S^z = 0, k = 0)}{2\pi/L}, \tag{1.46}$$

where $E_0(L, N, S^z = 0, k = 2\pi/L)$ denotes the first excited state in the sector $S^z = 0$. However, if quantum chains with open boundary conditions are considered, one has to put $k = \pi/L$ instead of $k = 2\pi/L$.

If the model is exactly solvable, like the 1D Hubbard model, then the ground state energy E_0 and the charge velocity v_c can be obtained by solving the Lieb-Wu equations (see Sec. 2.3.2 for details) in the thermodynamic limit [12]. The

Figure 1.4.: The critical exponent K_c (here denoted by K_ρ) for the repulsive Hubbard model as a function of the band filling $n = N/L$ with $U/t = 1$ for the top curve and with $U/t = 2, 4, 8, 16$ for the bottom curves (from [12]).
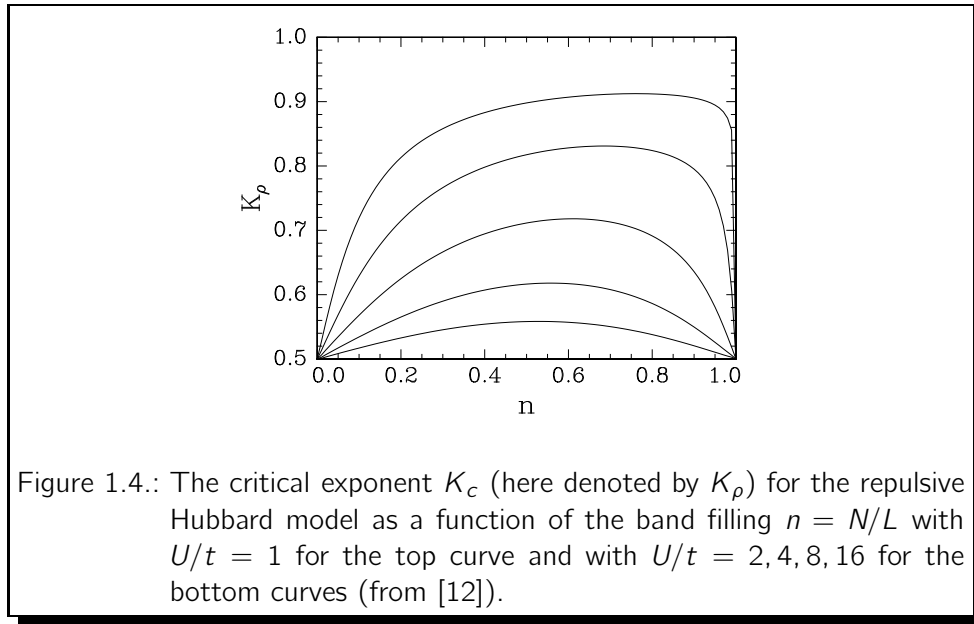
results for K_c as a function of n are shown in Fig. 1.4 for different values of $U/t > 0$. In the whole parameter region one always has $K_c < 1$, which means that magnetic fluctuations are dominant and on the other hand superconducting pairing is suppressed. Note that the situation changes for the attractive U [16].

Frahm and Korepin applied the conformal field theory in order to deduce the asymptotics of correlation functions for the 1D Hubbard model in the repulsive regime [17]. Within this theory, the role of the critical exponents is replaced by the so-called *scaling dimensions*. Additionally, they have shown that the elements of the so-called *dressed charge matrix* are related to the thermodynamic quantities of the model, especially to the compressibility and therefore to K_c. The entries obey integral equations derived from and similar to the Lieb-Wu equations in the thermodynamic limit.

Another approach how to compute K_μ numerically will be discussed in chapter 4. The basic idea is to determine the asymptotics of a suitable correlation function. However, in order to get qualitatively good results some technical effort is necessary.

1.5. Quasi-1D organic (super-) conductors

Organic conductors (see also the pioneer works [18, 19, 20]), like *Bechgaard* or *Fabre* salts are built up from large planar molecules stacked along one direction. The structure within the salts is characterized by several of such molecular chains lying next to each other. The motion of electrons is different in each direction and most significant along the chains of molecules in which the orbital overlap is strongest. Because of these differences in conductivity, these organic compounds show a *quasi one-dimensional* behaviour. Compared to the Bechgaard compounds $(TMTSF)_2X$ (X is a monovalent anion), the Fabre salts $(TMTTF)_2X$ exhibit

a more one-dimensional structure, since the interaction between neighbouring molecular chains is weaker. The properties of each compound become similar, if external pressure is applied, associating with a decrease of the distance between the chains, which leads to a *dimensional crossover* to higher dimensions.
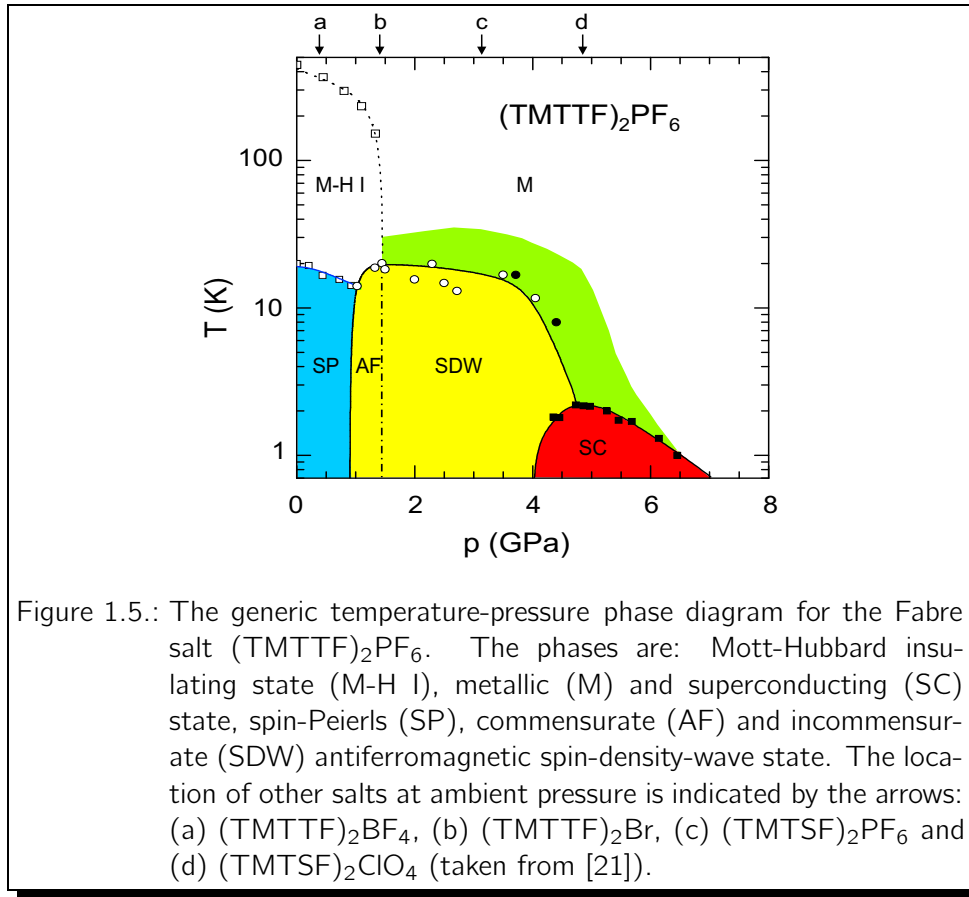

Figure 1.5.: The generic temperature-pressure phase diagram for the Fabre salt $(TMTTF)_2PF_6$. The phases are: Mott-Hubbard insulating state (M-H I), metallic (M) and superconducting (SC) state, spin-Peierls (SP), commensurate (AF) and incommensurate (SDW) antiferromagnetic spin-density-wave state. The location of other salts at ambient pressure is indicated by the arrows: (a) $(TMTTF)_2BF_4$, (b) $(TMTTF)_2Br$, (c) $(TMTSF)_2PF_6$ and (d) $(TMTSF)_2ClO_4$ (taken from [21]).

The phase diagram of these organic compounds is extraordinarily rich with almost all known electronic states of matter (see Fig. 1.5). At low pressure the $(TMTTF)_2PF_6$ compound behaves very much like a TLL conductor where spin and charge degrees of freedom are decoupled. The phase below $T_\rho = 250$ K is decribed by the presence of a charge gap and it has been interpreted as a Mott insulating state. At T_{SP} further transition takes place which is characterized by the opening of a spin gap. This transition can be considered as a spin-Peierls transition, involving formation of a density wave. By the application of external pressure or by the substitution of the anion X by atoms of different size, i. e. by chemical pressure, inter-chain interactions become more important and a crossover from a quasi 1D system to a Fermi liquid takes place. In this region dominant electron-electron interactions lead to a spin-density-wave ground state as observed in the Bechgaard salt $TMTSF_2PF_6$. With increasing pressure the system remains metallic and superconductivity replaces the SDW ground state. The range of strong SDW correlations for $TMTSF_2PF_6$ is possibly larger, as indicated in Fig. 1.5 by the shaded region above the SDW and SC phase boundaries.

From a theoretical point of view, organic conductors like Bechgaard or Fabre salts are very interesting compounds. Due to the simple topological structure it is possible to apply various well elaborated 1D tools and compare/varify the results with experimental predictions. For instance, the dimensional crossover can be studied by applying TLL tools on coupled chain-models, starting from a single chain. Another interesting point is to find a microscopic description for the mechanism which leads to superconductivity.

2. The generalized Hubbard model

In the previous sections the interacting electron gas, which is characterized by weak interactions, was the subject of interest. Here we will focus on strongly correlated lattice systems. One of the most prominent models is the so-called *Hubbard model*. It appeared in the literature for the first time in 1963, independently proposed by Hubbard [22], Gutzwiller [23] and Kanamori [24], as an attempt to describe in a simplified way the effect of electron correlations in narrow energy bands, in particular in d-bands of transition metals. The microscopic model consists of two parts: a kinetic term describing the motion of electrons and a second term, which approximates the Coulomb interaction among them. Because of the mechanism, the Hamiltonian is expected to be suitable for describing the main collective features such as itinerant magnetism or metal-insulator transition. Moreover, since the discovery of high temperature superconductors in 1986 [25], where strong electron correlations are believed to be important [26, 27], makes the two dimensional Hubbard model relevant for such materials.

In the following section we give a step-by-step derivation of the generalized Hubbard model starting from a general solid state Hamiltonian describing the interactions between electrons in the potential $U_{\text{ion}}(\mathbf{r})$ created by a lattice of ions. Afterwards, we provide an overview about some rigorous results and exact solutions for the one–dimensional Hubbard model.

2.1. Derivation of the generalized Hubbard model

After neglecting some irrelevant parts, such as the spin-orbit interaction and relativistic corrections, and the use of the so-called *adiabatic approximation*[1] the general Hamiltonian $\mathcal{H}$ in solid state physics (expressed in the language of second quantization) reads

$$
\begin{aligned}
\mathcal{H} &= \sum_{\sigma} \int d\mathbf{r}\, \psi_{\sigma}^{\dagger}(\mathbf{r}) \left(-\frac{\hbar^2}{2m}\nabla^2 + U_{\text{ion}}(\mathbf{r}) \right) \psi_{\sigma}(\mathbf{r}) \\
&+ \sum_{\sigma,\sigma'} \int d\mathbf{r} \int d\mathbf{r}'\, \psi_{\sigma}^{\dagger}(\mathbf{r})\psi_{\sigma'}^{\dagger}(\mathbf{r}')V_{ee}(\mathbf{r}-\mathbf{r}')\psi_{\sigma'}(\mathbf{r}')\psi_{\sigma}(\mathbf{r})\,, \quad (2.1)
\end{aligned}
$$

where $U_{\text{ion}}(\mathbf{r})$ labels the potential of the atom ions, $V_{ee}(\mathbf{r}-\mathbf{r}') \propto 1/|\mathbf{r}-\mathbf{r}'|$ the repulsive Coulomb potential and $\psi_{\sigma}^{\dagger}(\mathbf{r})$ a field operator. In a perfect crystal the

---

[1]or the Born-Oppenheimer approximation, based on the fact that typical electronic velocities are much greater than typical ionic velocities, leads to a Hamiltonian which describes electrons moving in a static lattice of ions.

ions are arranged in a regular periodic array. Thus we consider a periodic potential $U_{\text{ion}}(\mathbf{r} + \mathbf{R}) = U_{\text{ion}}(\mathbf{r})$, where $\mathbf{R}$ denotes a Bravais lattice vector. According to Bloch's theorem, the free electronic band splits under the influence of $U_{\text{ion}}(\mathbf{r})$ into infinitely many energy bands α with Bloch functions $u_{k\alpha}$. However, electrons in narrow energy bands, such as d-bands in transition metals, exhibit a 'poor' dynamics and are mostly localized around the atomic sites. Consequently the Bloch functions are unusable for such bands. A substantially better starting point is achieved with the so-called *tight-binding-approximation*, illustrated in Fig. 2.1. Functions with such a local behaviour are called Wannier functions. They are

Figure 2.1.: A schematic illustration of the the tight-binding approximation (taken from [28]). a) An isolated atom with three orbitals. b) The overlap of four identical atoms building a solid with electron bands. Electrons in black orbitals become itinerant (conduction band), while those in the light gray orbitals are still localized at the original atomic sites. Electrons in the gray orbitals are mostly localized around the atomic sites, but tunnel to nearby gray orbitals with a non-negligible probability (valence band). c) An approximation to valence electrons, which are expected to play essential roles in determining various low energy physics of the system. d) A reduction to a lattice model in which electrons live on lattice sites and move from one site to another.

related to the Bloch functions by an unitary transformation

$$\phi_{i,\alpha}(\mathbf{r}) = \frac{1}{\sqrt{L}} \sum_{k} e^{-ikR_i} u_{k,\alpha}(\mathbf{r}) \, , \tag{2.2}$$

where $\mathbf{R}_i$ labels the sites of the lattice center and L is the total number of lattice sites. The Hamiltonian (2.1) then transforms to

$$\mathcal{H} = \sum_{i,j,\alpha,\sigma} t_{ij}^{\alpha} c_{i,\alpha,\sigma}^{\dagger} c_{j,\alpha,\sigma} + \sum_{ijmn} \sum_{\alpha\beta\mu\nu} \sum_{\sigma\sigma'} v_{ijmn}^{\alpha\beta\mu\nu} c_{i,\alpha,\sigma}^{\dagger} c_{j,\beta,\sigma'}^{\dagger} c_{n,\nu,\sigma'} c_{m,\mu,\sigma} \, , \tag{2.3}$$

where $c_{i\alpha\sigma}^\dagger$ is a fermionic operator creating an electron with spin σ in a Wannier orbital α localized at site i. The coefficients are given by the matrix elements

$$
\begin{aligned}
t_{ij}^\alpha &= \langle i\alpha | \frac{-\hbar^2}{2m}\nabla^2 + U_{\text{ion}}(\mathbf{r}) | j\alpha \rangle \\
&= \int d\mathbf{r}\, \phi_{i,\alpha}^*(\mathbf{r}) \left[\frac{-\hbar^2}{2m}\nabla^2 + U_{\text{ion}}(\mathbf{r}) \right] \phi_{j,\alpha}(\mathbf{r})
\end{aligned}
\tag{2.4}
$$

and

$$
\begin{aligned}
v_{ijmn}^{\alpha\beta\mu\nu} &= \langle i\alpha, j\beta | V_{ee}(\mathbf{r}-\mathbf{r}') | m\mu, n\nu \rangle \\
&= \int d\mathbf{r} \int d\mathbf{r}'\, \phi_{i,\alpha}^*(\mathbf{r})\phi_{j,\beta}^*(\mathbf{r}') V_{ee}(\mathbf{r}-\mathbf{r}') \phi_{m,\mu}(\mathbf{r})\phi_{n,\nu}(\mathbf{r}') .
\end{aligned}
\tag{2.5}
$$

The electronic Hamiltonian (2.3) contains infinitely many parameters. For simplicity it is therefore often assumed that the essential physics of the problem is captured by a single s-band, thus all orbital indices α, β etc. can be omitted. Since the matrix elements are expected to decrease strongly with increasing distance, one usually takes only next-neighbor interactions $\langle ij \rangle$ into account. Furthermore, the matrix element t_{ij} depends only on the separation of unit cells and not on direction, hence $t_{ij} = t(\mathbf{R}_i - \mathbf{R}_j)$. Using all these simplifications the Hamiltonian reads

$$
\begin{aligned}
\mathcal{H} =\ & -t \sum_{\langle ij \rangle} \sum_{\sigma} \left(c_{i,\sigma}^\dagger c_{j,\sigma} + c_{j,\sigma}^\dagger c_{i,\sigma} \right) + U \sum_i n_{i,\uparrow} n_{i,\downarrow} + V \sum_{\langle ij \rangle} n_i n_j \\
& + J \sum_{\langle ij \rangle} \mathbf{S}_i \cdot \mathbf{S}_j + X \sum_{\langle ij \rangle} \sum_{\sigma} \left(c_{i,\sigma}^\dagger c_{j,\sigma} + c_{j,\sigma}^\dagger c_{i,\sigma} \right) \left(n_{i,-\sigma} + n_{j,-\sigma} \right) \\
& + Y \sum_{\langle ij \rangle} c_{i,\uparrow}^\dagger c_{i,\downarrow}^\dagger c_{j,\downarrow} c_{j,\uparrow}
\end{aligned}
\tag{2.6}
$$

which is known as the *generalized Hubbard model*. We used the following short-hand notation

$$
\begin{aligned}
t &\equiv -t_{ij}, & U &\equiv v_{iiii}, & X &\equiv v_{iiij} \\
V &\equiv v_{ijij}, & J &\equiv -2v_{ijji}, & Y &\equiv v_{iijj} .
\end{aligned}
\tag{2.7}
$$

The particle number operators $n_{j,\sigma}$, n_j and the spin operators $\mathbf{S}_j$ are defined as

$$
n_{j,\sigma} = c_{j,\sigma}^\dagger c_{j,\sigma}, \quad n_j = n_{j,\uparrow} + n_{j,\downarrow}, \quad \mathbf{S}_j = \frac{1}{2} \sum_{\alpha,\beta} c_{j,\alpha}^\dagger \vec{\tau}_{\alpha\beta} c_{j,\beta} ,
\tag{2.8}
$$

where $\vec{\tau}_{\alpha\beta} = ((\tau^x)_{\alpha\beta}, (\tau^y)_{\alpha\beta}, (\tau^z)_{\alpha\beta})$ is a vector which consists of the usual Pauli matrices. Apart from the *single-particle hopping* term t, which describes the motion of electrons to neighbouring lattice sites, and the *on-site* Coulomb interaction U of two electrons at the same site, the short-range Coulomb matrix (2.5) obviously leads to additional interaction terms: The term V denotes the Coulomb interaction between electrons at neighbour sites. The interaction X, called *bond-charge* interaction, corresponds to a single particle hopping where the

hopping amplitude depends on the occupation number of the sites involved. In fact it is proportional to the charge (number of electrons) located at the bond $\langle ij \rangle$ between the sites i and j which motivates the name. Furthermore, J describes the *spin-spin* interaction and Y the *hopping of electron pairs* to neighbour sites. While the on-site interaction U usually has the largest numerical value, the other matrix elements are certainly not zero. Hubbard gave an estimation of the energies in the case of transition metals [22]:

$$U \approx 20\,\text{eV} > V \approx 2 - 3\,\text{eV} > X \approx 1\,\text{eV} > J, Y \approx 0.025\,\text{eV} . \qquad (2.9)$$

In a first approximation he therefore neglected all interaction terms except for the on-site Coulomb repulsion U and the single-particle hopping t, typically range between 0.5 eV and 1.5 eV, which is needed to describe the relevant physics correctly. This two term model

$$
\begin{aligned}
\mathcal{H}_{\text{Hub}} &= \mathcal{H}_{\text{t}} + \mathcal{H}_{\text{U}} \\
&= -t \sum_{\langle ij \rangle} \sum_{\sigma} \left(c^{\dagger}_{i,\sigma} c_{j,\sigma} + c^{\dagger}_{j,\sigma} c_{i,\sigma} \right) + U \sum_{i} n_{i,\uparrow} n_{i,\downarrow} \qquad (2.10)
\end{aligned}
$$

is known as the *pure one-band Hubbard model* or just *Hubbard model*. Despite of its simplicity rigorous results for the Hubbard model are still rare. The next section will explore what is known rigorously about this model.

2.2. Some rigorous results for any lattice dimension

One of the most fascinating questions concerns the magnetic properties of the ground state. For the pure Hubbard model Nagaoka's theorem [29], valid for arbitrary lattice dimension but restricted to a special lattice structure fulfilling the *connectivity* condition [30], predicts a ferromagnetic ground state in a special limit, i.e. a single hole in a half-filled lattice with infinitely repulsive interaction ($U = \infty$). For finite repulsion ($U < \infty$) but on special lattices Mielke and Tasaki were able to derive rigorous criteria for the stability of ferromagnetism [31]. Moreover, Lieb's theorem [32] states that on a bipartite lattice at half-filling the ground state has spin $S = ||B| - |A||/2$, where $|B|$ ($|A|$) is the number of sites in the B (A) sublattice[2]. Based on Brandt and Giesekus basic concepts for the construction of exact ground states [33] Kollar et al. presented a generalization of Nagaoka's theorem [34]. They considered the generalized Hubbard model and derived sufficient conditions for the stability of ferromagnetism.
Apart from magnetism in the Hubbard model, the question about the theoretical mechanism of superconductivity is fascinating too. Based on so-called η pairs Yang has shown that already the pure Hubbard model (2.10) exhibits off-diagonal long-range order (ODLRO) eigenstates [35]. Using the *optimum ground state* approach, which is a much simpler and clearer method for the construction of exact eigenstates than Brandt and Giesekus basic concept, or Strack and Vollhardt

---

[2]As an example, take a square lattice and add a site (belonging to $|A|$) at the center of each bond of this square lattice. Then $|A| = 2|B|$ and the ground state has a magnetization per site which is more like ferrimagnetism than ferromagnetism.

generalization [36], De Boer et al. have shown that a large class of generalized Hubbard Hamiltonian has superconducting ground states of η-pairing type [37]. For reviews of rigorous results about the Hubbard model in arbitrary dimensions see for instance [28, 38]. Some of the most significant results have been collected in the reprint volumes [39, 40, 41].

2.3. The Hubbard model in 1D

It is very instructive to consider the one-dimensional Hubbard model, because analytical and numerical tools are much more elaborated in one dimension. In particular, in one dimension an exact solution for the pure Hubbard model is available. This solution gives exact energies of the ground state and all the excited states in terms of the solution of a system of coupled nonlinear equations. For a one-dimensional L-site lattice with periodic boundary conditions (PBC), i.e. $c_{L+1,\sigma} = c_{1,\sigma}$, the Hamiltonian of the model written in a symmetric form is given by

$$
\begin{aligned}
\mathcal{H} &= \mathcal{H}_\mathrm{t} + U \sum_{\ell=1}^{L} \left(n_{\ell,\uparrow} - \frac{1}{2} \right) \left(n_{\ell,\downarrow} - \frac{1}{2} \right) \qquad (2.11) \\
&= \mathcal{H}_\mathrm{t} + \mathcal{H}_\mathrm{U} - \frac{U}{2} N + \frac{U}{4} L
\end{aligned}
$$

in which $U/2$ shift the chemical potential. The physical properties depend on two parameters, i.e. the interaction U/t and the band-filling $n = N/L$, where $N = \sum_{\ell,\sigma} n_{\ell,\sigma} = \sum_{\sigma} N_{\sigma}$ is the total number of particles.

2.3.1. Symmetries and limiting cases

The Hubbard Hamiltonian (2.11) has two important symmetries[3] [42]. First, the Hamiltonian is invariant under rotations in spin space. The corresponding $SU(2)$-spin algebra is generated by the operators

$$
S^+ = \sum_{\ell=1}^{L} c_{\ell,\uparrow}^\dagger c_{\ell,\downarrow}, \quad S^- = \sum_{\ell=1}^{L} c_{\ell,\downarrow}^\dagger c_{\ell,\uparrow} \quad \text{and} \quad S^z = \frac{1}{2} \sum_{\ell=1}^{L} \left(n_{\ell,\uparrow} - n_{\ell,\downarrow} \right) \quad (2.12)
$$

with commutation relation

$$
[S^+, S^-] = 2S^z, \quad [S^z, S^\pm] = \pm S^\pm \quad \text{and} \quad [\mathcal{H}, S^\mu] = 0, \qquad (2.13)
$$

for $\mu \in \{+, -, z\}$. Note that this $SU(2)$-spin algebra is also valid for the standard Hubbard model (2.10). The second type of symmetry is particular to the Hubbard model and relates sectors of different particle numbers. For lattices of even length L the $SU(2)$-symmetry is generated by the pseudospin or η-pairing operators

$$
\eta^- = \sum_{\ell=1}^{L} (-1)^\ell c_{\ell,\uparrow} c_{\ell,\downarrow}, \quad \eta^+ = \sum_{\ell=1}^{L} (-1)^\ell c_{\ell,\downarrow}^\dagger c_{\ell,\uparrow}^\dagger \text{ and } \eta^z = \frac{1}{2} \left(N - L \right) \quad (2.14)
$$

---

[3] Notice that these two symmetries are not restricted to the one-dimensional model.

with corresponding commutation relation

$$[\eta^+, \eta^-] = 2\eta^z, \quad [\eta^z, \eta^\pm] = \pm\eta^\pm \quad \text{and} \quad [\mathcal{H}, \eta^\mu] = 0. \qquad (2.15)$$

Of course, this result is not surprising since the η-operators can be obtained from the spin operators by a *particle-hole* transformation. The generators of both algebras commute with one-another and it seems that the Hubbard model has a $SU(2) \otimes SU(2)$ symmetry. However, the symmetry group is smaller, because the two $SU(2)$ symmetries are not completely independent. For fixed L one has

$$S^z + \eta^z = \frac{1}{2}\left(N_\uparrow - N_\downarrow\right) + \frac{1}{2}\left(N - L\right) = N_\downarrow - \frac{L}{2} \qquad (2.16)$$

which is always an integer as long as L is even. Therefore, the full symmetry group is

$$SO(4) = SU(2) \otimes SU(2)/Z_2. \qquad (2.17)$$

One should notice that odd number of lattice sites or more complicated interactions will conserve the spin rotation invariance (2.12) but in general not the "charge" $SU(2)$ invariance (2.14). This second symmetry will become the standard global $U(1)$ invariance which is associated with particle number conservation. There exist two discrete symmetries which can be used to identify the fundamental regions of the model. First, the Hamiltonian is invariant under exchange of up and down spins (spin-flip symmetry). Another symmetry, which leaves the Hamiltonian invariant, is the *particle-hole* symmetry. By employing the transformation

$$c_{\ell,\sigma} \to (-1)^\ell c^\dagger_{\ell,\sigma} \quad \text{and} \quad c^\dagger_{\ell,\sigma} \to (-1)^\ell c_{\ell,\sigma} \qquad (2.18)$$

maps the empty state $|0\rangle$ to the completely filled state $|\uparrow\downarrow\rangle$. Making use of these symmetries it is sufficient to investigate the Hubbard model only in the region $N \leq L$ and $N_\downarrow \leq N/2$, important for the Bethe ansatz.

In the case $t = 0$ (*atomic limit*) the motion of electrons is impossible and at half-filling the ground state contains exactly one electron per site, i.e. the system is insulating. This feature still holds for finite t and $U = \infty$. In the *free fermion* limit ($U = 0$) the model reduces to a system of non-interacting moving electrons (see appendix) and the ground state is metallic. Therefore, for finite value t and at some critical value U_c of the Coulomb repulsion one can expect a *metal-insulator* transition.

2.3.2. Exact solution: The Bethe ansatz

In 1967 Yang [43] used the (nested) Bethe ansatz (BA) to solve an 1D electron system with delta-function interaction. One year later Lieb and Wu [44] generalized Yang's solution to a lattice case, i.e. the Hubbard model. They reduced the problem of diagonalizing the Hamiltonian to solving a set of coupled nonlinear equations known as the *Lieb-Wu* equations and calculated the ground state energy of the system. Moreover, they showed that for arbitrary positive value U the model at half-filling is an insulator. In 1972 Takahashi derived an infinite set of nonlinear integral equations that determines the thermodynamics

of the Hubbard model [45]. By solving these equations in some limits, he was able to calculate the low temperature specific heat [46]. In the 80's Woynarovich studied the elementary excitation spectrum of the Hubbard model in more detail [47, 48, 49, 50] which was started ten years earlier, e.g. by Ovchinnikov [51] and Coll [52]. Furthermore, he presented the explicit form of the Bethe ansatz wave function. Klümper et al. developed a different method to solve the BA equations at half-filling, rederiving all known results at zero temperature [53]. Based on the representation of the $SO(4)$ symmetry of the Hubbard model Eßler and Korepin proved that the excitation spectrum at half-filling is given by the scattering states of only four elementary excitations which are called *holon*, *antiholon* and *spinon* with spin up or down, respectively [54]. There was also progress in the understanding of the algebraic structure of the Hubbard model. Shastry showed that the 1D Hubbard Hamiltonian commutes with a one-parameter family of *transfer matrices* of a new 2D classical integrabel model and displayed the form of the R-matrix explicitly [55]. Shiroishi and Wadati showed that the R-matrix, which underlies the integrability of the Hubbard model, satisfies the Yang-Baxter equation [56]. Martins and Ramos formulated in terms of the *quantum inverse scattering* method the algebraic Bethe ansatz solution of the one-dimensional Hubbard model [57]. Jüttner et al. used this result in the *quantum transfer matrix* approach to the thermodynamics [58]. In contrast to the traditional approach by Takahashi, this approach leads to a finite number of non-linear integral equations that determine the Gibbs free energy.

This is only a short historical overview about the exact results of the Hubbard model. For a review including a rather exhaustive list of references we refer the interesting reader to [59] or the more pedagogical article [60].

Bethe ansatz for a Hubbard chain with PBC

The Hubbard Hamiltonian (2.11) conserves the total number of electrons N and the total number of down spins $N_\downarrow$ and thus $N_\uparrow$. Therefore, one can use these two quantum numbers to label the eigenstates of Hamiltonian (2.11) which have the following second quantized form

$$\left| N, N_\downarrow \right\rangle = \binom{N}{N_\downarrow} \sum_{\{x_k\}} \phi_\sigma(x_1, \ldots, x_N) c^\dagger_{x_1,\sigma_1} \ldots c^\dagger_{x_N,\sigma_N} \left| 0 \right\rangle, \qquad (2.19)$$

where $\left| 0 \right\rangle$ denotes the vacuum state in the Fock space and $\sigma = (\sigma_1, \ldots, \sigma_N) \in S_N$ (element of the symmetric group) is arbitrary. The Schrödinger equation

$$\mathcal{H} \left| N, N_\downarrow \right\rangle = E \left| N, N_\downarrow \right\rangle \qquad (2.20)$$

implies following eigenvalue equation for ϕ

$$-\sum_{j=1}^{N} \sum_{s=\pm 1} \phi_\sigma(x_1, \ldots, x_j + s, \ldots, x_N) + U \sum_{j<k} \delta_{x_j, x_k} \phi_\sigma(x_1, \ldots, x_N)$$

$$= \left(E + \frac{U}{2} N - \frac{U}{4} L \right) \phi_\sigma(x_1, \ldots, x_N), \qquad (2.21)$$

where δ_{x_j,x_k} denotes the Kronecker delta and $t = 1$. Unphysical amplitudes ϕ where two electrons with the identical spin occupy the same site will not be considered due to the Fermi statistics of the c-operators. The case $N = 1$ is not interesting because one electron without interaction obviously describes a free fermion and equation (2.21) can be solved by $\phi_\sigma(x) = A_\sigma e^{ikx}$ with the energy $E = -2\cos k$. In the case of two particles ($N = 2$) equation (2.21) reduces to

$$-\phi_\sigma(x_1 - 1, x_2) - \phi_\sigma(x_1 + 1, x_2) - \phi_\sigma(x_1, x_2 - 1) - \phi_\sigma(x_1, x_2 + 1)$$
$$= -U\delta_{x_1,x_2}\phi_\sigma(x_1, x_2) + E'\phi_\sigma(x_1, x_2) , \qquad (2.22)$$

with $E' = E + U - UL/4$ and $\sigma = (\sigma_1, \sigma_2)$. For free electrons, i.e. as long as $x_1 < x_2$ or $x_1 > x_2$, the solution of (2.22) is just a superposition of plane waves. A scattering process takes place, when the two particles occupy the same site, i.e. $x_1 = x_2$. This scattering is purly elastic, which means that the energy is conserved and that the momenta of the two electrons are individually conserved, i.e. the electrons exchange their momenta. The expression for ϕ in these two cases can be written in a unified form that also anticipates the form of the expression for $N > 2$. Let Q be a permutation of the labels of coordinates, i.e. $Q = (Q_1, Q_2) \in \{(1, 2), (2, 1)\}$. For $x_{Q_1} \leq x_{Q_2}$ the form for ϕ is then given by

$$\phi_\sigma(x_1, x_2) = \sum_{P \in S_2} (-1)^P A_{\sigma_{Q_1} \sigma_{Q_2}}(k_{P_1}, k_{P_2}) e^{ik_{P_1} x_1 + ik_{P_2} x_2} , \qquad (2.23)$$

where $(-1)^P$ denotes the sign of the permutation. This is the famous *nested* Bethe ansatz form for the wavefunction ϕ. The continuity of the wavefunction at $x_1 = x_2$ requires the fulfillment of the following relation among the amplitudes:

$$A_{\sigma_1 \sigma_2}(k_1, k_2) - A_{\sigma_1 \sigma_2}(k_2, k_1) = A_{\sigma_2 \sigma_1}(k_2, k_1) - A_{\sigma_2 \sigma_1}(k_1, k_2) . \qquad (2.24)$$

In addition, substituting (2.23) into equation (2.22) with $x = x_1 = x_2$ yields the condition

$$\{[A_{\sigma_2 \sigma_1}(k_2, k_1) - A_{\sigma_1 \sigma_2}(k_1, k_2)] (e^{ik_1} - e^{-ik_1} - e^{ik_2} + e^{-ik_2})$$
$$-U [A_{\sigma_1 \sigma_2}(k_1, k_2) - A_{\sigma_1 \sigma_2}(k_2, k_1)]\}$$
$$+E' [A_{\sigma_1 \sigma_2}(k_1, k_2) - A_{\sigma_1 \sigma_2}(k_2, k_1)]$$
$$= -2(\cos k_1 + \cos k_2) [A_{\sigma_1 \sigma_2}(k_1, k_2) - A_{\sigma_1 \sigma_2}(k_2, k_1)] . \qquad (2.25)$$

This becomes an eigenvalue equation for the eigenvalue $E' = -2(\cos k_1 + \cos k_2)$ with eigenfunction $[A_{\sigma_1 \sigma_2}(k_1, k_2) - A_{\sigma_1 \sigma_2}(k_2, k_1)]$, if the expression in brackets $\{\ldots\}$ vanishes. One can express two of the four amplitudes $A_{\sigma_{Q_1} \sigma_{Q_2}}(k_{P_1}, k_{P_2})$ in terms of the other two. The vanishing condition then reads

$$A_{\sigma_1 \sigma_2}(k_2, k_1) = \frac{-U/2i}{\sin k_1 - \sin k_2 - U/2i} A_{\sigma_1 \sigma_2}(k_1, k_2)$$
$$+ \frac{\sin k_1 - \sin k_2}{\sin k_1 - \sin k_2 - U/2i} A_{\sigma_2 \sigma_1}(k_1, k_2) . \qquad (2.26)$$

Equation (2.26) has a natural interpretation in terms of a scattering process of two particles. In order to see this one has to rewrite it as

$$A_{\sigma_1 \sigma_2}(k_2, k_1) = \sum_{\sigma'_1, \sigma'_2} S_{\sigma_2 \sigma'_2}^{\sigma_1 \sigma'_1}(k_1, k_2) A_{\sigma'_1 \sigma'_2}(k_1, k_2) , \qquad (2.27)$$

where $S(k_1, k_2)$ is the *two-particle scattering matrix* with elements

$$S_{\sigma_2\sigma_2'}^{\sigma_1\sigma_1'}(k_1, k_2) = \frac{-U/2\mathrm{i}}{\sin k_1 - \sin k_2 - U/2\mathrm{i}}\delta_{\sigma_1,\sigma_2'}\delta_{\sigma_2,\sigma_1'}$$
$$+\frac{\sin k_1 - \sin k_2}{\sin k_1 - \sin k_2 - U/2\mathrm{i}}\delta_{\sigma_1,\sigma_1'}\delta_{\sigma_2,\sigma_2'}. \qquad (2.28)$$

The elements of the S-matrix (2.28) give two possibilities of a scattering process: The particles can pass each other without changing their momenta and spin, or alternatively, the particles exchange their spins so that after scattering particle one has momentum k_1 and spin σ_2 and particle two momentum k_2 and spin σ_1. An equivalent interpretation would be an exchange of momenta instead of spins. Expression (2.28) can be written in a compact operator form

$$S_{12}(\lambda) = \frac{\lambda + \mathrm{i}U/2\, P_{12}}{\lambda + \mathrm{i}U/2} \qquad (2.29)$$

with the momentum parametrization $\lambda = \sin k_1 - \sin k_2$ and the permutation operator of a pair of particles

$$P_{12} = P_{\sigma_2\sigma_2'}^{\sigma_1\sigma_1'} = \delta_{\sigma_1,\sigma_2'}\delta_{\sigma_2,\sigma_1'} = \begin{pmatrix} 1 & 0 & 0 & 0 \\ 0 & 0 & 1 & 0 \\ 0 & 1 & 0 & 0 \\ 0 & 0 & 0 & 1 \end{pmatrix}. \qquad (2.30)$$

In the final step one has to consider the effect of the periodic boundary conditions on the wavefunction, i.e.

$$\phi_\sigma(x_1 + L, x_2) = \phi_\sigma(x_1, x_2) \quad \text{and} \qquad (2.31)$$
$$\phi_\sigma(x_1, x_2 + L) = \phi_\sigma(x_1, x_2). \qquad (2.32)$$

This induces the following conditions on the amplitudes

$$A_{\sigma_{Q_1}\sigma_{Q_2}}(k_{P_1}, k_{P_2}) = \exp(\mathrm{i}k_{P_1}L)\, A_{\sigma_{Q_2}\sigma_{Q_1}}(k_{P_2}, k_{P_1}), \qquad (2.33)$$

where $P, Q \in S_2$ are arbitrary. Solution of (2.33) determine the quantization conditions for the momenta k_1 and k_2.

The generalization to $N \geq 3$ particles separates the Fock space of the Hamiltonian in $N!$ quadrants

$$X_Q \equiv \{1 \leq x_{Q_1} \leq x_{Q_2} \leq \ldots \leq x_{Q_N} \leq L\}. \qquad (2.34)$$

The corresponding N-particle Bethe ansatz wavefunction reads

$$\phi_\sigma(x_1, \ldots, x_N) = \sum_{P\in S_N}(-1)^P A_{\sigma_{Q_1}\ldots\sigma_{Q_N}}[Q, P]\exp\left(\mathrm{i}\sum_{j=1}^N k_{P_j}x_j\right), \qquad (2.35)$$

where the symbolic notation $A_{\sigma_{Q_1}\ldots\sigma_{Q_N}}[Q, P] \equiv A_{\sigma_{Q_1}\ldots\sigma_{Q_N}}(k_{P_1}, \ldots, k_{P_N})$ was used. The amplitudes of various regions are related through the S-matrix. If the regions
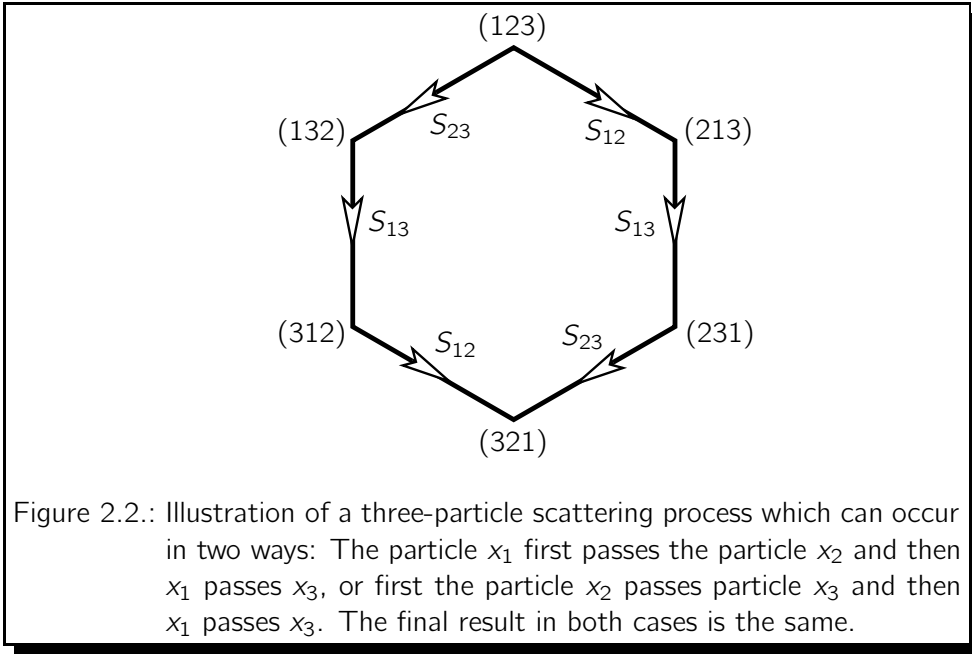
X_Q and $X_{\widetilde{Q}}$ differ by the exchange of particles i and j, then the relation can be written in the form

$$A_{\ldots\sigma_i\ldots\sigma_j\ldots}[Q,P] = \sum_{\sigma_i',\sigma_j'} S_{\sigma_j\sigma_j'}^{\sigma_i\sigma_j'}(k_i,k_j)A_{\ldots\sigma_i'\ldots\sigma_j'\ldots}[\widetilde{Q},P]\,. \tag{2.36}$$

Note that a repeated application of relation (2.36) for a single pair of particles reduces any permutation to the identity permutation I with

$$X_I \equiv \{1 \le x_1 \le x_2 \le \ldots \le x_N \le L\}\,. \tag{2.37}$$

This means that the amplitudes $A[\widetilde{Q},P]$ and $A[I,P]$ will be connected by the product of S-matrices corresponding to all transpositions of a pair of indices which are necessary to reduce the permutation $\widetilde{Q}$ to the identity permutation. However, the way how to express a permutation by a sequence of transpositions is usually not unique. For instance, if three particles in their initial state are ordered as $x_1 < x_2 < x_3 = (1,2,3)$ and after the passage of a certain amount of time their positions are $x_3 < x_2 < x_1 = (3,2,1)$, then the three-particle scattering process can be described in two ways, illustrated in Fig. 2.2. Thus equivalence plays a

Figure 2.2.: Illustration of a three-particle scattering process which can occur in two ways: The particle x_1 first passes the particle x_2 and then x_1 passes x_3, or first the particle x_2 passes particle x_3 and then x_1 passes x_3. The final result in both cases is the same.

fundamental role in the theory of exactly solvable one-dimensional models and was established by Yang [43] and Baxter [61] and becomes the basis for what is known as the *Yang-Baxter equation*

$$\sum_{\sigma_1',\sigma_2',\sigma_3'} S_{\sigma_2\sigma_2'}^{\sigma_1\sigma_1'}(k_1,k_2)S_{\sigma_3\sigma_3'}^{\sigma_1'\sigma_1''}(k_1,k_3)S_{\sigma_3'\sigma_3''}^{\sigma_2'\sigma_2''}(k_2,k_3) =$$

$$\sum_{\sigma_1',\sigma_2',\sigma_3'} S_{\sigma_3\sigma_3'}^{\sigma_2\sigma_2'}(k_2,k_3)S_{\sigma_3'\sigma_3''}^{\sigma_1\sigma_1'}(k_1,k_3)S_{\sigma_2'\sigma_2''}^{\sigma_1'\sigma_1''}(k_1,k_2)\,. \tag{2.38}$$

If the S-matrix derived from the Hamiltonian satisfies the Yang-Baxter equation, then the Bethe ansatz form of the wavefunction is consistent and the model is integrabel.

The expression obtained for the S-matrix of the Hubbard model (2.29) has the same form as the matrix, which was used to solve the *six-vertex* model exactly (see [61] for details). In order to see that the S-matrix (2.29) satisfies the Yang-Baxter equation one has to rewrite it explicitly in matrix form

$$
S(\lambda) = \frac{1}{\lambda + iU/2}
\begin{pmatrix}
\lambda + iU/2 & 0 & 0 & 0 \\
0 & \lambda & iU/2 & 0 \\
0 & iU/2 & \lambda & 0 \\
0 & 0 & 0 & \lambda + iU/2
\end{pmatrix}
\tag{2.39}
$$

and identify the matrix elements with the elements of the $\mathcal{L}$-matrix

$$
a(\lambda) = 1, \quad b(\lambda) = \frac{iU/2}{\lambda + iU/2} \quad \text{and} \quad c(\lambda) = \frac{\lambda}{\lambda + iU/2}.
\tag{2.40}
$$

The following relation holds between them

$$
a(\lambda) : c(\lambda) : b(\lambda) = (\lambda + iU/2) : \lambda : iU/2,
\tag{2.41}
$$

which automatically satisfies the functional equation

$$
\frac{c(\lambda)}{b(\lambda)} = \frac{c(\mu)}{b(\mu)} + \frac{c(\lambda - \mu)}{b(\lambda - \mu)},
\tag{2.42}
$$

moreover the Yang-Baxter equation in local form, from which (2.42) follows. Hence, one can apply all the technique which was used to solve the six-vertex model. For a prescribed choice of quantities λ_j^0, i.e. $\lambda_j^0 = \sin k_j$, and parametrization of the elements of the S-matrix (2.39) the eigenvalue of the *transfer matrix* T_j adopt the specific form

$$
\Lambda(\lambda = \lambda_j^0; \lambda_1^0 \ldots \lambda_N^0; \lambda_1 \ldots \lambda_{N_\downarrow}) = \prod_{i+1}^{N_\downarrow} \frac{\lambda_i - \sin k_j + iU/2}{\lambda_i - \sin k_j} \equiv e^{ik_j L}
\tag{2.43}
$$

and the numbers λ_i $(i = 1, \ldots, N_\downarrow)$ assume the following expression

$$
\prod_{j=1}^{N} \frac{\lambda_i - \sin k_j + iU/2}{\lambda_i - \sin k_j} = \prod_{k=1}^{N_\downarrow} \frac{\lambda_i - \lambda_k + iU/2}{\lambda_i - \lambda_k - iU/2}
\tag{2.44}
$$

The right hand side of equation (2.43) is due to the periodicity condition

$$
e^{ik_j L} A[I, I] = T_j A[I, I],
\tag{2.45}
$$

where relation (2.39) was used repeatedly to obtain the above expression for the amplitude $A[I, I]$ corresponding to the identity P- and Q-permutations. A substitution of the form $\lambda_i = \lambda_i' - iU/4$ changes expression (2.43) and (2.44) into the form written by Lieb and Wu, which are called Lieb-Wu equations.

Lieb-Wu equations for open boundary conditions

The Hubbard model with open boundary conditions was solved by Schulz using the Bethe ansatz technique [62]. Further examinations of Hubbard models including boundary chemical potentials or magnetic fields opened new possibilities to study quantum impurity problems (see e.g. [63, 64, 65]).

The Hubbard chain with boundary chemical potentials is given by

$$
\mathcal{H} = \ - \ t \sum_{\ell=1}^{L-1} \sum_{\sigma} \left(c_{\ell,\sigma}^{\dagger} c_{\ell+1,\sigma} + c_{\ell+1,\sigma}^{\dagger} c_{\ell,\sigma} \right) + U \sum_{\ell=1}^{L} n_{\ell,\uparrow} n_{\ell,\downarrow}
$$
$$
- \ p \sum_{\sigma} (n_{1,\sigma} + n_{L,\sigma}) \, . \tag{2.46}
$$

Using the notation of Ref. [66], the Lieb-Wu equations determing the spectrum of $\mathcal{H}$ in the N-electron sector and magnetization $M = N/2 - N_{\downarrow}$ read

$$
e^{ik_j 2L} \left(\frac{e^{ik_j} - p}{1 - pe^{ik_j}} \right)^2 \frac{\sin(k_j) + iU/4}{\sin(k_j) - iU/4} = \prod_{\beta=-N_{\downarrow}}^{N_{\downarrow}} \frac{\sin(k_j) - \lambda_{\beta} + iU/4}{\sin(k_j) - \lambda_{\beta} - iU/4} \, , \tag{2.47}
$$

$$
\frac{\lambda_{\alpha} + 2iU/4}{\lambda_{\alpha} - 2iU/4} \prod_{j=-N}^{N} \frac{\lambda_{\alpha} - \sin(k_j) + iU/4}{\lambda_{\alpha} - \sin(k_j) - iU/4} = \prod_{\substack{\beta=-N_{\downarrow} \\ \beta \neq \alpha}}^{N_{\downarrow}} \frac{\lambda_{\alpha} - \lambda_{\beta} + 2iU/4}{\lambda_{\alpha} - \lambda_{\beta} - 2iU/4} \, , \tag{2.48}
$$

where the identification $k_{-j} = -k_j$ and $\lambda_{-\alpha} = -\lambda_{\alpha}$ was used in order to simplify the equations. Of course, with $p = 0$ one directly obtains the case for open boundary conditions. The roots of the Lieb-Wu equations (2.47) and (2.48) are characterized by the so-called *charge rapidities* k_j with $j = -N, \ldots, N$ and *spin rapidities* λ_{α} with $\alpha = -N_{\downarrow}, \ldots, N_{\downarrow}$. The energy of the corresponding eigenstate of (2.46) has then the form

$$
E/t = 1 - \sum_{j=-N}^{N} \cos(k_j) \, , \tag{2.49}
$$

where the solutions $k = 0$ and $\lambda = 0$ have been excluded, since the Lieb-Wu equations (2.47) and (2.48) are already symmetrized.

In order to check the accuracy of our DMRG algorithm (see following chapter 3) we compared the ground state energy of the open Hubbard chain at various band fillings obtained by (2.47), (2.48) and (2.49) and our DMRG results. For this purpose we chose the logarithmic expression of Lieb-Wu equations and determined the set of rapidities by applying an IMSL routine like `DNEQNF` [67]. Additional checks have been done in the case of free fermions (see appendix B).

2.4. Superconductivity in extended Hubbard models

Since the discovery of quasi one-dimensional conductors and high-T_c supercon-ducting materials much effort has been devoted to the study of the pairing mech-anism in highly correlated electronic systems. While the search for 'superconduct-ivity' (characterized by dominant pairing correlations) in the Hubbard chain with

repulsive Coulomb interaction failed, a superconducting state with dominant on-site singlet-pairing correlations is realized in the *attractive* case, where a spin gap opens. An exact analysis of the Bethe ansatz solution by Kawakami and Yang [16] showed that this pairing correlation function behaves like $\langle \mathcal{O}_{\mathrm{OS}}^\dagger(0)\mathcal{O}_{\mathrm{OS}}(r)\rangle \sim 1/r^\beta$ at large separations r between pairs. The non-universal exponent β is a function of U/t and the band filling.

However, the pure Hubbard model is limited in its applicability to real materials. For instance, the properties of conducting polymers can not be explained without invoking a least a nearest-neighbour Coulomb interaction. Therefore, various more realistic extensions of the pure Hubbard model have been considered.

2.4.1. The extended Hubbard model

The Hamiltonian of the Hubbard model with nearest-neighbour Coulomb interaction V is given by

$$
\begin{aligned}
\mathcal{H} &= \mathcal{H}_{\mathrm{Hub}} + \mathcal{H}_{\mathrm{V}} \\
&= -t\sum_{\ell=1}^{L}\sum_{\sigma}\left(c_{\ell,\sigma}^\dagger c_{\ell+1,\sigma} + c_{\ell+1,\sigma}^\dagger c_{\ell,\sigma}\right) + U\sum_{\ell=1}^{L} n_{\ell,\uparrow}n_{\ell,\downarrow} + V\sum_{\ell=1}^{L} n_\ell n_{\ell+1}
\end{aligned}
\tag{2.50}
$$

and it is called *extended* Hubbard model. In contrast to the pure Hubbard model, this Hamiltonian is no longer exactly solvable. However, the model has been extensively studied by the weak coupling theory based on the bosonization technique and renormalization group (RG) analysis [68, 9, 69] and numerical calculations using exact diagonalization, quantum Monte-Carlo simulations or DMRG method [70, 71, 72, 73]. The weak-coupling phase diagram consists of two insulating
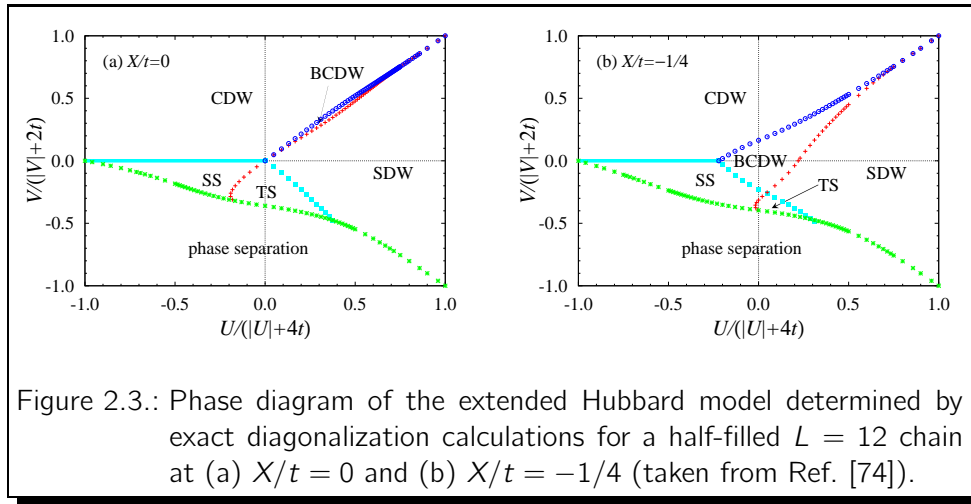
Figure 2.3.: Phase diagram of the extended Hubbard model determined by exact diagonalization calculations for a half-filled $L = 12$ chain at (a) $X/t = 0$ and (b) $X/t = -1/4$ (taken from Ref. [74]).

phases, the spin-density-wave (SDW) phase and the charge-density-wave (CDW) phase, which are separated by a transition line located at $U = 2V$. The metallic phases are described by dominating singlet (SS) and triplet (TS) superconducting correlations. In the most interesting region ($U, V > 0$), the weak-coupling RG studies [68, 9] show that there is a continuous phase transition between SDW

and CDW along the line $U = 2V$. In the strong coupling limit ($U, V \gg 1$) the SDW-CDW transition is discontinuous (first-order) and the phase boundary is slightly shifted away from the line $U = 2V$ [70].

Quite recently, Nakamura found numerically that for small to intermediate values of U and V, the SDW and CDW phases are disjoined by the bond-charge density wave (BCDW) phase [74] which is characterized by the operator:

$$\mathcal{O}_{\text{BCDW}} \equiv (-1)^{\ell} \sum_{\sigma} (c_{\ell,\sigma}^{\dagger} c_{\ell+1,\sigma} + \text{h.c.}). \tag{2.51}$$

To clarify this mechanism of the transition, he also investigated the effect of the bond-charge interaction X which leads to an enlargement of the BCDW region (see also Fig. 2.3). He concluded that SDW-BCDW and BCDW-CDW transitions are continuous and that these two transition lines merge at a tricritical point into the first-order line separating the CDW and SDW phases.
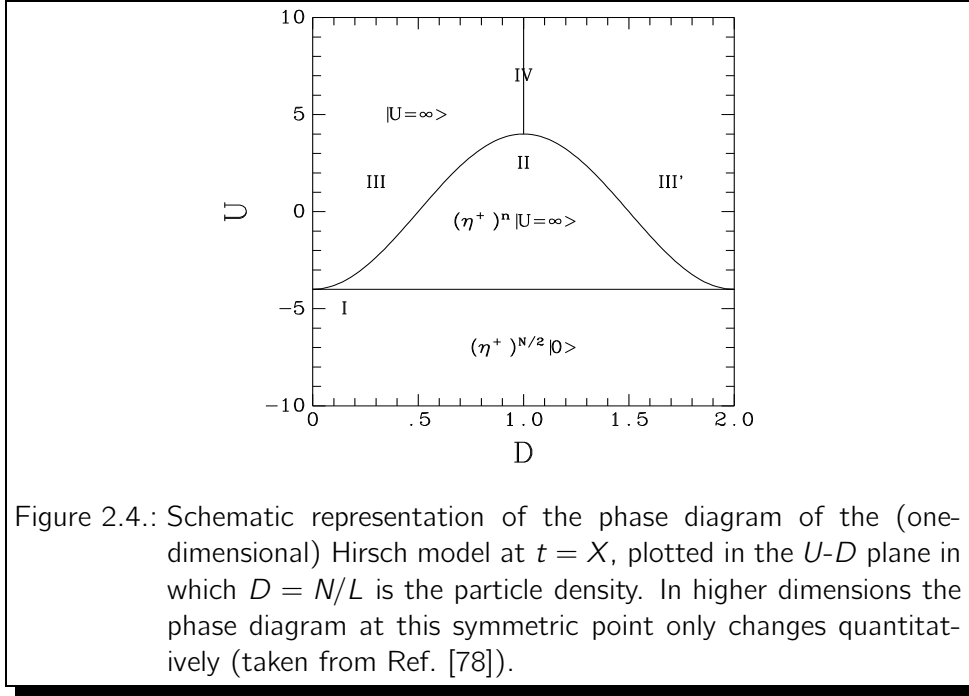
2.4.2. The Hirsch model

The extended Hubbard model (2.50) with bond-charge interaction X was proposed by Hirsch for the description of oxide superconductors by considering holes as the charge carriers [75, 76]. The one-dimensional Hamiltonian without nearest-neighbour Coulomb interaction V, which we call Hirsch model, reads

$$\begin{aligned}
\mathcal{H} &= \mathcal{H}_{\text{Hub}} + \mathcal{H}_{\text{X}} \tag{2.52} \\
&= \mathcal{H}_{\text{Hub}} + X \sum_{\ell=1}^{L} \sum_{\sigma} \left(c_{\ell,\sigma}^{\dagger} c_{\ell+1,\sigma} + c_{\ell+1,\sigma}^{\dagger} c_{\ell,\sigma} \right) \left(n_{\ell,-\sigma} + n_{\ell+1,-\sigma} \right).
\end{aligned}$$

Due to charge and spin conservation the model exhibits $\text{U}(1) \otimes \text{SU}(2)$ symmetry. The Hamiltonian with $U = 0$ and a modified version of $\mathcal{H}_{\text{X}}$, called Bariev model[4], has been solved by Bethe ansatz [77]. In contrast to the Hirsch model only the S^z generator commutes with the Bariev Hamiltonian which indicates a $\text{U}(1) \otimes \text{U}(1)$ symmetry. Applying the Lanczos technique Quaisser proved that various ground-state properties of the Bariev model and (2.52) with $U = 0$ indicate similar behaviour as long as the bond-charge repulsion X is small [11, 79]. In addition, he concluded that for $X \approx 0.5$ the pair correlations are strongest in both models. In the high-symmetric case $t = X$ zero and finite temperature properties of the Hirsch model have been exactly derived. Schadschneider [78] and Arrachea and Aligia [80] determined the phase diagram at zero temperature shown in Fig. 2.4. In regimes I and II the system is described by superconducting states of η-pairing type, where η-pairs are inserted in the empty lattice or the ground-state of an $U = \infty$ Hubbard model. These states show ODLRO

$$\lim_{|i-j| \to \infty} \langle \psi_\eta | \mathcal{O}_{\text{OS}}^{\dagger}(i) \mathcal{O}_{\text{OS}}(j) | \psi_\eta \rangle \neq 0 \quad \text{with} \quad \mathcal{O}_{\text{OS}}^{\dagger}(i) = c_{i,\uparrow}^{\dagger} c_{i,\downarrow}^{\dagger}. \tag{2.53}$$

---

[4]Bariev considered in his original work [77] a model consisting of two isotropic XY chains coupled by three-spin interactions. By using the Jordan-Wigner transformation the Hamiltonian can be presented in terms of fermionic creation and annihilation operators, which is known as the Bariev model.

Figure 2.4.: Schematic representation of the phase diagram of the (one-dimensional) Hirsch model at $t = X$, plotted in the U-D plane in which $D = N/L$ is the particle density. In higher dimensions the phase diagram at this symmetric point only changes quantitatively (taken from Ref. [78]).

The physics of III ($n < 1$) is the same as that of a the $U = \infty$ Hubbard model, i.e. without doubly occupied sites. Due to the particle-hole symmetry regime III' ($n > 1$) is equivalent to III, however no empty sites occur. For $n = 1$, phase IV, the ground state is an insulator.

The thermodynamics was studied by Dolcini and Montorsi [81]. The non-integrable regime $0 < X < 1$ was intensively studied by Kemper using the transfer-matrix DMRG [82, 83].
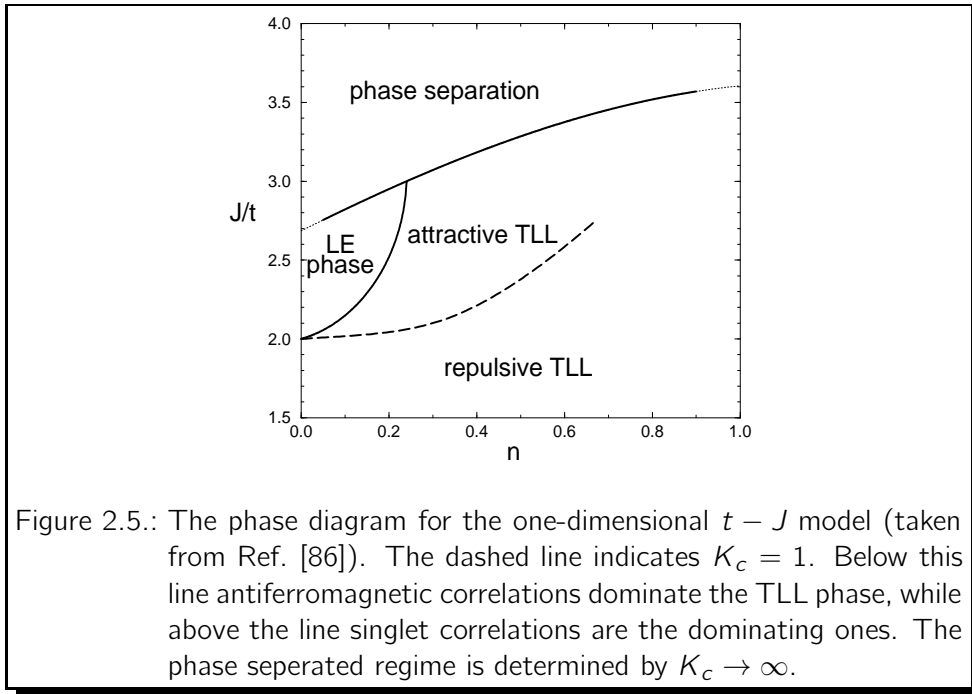
2.4.3. The $t - J$ model

In the limit $U \to \infty$ doubly occupied lattice sites are forbidden. After projecting out the states in the Hilbert space involving double occupancies one finds in second order in t/U the following effective Hamiltonian

$$
\begin{aligned}
\mathcal{H}_{\text{t-J}} \;=\; & -t \sum_{\ell=1}^{L} \sum_{\sigma} \left\{ (1 - n_{\ell,-\sigma})\, c_{\ell,\sigma}^{\dagger} c_{\ell+1,\sigma} (1 - n_{\ell+1,-\sigma}) + \text{h.c.} \right\} \\
& + J \sum_{\ell=1}^{L} \left(\mathbf{S}_\ell \cdot \mathbf{S}_{\ell+1} - \frac{n_\ell n_{\ell+1}}{4} \right) ,
\end{aligned}
\tag{2.54}
$$

where $J = 2t^2/|U|$. This model was solved exactly at the *super-symmetric* point $J/t = 2$ by applying the Bethe ansatz technique [84, 85] and for the limiting case $J \to 0$, which is equivalent to the $U \to \infty$ Hubbard model.

From the analysis, supported by various numerical calculations (e.g. [87, 88]), it is known that the $t - J$ model belongs to the universality class of a Tomonaga-Luttinger liquid (TLL). The remaining parameter region at $J/t > 2$ was first

Figure 2.5.: The phase diagram for the one-dimensional $t - J$ model (taken from Ref. [86]). The dashed line indicates $K_c = 1$. Below this line antiferromagnetic correlations dominate the TLL phase, while above the line singlet correlations are the dominating ones. The phase seperated regime is determined by $K_c \to \infty$.

analyzed by Ogata et al. [87] using the exact diagonalization. For $J/t = 2.8$ to 3.5 depending on the electron density a phase separation takes place, where the system is separated into electron-rich and hole-rich phases. A third phase with a spin gap (SG) was found at low densities and $2 < J/t < 3.1$. The complete phase diagram is shown in Fig. 2.5.

3. The density matrix renormalization group technique

The solution of a (stationary) Schrödinger equation is equivalent to the solution of a high-dimensional eigenvalue problem. This eigenvalue problem can be solved numerically by diagonalizing the Hamiltonian matrix with standard eigenvalue routines on computer. Most of these routines [89] use computer memory instead of 'harddisk memory' as an efficient way to save the data. However, this is restricted to the available free memory.

In order to get the matrix elements of the Hamiltonian one has to choose a proper orthonormal basis in the Hilbert space $\mathfrak{H}$, like the occupation number basis that includes states describing all possible distributions of N electrons on L lattice sites. The size of $\mathfrak{H}_L$ grows exponentially with the number of sites L. For instance, a fermionic spin-1/2 model with four possible occupancies at each lattice site (vacant, singly occupied with either up-spin or down-spin and doubly occupied with one up-spin and one down-spin) has 4^L degrees of freedom. When $L = 16$, the dimension of $\mathfrak{H}_L$ is already $4\,294\,967\,296$ and the corresponding Hamilton matrix has more than 10^{19} elements. Therefore, it is important to be as efficient as possible.

One way to reduce $\mathfrak{H}_L$ into invariant subspaces, which finally transforms the Hamiltonian matrix into a block-diagonal form, is to use symmetries. The simplest symmetry is associated with the conservation of the total number of electrons N. In addition, when translational symmetry is present, the momentum is conserved and all states can be grouped by the wave number. This leads to a further reduction of $\mathfrak{H}_L$. Using both symmetries, the largest block matrix of the previous example has still over 10^{14} elements and one has to store more than 10^5 GBytes of memory, too large for most computers. However, Hamiltonian matrices of current quantum models are extremely sparse.

An effective algorithm for diagonalizing sparse matrices was proposed by Lanczos in 1950 [90]. The procedure reduces a high-dimensional eigenvalue problem to a small one without storing the original matrix. Consequently less memory will be required but memory limitations will still impose restrictions on the system size.

Examination of larger systems needs another methods like the *density matrix renormalization group* (DMRG) approach that was formulated by White in 1992 [91, 92]. In contrast to other numerical methods, such as *quantum Monte-Carlo* simulations [93], the DMRG technique offers a powerful tool for determing accurate approximations to the ground state and the low-lying excited states of low-dimensional strongly correlated systems.

The subject of this chapter will be the detailed description of the Lanczos method

and the DMRG approach, which represent the main numerical tool of the present thesis.

3.1. Exact diagonalization: The Lanczos method

3.1.1. Invariant subspace

The concept of an *invariant subspace* is the most important point for understanding the Lanczos method. From linear algebra we know, that a subspace that is spanned by m linear independent vectors $|q_1\rangle, \ldots, |q_m\rangle$ is invariant under $\mathcal{H}$, a $n \times n$ hermitian matrix, if for any vector $|q\rangle$ in the subspace the vector $\mathcal{H}|q\rangle$ is also in the subspace. In the following we will denote the $\mathcal{H}$-invariant subspace by $\mathfrak{K}$. What does this invariance mean? If Q_m is a $n \times m$ matrix whose columns are the orthonormal vectors $|q_k\rangle$, then the matrix product $\mathcal{H}Q_m$ is a $n \times m$ matrix too and the columns are linear combinations of the columns of Q_m. Assuming that the $|q_k\rangle$ form an orthonormal basis in $\mathfrak{K}$, i.e. $Q_m^t Q_m = \mathrm{id}_m$, one can find a $m \times m$ matrix T_m which satisfies the relation

$$\mathcal{H}Q_m = Q_m T_m \quad \Leftrightarrow \quad Q_m^t \mathcal{H}Q_m = T_m. \tag{3.1}$$

This means that the eigenpairs of a large matrix $\mathcal{H}$ can be found from those of a smaller matrix T_m. For instance, let λ and $|\phi\rangle$ be an eigenpair of T_m. Multiplication of $T_m|\phi\rangle = \lambda|\phi\rangle$ by Q_m and the use of relation (3.1) leads to the equivalence

$$Q_m T_m|\phi\rangle = \lambda Q_m|\phi\rangle \quad \Leftrightarrow \quad \mathcal{H}Q_m|\phi\rangle = \lambda Q_m|\phi\rangle, \tag{3.2}$$

where λ and $Q_m|\phi\rangle$ describe an eigenpair of $\mathcal{H}$. The Lanczos algorithm approximately generates such an invariant subspace $\mathfrak{K}$.

3.1.2. The algorithm

The first step in the procedure is to select an arbitrary but nonzero vector $|q_0\rangle$ which belongs to the Hilbert space $\mathfrak{H}$ of the model being studied. If some information about the ground state is known, like total momentum or spin, then it is convenient to start the iteration with a vector already belonging to the subspace having those quantum numbers. Otherwise, it is convenient to select an initial vector with randomly chosen coefficients. After $|q_0\rangle$ is selected, a new vector can be defined by multiplying the hermitian matrix $\mathcal{H}$ with the initial vector. However, to ensure the orthogonality $\langle q_0|q_1\rangle = 0$ one has to subtract the projection onto $|q_0\rangle$. Together one obtains

$$|q_1\rangle = \mathcal{H}|q_0\rangle - \langle q_0|\mathcal{H}|q_0\rangle|q_0\rangle. \tag{3.3}$$

An additional vector that is orthogonal to the previous two, i.e. $\langle q_0|q_2\rangle = 0$ and $\langle q_1|q_2\rangle = 0$, can be constructed as

$$|q_2\rangle = \mathcal{H}|q_1\rangle - \langle q_1|\mathcal{H}|q_1\rangle|q_1\rangle - \langle q_1|\mathcal{H}|q_0\rangle|q_0\rangle. \tag{3.4}$$

It can be easily checked that the orthogonality conditions are fulfilled. This procedure can be generalized by defining an orthogonal basis recursively. For each $k = 0, 1, \ldots$ one then gets

$$|q_{k+1}\rangle = \mathcal{H}|q_k\rangle - \alpha_k|q_k\rangle - \beta_k|q_{k-1}\rangle, \tag{3.5}$$

where the coefficients are given by

$$\alpha_k = \langle q_k|\mathcal{H}|q_k\rangle \quad \text{and} \quad \beta_k = \langle q_k|\mathcal{H}|q_{k-1}\rangle. \tag{3.6}$$

Of course, for all $\ell \leq k - 1$ one obtains $\langle \ell|k\rangle = 0$ and for $k = 0$ one has to set $\beta_0 \equiv 0$ and $|q_{-1}\rangle \equiv 0$. After $k = m$ steps a set of orthogonal vectors $|q_k\rangle$ has been generated. Normalizing them by $|q_k^\circ\rangle \equiv |q_k\rangle/\beta_k$ leads to an orthonormal matrix Q_m whose columns are filled with the vectors $|q_k^\circ\rangle$. By applying formula (3.1) the Hamiltonian matrix $\mathcal{H}$ will be transformed into a tridiagonal form (cf. with Fig. 3.1). If m is sufficiently large, the eigenvalues λ of the Lanczos matrix T_m should be good approximations[1] of the eigenvalues of $\mathcal{H}$ which are restricted to the invariant subspace

$$\mathfrak{K}_m = \text{span}\left\{|q_0^\circ\rangle, \mathcal{H}|q_0^\circ\rangle, \mathcal{H}^2|q_0^\circ\rangle, \ldots, \mathcal{H}^{m-1}|q_0^\circ\rangle\right\}, \tag{3.7}$$

known as Krylov subspace. To be more precise, the algorithm is repeated until

$$\frac{|\lambda_0(m) - \lambda_0(m-1)|}{|\lambda_0(m)|} < \varepsilon, \tag{3.8}$$

where ε is a small number, typically of magnitude 10^{-10} and $\lambda_0(m)$ is the lowest or largest eigenvalue at $k = m$.

The Lanczos algorithm is similar to the Gram-Schmidt orthonormalization (GSO) process. However, the GSO process applied to $\mathfrak{K}_m$ is expensive, since the cost is $\mathcal{O}(m^2)$. In contrast, the Lanczos algorithm delivers the same result but in an $\mathcal{O}(m)$ process. The crucial point is that, to compute $|q_m^\circ\rangle$, one uses $\mathcal{H}|q_{m-1}^\circ\rangle$ instead of $\mathcal{H}^m|q_0^\circ\rangle$.
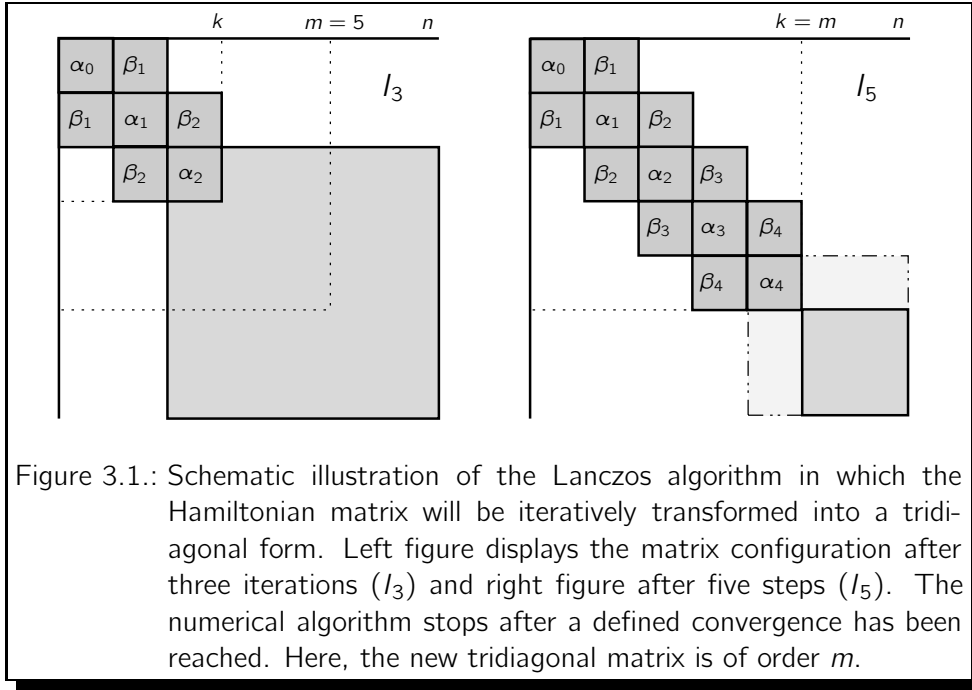
3.1.3. Numerical implementation

The main aim in the numerical realization of the Lanczos algorithm is to keep computational effort low. The most expensive operation is the matrix-vector multiplication $\mathcal{H}|q_k^\circ\rangle$. In addition, the Hamiltonian matrix cannot be stored in computer memory (already for small spin-1/2 systems one has to allocate more than 10^5 GBytes of memory) and one has to generate the matrix at each iteration step. However, the calculation of α_k can be modified if one introduces a new vector

$$|v_k\rangle \equiv \mathcal{H}|q_k^\circ\rangle - \beta_k|q_{k-1}^\circ\rangle, \tag{3.9}$$

which permits the relation

$$\alpha_k = \langle q_k^\circ|\mathcal{H}|q_k^\circ\rangle = \langle q_k^\circ|v_k\rangle. \tag{3.10}$$

---

[1]Note that the error increases as one proceeds into the spectrum. Therefore, for extremal eigenvalues one expects a higher accuracy than for eigenvalues in the middle of the spectrum.

Figure 3.1.: Schematic illustration of the Lanczos algorithm in which the Hamiltonian matrix will be iteratively transformed into a tridiagonal form. Left figure displays the matrix configuration after three iterations (I_3) and right figure after five steps (I_5). The numerical algorithm stops after a defined convergence has been reached. Here, the new tridiagonal matrix is of order m.

Consequently, relation (3.5) can be expressed in the less expensive form

$$|q_{k+1}\rangle = |v_k\rangle - \alpha_k|q_k\rangle, \qquad (3.11)$$

in which the number of matrix-vector multiplications is reduced to one per iteration step. The number of iterations depends on the model being studied, but typically one needs only $m = 60 - 120$ steps to get the extreme eigenvalues of the higher-dimensional Hamiltonian matrix $\mathcal{H}$.

3.2. Density matrix renormalization group (DMRG)

The density matrix renormalization group algorithm, developed by White in 1992 [91, 92], nowadays belongs to the standard numerical tools for studying low-dimensional spin and lattice systems with short-range interactions. The basic idea is to build up the system iteratively, starting with a small one that can be diagonalized exactly. The exponentially increasing Hilbert space is controlled by a proper selection of states which keeps the dimension constant.
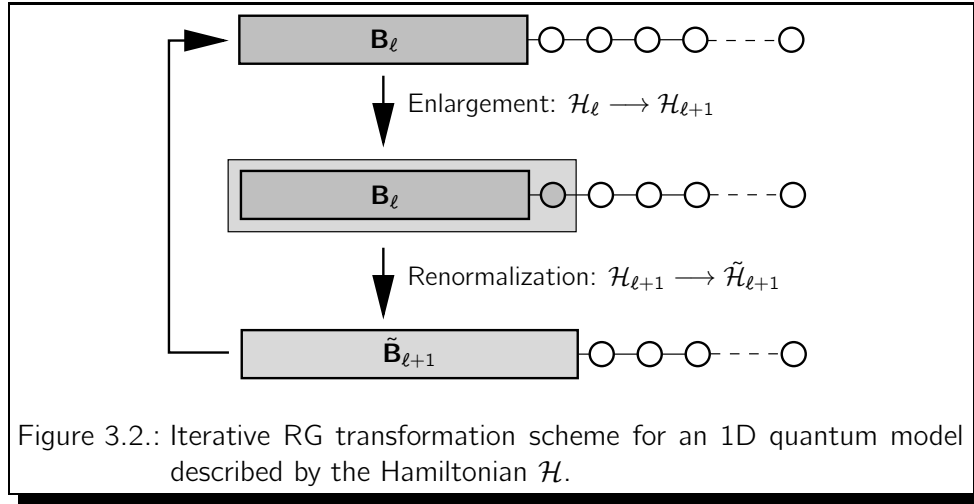
Its remarkable accuracy was already demonstrated in the original paper by White on the basis of a spin-one Heisenberg chain by computing the ground state energy for a lattice of hundreds of sites with a precision of order 10^{-10} and with a marginal amount of computational effort. Since then the method has been applied to a great variety of low-dimensional systems showing similar accuracy.

Apart from ground state properties the inclusion of temperature and the calculation of dynamical and time-dependent properties is possible too. For instance, the transfer-matrix DMRG (TMRG) permits the study of thermodynamic properties. An overview about the great variety of applications can be found in [94].

In the remaining sections we give a complete description of the DMRG algorithm including numerical details. First of all, we outline the concept of Wilson's numerical renormalization group method which is the basic module of the DMRG technique.

3.2.1. Numerical renormalization group (NRG)

The roots of the DMRG technique goes back to Wilson's numerical variant of renormalization group (RG) procedure [95, 96]. The basic idea of the (real-space) NRG is to truncate unimportant degrees of freedom using a sequence of RG transformations (cf. with Fig. 3.2). To be more concrete, the RG sequence

Figure 3.2.: Iterative RG transformation scheme for an 1D quantum model described by the Hamiltonian $\mathcal{H}$.

starts with a quantum chain of length $\ell + 1$, within the DMRG terminology also called *block*, which is sufficiently small thus the local Hamiltonian $\mathcal{H}_{\ell+1}$ can be diagonalized exactly. After diagonalizing $\mathcal{H}_{\ell+1}$ numerically, the m lowest eigenpairs $\{e_i, |v_i\rangle\}$ are selected to transform $\mathcal{H}_{\ell+1}$ and other operators $\mathcal{O}_{\ell+1}$ in block $\mathbf{B}_{\ell+1}$ to a reduced basis. The remaining eigenpairs are neglected. This can be realized by forming a projector matrix $\mathcal{P}$ in which the columns contain the m lowest eigenvectors $|v_i\rangle$ of the Hamiltonian $\mathcal{H}_{\ell+1}$, i.e.

$$\mathcal{P} \equiv \begin{pmatrix} | & | & & | \\ |v_1\rangle & |v_2\rangle & \cdots & |v_m\rangle \\ | & | & & | \end{pmatrix} . \tag{3.12}$$

Thus, applying truncation relation

$$\tilde{\mathcal{H}}_{\ell+1} = \mathcal{P}^\dagger \mathcal{H}_{\ell+1} \mathcal{P} \tag{3.13}$$

irrelevant information will be projected out. The effective Hamiltonian $\tilde{\mathcal{H}}_{\ell+1}$ is then a diagonal $m \times m$ matrix. Of course, other operators in $\mathbf{B}_{\ell+1}$ have to be transformed in the same way. The procedure can be repeated if one replaces $\tilde{\mathcal{H}}_{\ell+1}$ with $\mathcal{H}_\ell$. However, in order to form a new Hamiltonian $\mathcal{H}_{\ell+1}$ by adding one site to $\mathcal{H}_\ell$, the interaction between $\mathbf{B}_\ell$ and a single site must be reconstructed. We will give an instruction in Sec. 3.2.5.

The exponentially growing dimension of the Hilbert space $\mathfrak{H}$ is now controlled by the truncation number m which is typically fixed at each enlargement step of the NRG algorithm. Therefore, the required time and memory for each diagonalization stays the same.

The NRG procedure was successfully applied to the single impurity Kondo problem by Wilson [96]. However, further NRG studies of the 1D Heisenberg and Hubbard model showed that the accuracy becomes quite poor after a few iteration steps [97, 98]. White realized that the choice of energetically *lowest* eigenstates as relevant states in a RG step is usually not adequate. He solved this problem by a density matrix (DM) projection in which the *largest* eigenstates of the DM play a fundamental role at each renormalization step.

3.2.2. Density matrix projection

Following Ref. [91, 99], we will show that the DM projection provides an useful truncation prescription for the basis of the Hilbert space $\mathfrak{H}$.

At the beginning, we seperate an 1D quantum chain that is represented by the so-called *superblock*, into two chains. One part of the chain, the *system block*, is considered to be embedded in the superblock, whereas the second part acts as *environment* (cf. with Fig. 3.3). Without loss of generality, we assume that $\mathfrak{H}_{\mathrm{sys}}$

$$\mathbf{B}_5^{\mathrm{sys}} = \mathbf{B}_4 + \mathbf{S} \qquad \mathbf{B}_5^{\mathrm{env}} = \mathbf{S} + \mathbf{B}_4$$
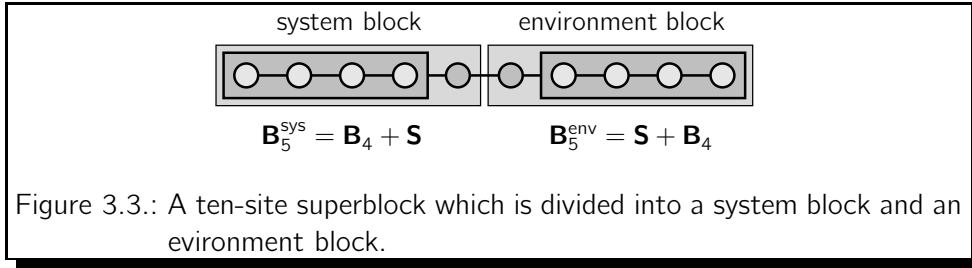
Figure 3.3.: A ten-site superblock which is divided into a system block and an evironment block.

and $\mathfrak{H}_{\mathrm{env}}$ have the same dimension $d \equiv d_B \times d_S$, spanned by orthonormal sets of eigenstates $\{|i\rangle_{\mathrm{sys}}\}$ and $\{|j\rangle_{\mathrm{env}}\}$, respectively. The ground state, which is also called *target* state has then the following expression

$$|\psi\rangle = \sum_{i,j} \psi_{ij} |i\rangle_{\mathrm{sys}} \otimes |j\rangle_{\mathrm{env}} \,. \tag{3.14}$$

The aim is to approximate the ground state by $m < d$ orthonormal states $|u_i\rangle_{\mathrm{sys}}$, characterizing the basis of the new truncated Hilbert space $\mathfrak{H}'_{\mathrm{sys}}$, so that

$$|\psi\rangle \approx |\tilde{\psi}\rangle = \sum_{i,j} \tilde{\psi}_{ij} |u_i\rangle_{\mathrm{sys}} \otimes |j\rangle_{\mathrm{env}} \,. \tag{3.15}$$

If it is not necessary, we will ignore the subscript. In order to find the optimal truncated basis one has to minimize the functional

$$S(|\tilde{\psi}\rangle) \equiv \big\| |\psi\rangle - |\tilde{\psi}\rangle \big\|^2 \,. \tag{3.16}$$

Since the coefficients $\psi_{ij} = \langle ij|\psi\rangle$ and $\tilde{\psi}_{ij} = \langle ij|\tilde{\psi}\rangle$ are (real-valued) matrix elements which belong to $d \times d$ matrices, the functional equation (3.16) can be

transformed to a more useful matrix representation

$$S(\tilde{\psi}) = \text{tr}\left\{(\psi - \tilde{\psi})^\dagger(\psi - \tilde{\psi})\right\} . \tag{3.17}$$

Now, we will show that Eq. (3.16) is minimized if the $|u_i\rangle$ are represented by the eigenvectors of the m largest eigenvalues w_i of the *reduced* density matrix

$$\rho_{ii'} = \sum_j \psi_{ij}\psi_{i'j} , \tag{3.18}$$

which is the projection of the ground state of the superblock on $\mathfrak{H}_{\text{sys}}$. Note that ρ is a hermitian operator and the condition $\text{tr}(\rho) = 1$ is fulfilled because of the normalized target state. One can simplify Eq. (3.17) by the application of the *singular value decomposition* theorem [100]. According to the theorem there exist two unitary $d \times d$ matrices U and V and a diagonal matrix D with non-negative elements σ_i, such that

$$\psi = U D V^\dagger . \tag{3.19}$$

The elements σ_i, called singular values, are the square roots of the eigenvalues w_i of ρ, because

$$\rho = U D^2 U^\dagger . \tag{3.20}$$

Using Eq. (3.19) and applying the theorem to the approximated state too, the functional equation (3.17) simplifies to

$$S(\tilde{\psi}) = \text{tr}\left\{(D - \tilde{D})^\dagger(D - \tilde{D})\right\} . \tag{3.21}$$

where $\tilde{D} \equiv U^\dagger \tilde{\psi} V$. It is obvious that the functional S is minimized by a diagonal matrix $\tilde{D}$ of rank m, whose elements are the largest singular values. Finally, the explicit form of the optimal approximated state reads

$$\tilde{\psi} = U \tilde{D} V^\dagger \quad \text{with} \quad \tilde{D} = \begin{pmatrix} \sigma_1 & & & \\ & \ddots & & \\ & & \sigma_m & \\ & & & 0 \end{pmatrix} , \tag{3.22}$$

where the entries are sorted by magnitude. Therefore, the largest eigenvectors of the reduced DM represent in a good approximation the ground state of the superblock. Note that the singular value decomposition does not play a role within the DMRG algorithm. The theorem was only used to show how an optimal basis of the truncated Hilbert space $\mathfrak{H}'_{\text{sys}}$ can be found.

Of course, other types of DM are possible. For instance, in the study of electron models, such as Hubbard or $t - J$ model, the electron density has to be fixed[2] at each DMRG iteration. For this reason, one has to construct the reduced density matrix from two target states. To be more precise [101], if the desired density is n and the superblock is of size L, then one can always find two nearest integers N_1 and N_2 such that $N_1 \leq nL \leq N_2$. Assuming that $|\psi(N_1)\rangle$ is the ground state

---

[2]Note that in a DMRG process only two sites are added at each step, which makes the half-filling and quarter-filling case invariant.

of N_1 electrons and $|\psi(N_2)\rangle$ is that of N_2 electrons, the corresponding DM then reads

$$\rho_{ii'} = W_1 \sum_j \psi_{ij}(N_1)\psi_{i'j}(N_1) + W_2 \sum_j \psi_{ij}(N_2)\psi_{i'j}(N_2)\,, \qquad (3.23)$$

where the weights W_k has to satisfy the condition

$$nL = W_1 N_1 + W_2 N_2 \quad \text{and} \quad W_1 + W_2 = 1\,. \qquad (3.24)$$

It is obvious that these construction ensures the constant band filling at every iteration. However, the success of this construction is guaranteed as long as the ground state is not described by a phase separation regime.

In addition, the DM can be easily adapted to obtain thermodynamic quantities of the quantum model being studied (see e.g. Ref. [102]). One only has to target several excited states when building the reduced DM. However, the accuracy decreases as more states are targeted. Therefore, it is most accurate to target only the ground state of the superblock if ground state properties are of interest.
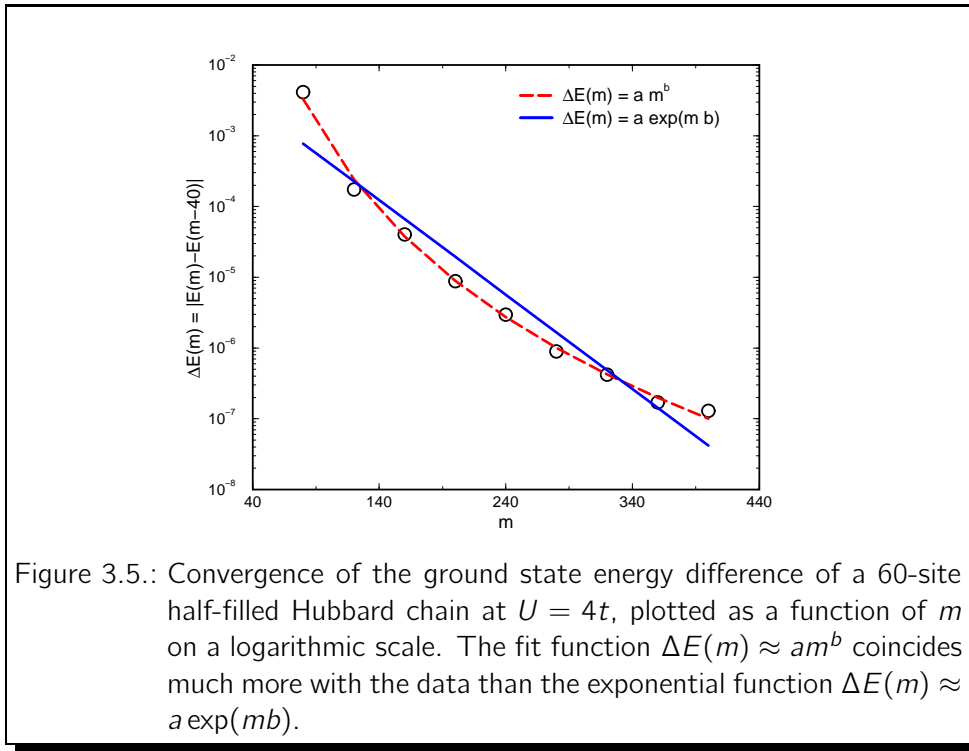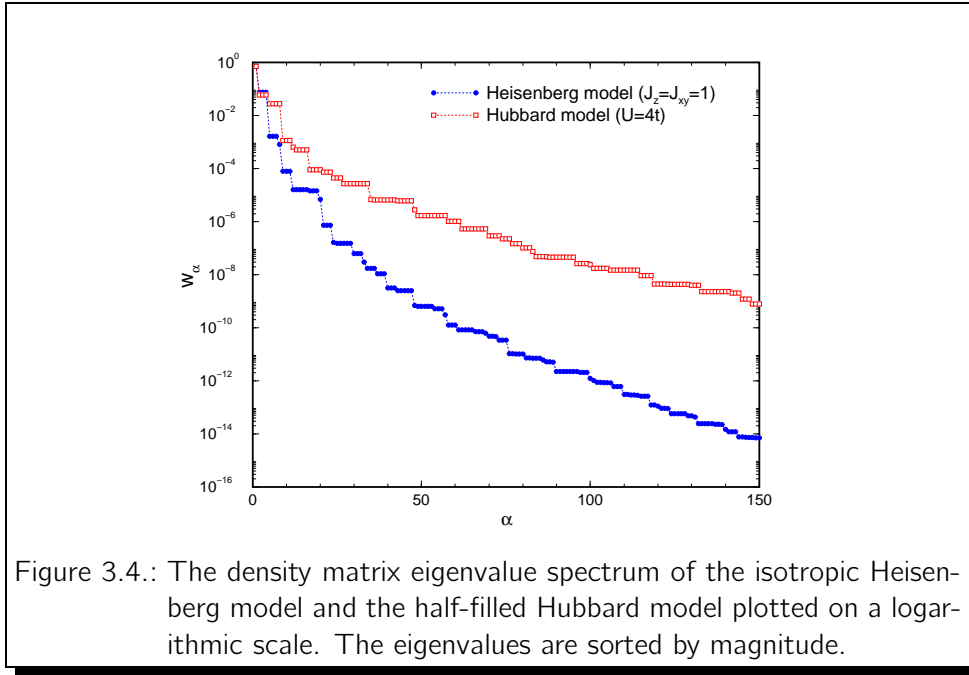
3.2.3. Truncation error & eigenvalue convergence

The DMRG precision depends crucially on the number of states that have been projected out in order to truncate the Hilbert space. This truncation error is measured by the so-called *discarded weight*

$$P_m \equiv 1 - \sum_{\alpha=1}^{m} w_\alpha\,, \qquad (3.25)$$

where w_α are the m largest density matrix eigenvalues. Note that the accuracy for a fixed m is many orders of magnitude worse for periodic than for open boundary conditions. In general, the quality of the truncation of $\mathfrak{H}_{\text{sys}}$ will be displayed by the distribution of the density matrix spectrum, where the eigenvalues are sorted by magnitude, i.e. $w_m \leq \ldots \leq w_1$. Fig. 3.4 depicts the distribution behaviour on the basis of the spin-1/2 Heisenberg model and the half-filled Hubbard chain, calculated with open boundary conditions. In the case of the Hubbard chain, the clearly slower decay indicates that one has to take twice as many (or even more) of DM eigenstates in order to achieve the same accuracy. Spectra of such a form have been observed in various calculations and only for a few integrable models the spectra of the density matrix have been determined exactly [103].

One can easily prove that in the limit $m \to \infty$ the convergence of the ground state energy $E(m)$ has rather a sub-exponential behaviour [104]. Fig. 3.5 shows the energy difference $\Delta E(m) = |E(m) - E(m-40)|$ of a half-filled Hubbard chain as a function of equidistant $m = 80, 120, 160, \ldots, 400$, plotted on a logarithmic scale. A fit of the data indicates that the function $\Delta E(m) \approx am^b$ coincides much more with the data than the exponential function $\Delta E(m) \approx a\exp(mb)$.

Figure 3.4.: The density matrix eigenvalue spectrum of the isotropic Heisenberg model and the half-filled Hubbard model plotted on a logarithmic scale. The eigenvalues are sorted by magnitude.

Figure 3.5.: Convergence of the ground state energy difference of a 60-site half-filled Hubbard chain at $U = 4t$, plotted as a function of m on a logarithmic scale. The fit function $\Delta E(m) \approx am^b$ coincides much more with the data than the exponential function $\Delta E(m) \approx a\exp(mb)$.

3.2.4. DMRG algorithms

First of all, one has to decide how to construct a DMRG algorithm, i.e. how to build up the system block and finally the superblock. In order to keep the dimension of $\mathfrak{H}$ as small as possible, one usually enlarges the system block $\mathbf{B}_\ell^{\text{sys}}$

by one site at each step, similar to Wilson's numerical RG (cf. with Sec. 3.2.1). Depending on the choice of the environment block $\mathbf{B}_\ell^{\text{env}}$ the procedure can be descibed by either the *infinite system* or *finite system* algorithm.

Infinite system algorithm

The infinite system algorithm is best suited for computing the ground state of a quantum chain in the thermodynamic limit $L \to \infty$. The standard algorithm is developed for open boundary conditions[3] and proceeds as follows (we use the illustrative representation by [82]):

❶ Take a system block of size ℓ and set up the matrices which represent the block Hamiltonian

$$\mathcal{H}_\ell^{\text{sys}} = \sum_{i=1}^{\ell-1} h_{i,i+1}, \quad \mathbf{B}_\ell^{\text{sys}} = \boxed{\overset{1}{\text{O}}\!-\!\text{O}\cdots\!-\!\cdots\overset{\ell}{\text{O}}}. \tag{3.26}$$

The local operator $h_{i,i+1} \equiv \text{id}^{i-1} \otimes h \otimes \text{id}^{\ell-1-i}$ depends on the studied model (cf. with Sec. 3.2.5). Notice that other local operators $\mathcal{O}$ have to be constructed in a similar way.

❷ Enlarge the system block by one site and form the corresponding Hamiltonian

$$\mathcal{H}_{\ell+1}^{\text{sys}} = \mathcal{H}_\ell^{\text{sys}} \otimes \text{id} + h_{\ell,\ell+1}, \quad \mathbf{B}_{\ell+1}^{\text{sys}} = \boxed{\boxed{\text{O}\!-\!\text{O}\cdots\!-\!\cdots\text{O}}\!-\!\text{O}} \tag{3.27}$$

as well as other operators.

❸ Construct the superblock

where the environment block $\mathbf{B}_{\ell+1}^{\text{env}}$ is usually obtained by reflecting $\mathbf{B}_{\ell+1}^{\text{sys}}$. In order to get the ground state $|\psi\rangle$ (or, if required, the excited states) diagonalize the Hamiltonian

$$\mathcal{H}_L = \mathcal{H}_{\ell+1}^{\text{sys}} + h_{\ell+1,\ell+2} + \mathcal{H}_{\ell+1}^{\text{env}} \tag{3.28}$$

of size $L = 2\ell + 2$ numerically by using the Lanczos algorithm (cf. with Sec. 3.1.2) or the Davidson algorithm [105]. If the desired system size L is reached, calculate the expectation values $\langle\psi|\mathcal{O}|\psi\rangle$ and $\langle\psi|\mathcal{O}\,\mathcal{O}'|\psi\rangle$.

---

[3]In principle, the DMRG can work with open and closed (peridic, antiperiodic) boundary conditions. However, the use of open boundary conditions produces a truncation error typically several orders of magnitude smaller.

❹ Build the reduced density matrix ρ and compute its complete eigenspectrum $\{w_\alpha, |u_\alpha\rangle\}$. Write the orthonormal eigenstates corresponding to the m largest eigenvalues w_α into the projector matrix

$$\mathcal{P} = \begin{pmatrix} | & | & & | \\ |u_1\rangle & |u_2\rangle & \cdots & |u_m\rangle \\ | & | & & | \end{pmatrix} . \tag{3.29}$$

❺ Project all operators onto the reduced basis of $\mathbf{B}^{\text{sys}}_{\ell+1}$ using Eq. (3.29), i.e.

$$\tilde{\mathcal{H}}^{\text{sys}}_{\ell+1} = \mathcal{P}^\dagger \mathcal{H}^{\text{sys}}_{\ell+1} \mathcal{P} \quad \text{and} \quad \tilde{\mathcal{O}} = \mathcal{P}^\dagger \mathcal{O} \mathcal{P} . \tag{3.30}$$

❻ Rename the enlarged system block

and continue from step ❷ after substituting $\tilde{\mathcal{H}}^{\text{sys}}_{\ell+1} \longrightarrow \mathcal{H}^{\text{sys}}_\ell$ and all other operators.

The algorithm successively increases the chain length by two sites at each iteration step, whereas the dimension of the Hilbert space $\mathfrak{H}$ stays constant. It is clear that the algorithm is adopted from Wilson's numerical RG procedure. However, there are a few important differences. In the former case the new basis for the system block is determined by the density matrix diagonalization and in the latter case by diagonalizing the Hamiltonian matrix. Furthermore, it is possible to formulate the infinite system algorithm without any reflection symmetry. This is easily done in the context of the finite system algorithm.

Finite system algorithm

Apart from the truncation error there is an additional source of error within the DMRG procedure. During the growth phase (until a desired chain size L is reached) the system block is embedded into an *approximate* superblock and not into the, a priori unknown, exact environment. This 'environment error' is not simply additive but can be reduced by using the finite system algorithm (cf. with Fig. 3.6). One can think of a zipper running repeatedly from left to right and then right to left through a superblock of fixed size. To be more precise: start with the infinite system algorithm and enlarge the superblock until a desired length L is reached. At each iteration $\ell = 1, \ldots, L/2$ store the Hamiltonian matrices $\tilde{\mathcal{H}}^{\text{env}}_{\ell'}$ with $\ell' = \ell$ as well as all additional operators which are needed to connect the blocks at each iteration (cf. with Sec. 3.2.5). It is clear that in contrast to the previous algorithm, the size of the environment block $\mathbf{B}^{\text{env}}_\ell$ has to be adapted at each iteration step in order to keep the superblock size fixed, i.e. $L = \ell + \ell'$. The algorithm then proceeds as follows [92]:

❶ Enlarge the system block Hamiltonian by one site ($\ell \rightarrow \ell + 1$). Then construct a superblock Hamiltonian (3.28) with $\mathcal{H}^{\text{sys}}_{\ell+1}$, but $\mathcal{H}^{\text{env}}_{\ell'=L-\ell}$ and diagonalize $\mathcal{H}_L$ numerically.

Figure 3.6.: Schematic diagram of the finite system algorithm for an eight-site quantum chain including two sweeps.
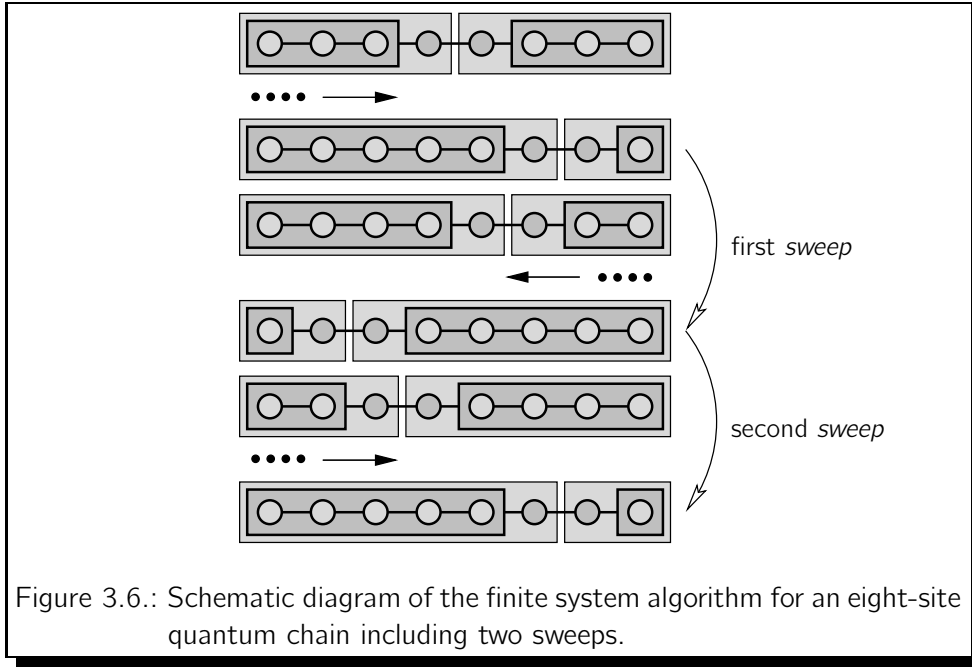
❷ Carry out steps ❹ and ❺ of the infinite system algorithm. Then store $\tilde{\mathcal{H}}^{\text{sys}}_{\ell+1}$ and all bond operators h which are needed to connect the blocks at each step. At last substitute $\tilde{\mathcal{H}}^{\text{sys}}_{\ell+1} \to \mathcal{H}^{\text{sys}}_{\ell}$ as well all the h operators.

❸ Repeat steps ❶ and ❷ until $\ell = L - 2$, i.e. $\ell' = 2$. This is the left–to–right phase of the algorithm.

❹ Now reverse the roles of $\mathcal{H}^{\text{sys}}$ and $\mathcal{H}^{\text{env}}$, i.e. switch directions to build up the environment block until $\ell' = L - 2$. This is the right–to–left phase of the algorithm.

❺ Repeat the whole algorithm, starting with step ❶.

Each time the direction is changed, so-called *sweep*, an improved set of stored block Hamiltonians is used to describe the environment block. It can be repeated until sufficient convergence is reached.

To demonstrate how the algorithm works in detail, we computed the ground state energy for a partially filled 60-site Hubbard system with open boundary conditions. Afterwards, we compared the data with the Bethe ansatz energy (see for details Sec. 2.3.2) versus the number of sweeps. Fig. 3.7 displays how the progression of the absolute error ΔE depends on the number of sweeps. The absolute error decreases with increasing number of iterations until convergence is reached. Notice that we used a modified version of the finite system algorithm by running from left to right through the superblock only.

3.2.5. Algorithm improvements

The most time-consuming part within the DMRG algorithm is the diagonalization of the superblock Hamiltonian (3.28). The efficiency can be increased by using
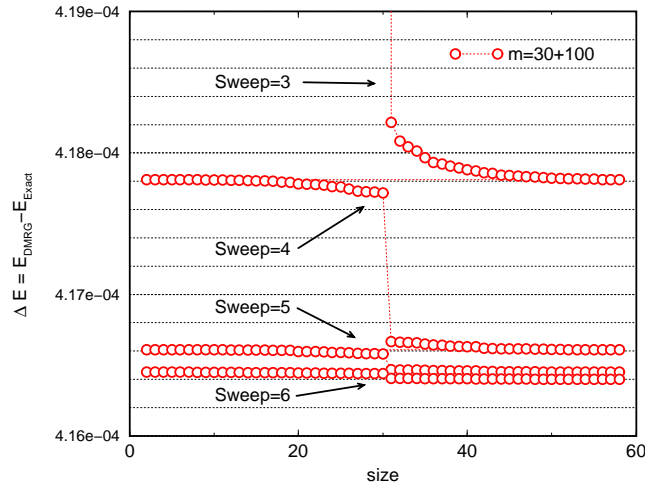
Figure 3.7.: The absolute error of the ground state energy computed by finite system algorithm and Bethe ansatz for a 60-site Hubbard chain with 40 electrons at $U = 4t$, plotted as a function of the size of the system block.

good quantum numbers and diagonalization accelerators reducing CPU time as well as CPU memory.

If good quantum numbers are used, the Hilbert space $\mathfrak{H}$ splits into invariant subspaces and the corresponding Hamiltonian matrix gains a block diagonal structure. Each block matrix can be stored separately, consequently less memory will be needed. But, what are good quantum numbers? The simplest symmetry, for instance, is associated with the conservation of the total number of electrons N. Additionally, each subspace $\mathfrak{H}_N$ can be grouped by implementing further quantum numbers like S^z.

Construction of the superblock Hamiltonian

Up to now, we did not give any description of how to construct and store the Hamiltonian matrix of an interacting quantum system

$$\mathcal{H}_{B_1 B_2} = \mathcal{H}_{B_1} + h_{B_1 B_2} + \mathcal{H}_{B_2} \equiv \mathcal{H}_L \tag{3.31}$$

which is built up from block $\mathbf{B}_1$ with m_1 states and $\mathbf{B}_2$ with m_2 states. In this section we will show how to do this efficiently.

In order to form the Hamiltonian matrix for two blocks joined together, it is necessary that each block has various bond operators which are stored as matrices. For instance, in the case of the Hubbard model, one has to store the matrix representations of $c_{n,\sigma}^\dagger$, where n corresponds to either the leftmost (l) or the rightmost (r) site of the block. Note that operators $c_{n,\sigma}$ can be easily obtained by taking the Hermitian conjugate of $c_{n,\sigma}^\dagger$. Consequently, they are not stored within the routine. Following [92], the matrix which is representing the Hamiltonian

$\mathcal{H}_{B_1 B_2}$ is then given by

$$
\begin{aligned}
\left[\mathcal{H}_{B_1 B_2}\right]_{ij,i'j'} &= \left[\mathcal{H}_{B_1}\right]_{ii'}\delta_{j,j'} + \sum_\sigma \left(\left[c^\dagger_{r,\sigma}\right]_{ii'}\left[c_{l,\sigma}\right]_{jj'} + \left[c^\dagger_{l,\sigma}\right]_{jj'}\left[c_{r,\sigma}\right]_{ii'} \right) \\
&\quad + \left[\mathcal{H}_{B_2}\right]_{jj'}\delta_{i,i'} ,
\end{aligned}
\tag{3.32}
$$

where the $m_1 m_2$ states are labeled by the indices ij.

However, the Hamiltonian matrix should not be explicitly constructed and thereby allocated in memory, because Lanczos or Davidson procedure use only the matrix-vector multiplication at each diagonalization step (cf. with Sec. 3.1.3). Instead, one should rather form and store the action $\mathcal{H}|\psi\rangle$ which uses less memory and is also faster. Starting with the more general expression

$$
\left[\mathcal{H}_L\right]_{ij,i'j'} = \sum_\alpha \left[A^\alpha\right]_{ii'}\left[B^\alpha\right]_{jj'}
\tag{3.33}
$$

the matrix-vector product then reads

$$
\sum_{i',j'} \left[\mathcal{H}_L\right]_{ij,i'j'} \left[\psi^\alpha\right]_{i'j'} = \sum_\alpha \sum_{i'} \left[A^\alpha\right]_{ii'} \left(\sum_{j'} \left[B^\alpha\right]_{jj'} \left[\psi\right]_{i'j'} \right) .
\tag{3.34}
$$

For each α, the last sum is used first to compute a temporary matrix $\left[C^\alpha\right]$. Afterwards, the multiplication of $\left[A^\alpha\right]$ with $\left[C^\alpha\right]^t$ provides a partial result, which is added into the result vector, giving a sum on α. Note that such a calculation can be accelerated if quantum numbers are used.

Transformation of the wavefunction

Lanczos or Davidson diagonalization algorithms can usually be speeded up if the initial vector already has characteristic features of the ground state vector. In the case of the DMRG algorithm, such initial guesses can be provided for either the infinite system algorithm [106, 107] or the finite system algorithm [108]. Because the first statement is restricted to spin models only, we will focus on the second idea which transforms the wavefunction of the previous DMRG step into the basis of the current configuration.

Assuming that the algorithm is in the left–to–right phase in which one site is iteratively added to the left block[4], the transformation proceeds as follows [108]: Let $|b_\ell\rangle$ be the m states of the left block $\mathbf{B}_\ell$ with ℓ denoting the rightmost site of the block. In addition, let $|s_{+1}\rangle$ be the m_S states of a single site block $\mathbf{S}$, where the subscript $+1$ labels the $\ell + 1$-site of a chain. Joining $\mathbf{B}_\ell$ and $\mathbf{S}$ together,
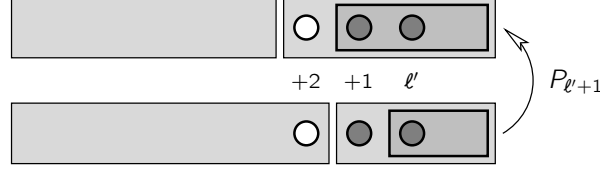

---
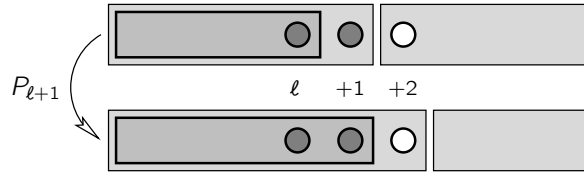
4 Note that an analogous transformation is used for the right–to–left phase.

the corresponding $m \times m_S$ basis states are represented by $|b_\ell\rangle \otimes |s_{+1}\rangle$. The new truncated basis with m states $|b_{\ell+1}\rangle$ is then generated by

$$|b_{\ell+1}\rangle = \sum_{s_{+1},b_\ell} \left[P_{\ell+1}\right]_{b_{\ell+1},b_\ell s_{+1}} |b_\ell\rangle \otimes |s_{+1}\rangle, \tag{3.35}$$

where P is a slightly rewritten form of the projection matrix (3.29). Note that $b_\ell s_{+1}$ is a single matrix index. The m states $|b_{\ell'+1}\rangle$ of the right block $\mathbf{B}_{\ell'+1}$,

where ℓ' labels the leftmost site of $\mathbf{B}_{\ell'}$, were constructed at an earlier DMRG step, but in a similar fashion

$$|b_{\ell'+1}\rangle = \sum_{s_{+1},b_{\ell'}} \left[P_{\ell'+1}\right]_{b_{\ell'+1},s_{+1}b_{\ell'}} |s_{+1}\rangle \otimes |b_{\ell'}\rangle. \tag{3.36}$$

Now we are going to describe how to transform the superblock wavefunction

$$|\psi\rangle = \sum_{b_\ell,s_{+1},s_{+2},b_{\ell'+1}} \psi(b_\ell s_{+1} s_{+2} b_{\ell'+1}) |b_\ell\rangle \otimes |s_{+1}\rangle \otimes |s_{+2}\rangle \otimes |b_{\ell'+1}\rangle \tag{3.37}$$

into the new basis $|b_{\ell+1}\rangle \otimes |s_{+2}\rangle \otimes |s_{+1}\rangle \otimes |b_{\ell'}\rangle$ which belongs to the next DMRG iteration. Note that the transformation is not exact, due to the truncation going from $|b_\ell\rangle \otimes |s_{+1}\rangle$ to $|b_{\ell+1}\rangle$. However, with the approximation

$$\sum_{b_{\ell+1}} |b_{\ell+1}\rangle\langle b_{\ell+1}| \approx 1 \tag{3.38}$$

as well as the use of formula (3.35) and (3.36) one finally obtains

$$\psi(b_{\ell+1}s_{+2}s_{+1}b_{\ell'}) \approx \sum_{b_\ell,s_{+1},b_{\ell'+1}} \left[P_{\ell+1}\right]_{\ldots} \psi(b_\ell s_{+1} s_{+2} b_{\ell'+1}) \left[P_{\ell'+1}\right]_{\ldots}. \tag{3.39}$$

The numerical realization of the transformation is most efficient if the process is divided into two parts. At first, it is useful to construct a temporary wavefunction

$$\psi(b_{\ell+1}s_{+2}b_{\ell'+1}) = \sum_{b_\ell,s_{+1}} \left[P_{\ell+1}\right]_{b_{\ell+1},b_\ell s_{+1}} \psi(b_\ell s_{+1} s_{+2} b_{\ell'+1}), \tag{3.40}$$

and then form the final result

$$\psi(b_{\ell+1}s_{+2}s_{+1}b_{\ell'}) = \sum_{b_{\ell'+1}} \psi(b_{\ell+1}s_{+2}b_{\ell'+1}) \left[P_{\ell'}\right]_{s_{+1}b_{\ell'},b_{\ell'+1}}. \tag{3.41}$$

In this form, the transformation requires only a small CPU time compared to other parts of the DMRG procedure. Using formula (3.40) and (3.41) reduces the number of diagonalization steps drastically, i.e. from about 100 to less than 30 steps.

3.2.6. Correlation functions

The ground state wavefunction $|\psi\rangle$ resulting from the diagonalization of the superblock Hamiltonian $\mathcal{H}_L$, is used to evaluate local expectation values $\langle\psi|\mathcal{O}(n)|\psi\rangle$ and correlation functions. Here, we will restrict ourselves to two-point correlators of the form $\langle\psi|\mathcal{O}(n)\mathcal{O}'(m)|\psi\rangle$. In order to measure $\mathcal{O}(n)$, one has to use the matrix representation, if necessary for each lattice site n. At every step of each iteration these operators have to be updated using Eq. (3.30). For instance, one obtains for the local spin-density $S^z(n)$ the expectation value

$$\langle\psi|S^z(n)|\psi\rangle = \sum_{i,i',j}\psi_{ij}\left[S^z(n)\right]_{ii'}\psi_{i'j}. \tag{3.42}$$

Note that the procedure gives exact results within the framework of the approximate eigenstate $|\psi\rangle$.

The examination of a correlation function depends on whether n and m are in the same block or not. If they are in different blocks, one has to keep track of $\left[\mathcal{O}(n)\right]_{ii'}$ and $\left[\mathcal{O}'(m)\right]_{jj'}$. The evaluation then reads

$$\langle\psi|\mathcal{O}(n)\mathcal{O}'(m)|\psi\rangle = \sum_{i,i',j,j'}\psi_{ij}\left[\mathcal{O}(n)\right]_{ii'}\left[\mathcal{O}'(m)\right]_{jj'}\psi_{i'j'}. \tag{3.43}$$

If n and m are in the same block, one has to keep track of $\left[\mathcal{O}(n)\mathcal{O}'(m)\right]_{ii'}$, because Eq. (3.43) would not give the correct evaluation of the correlation function. One gets

$$\langle\psi|\mathcal{O}(n)\mathcal{O}'(m)|\psi\rangle = \sum_{i,i',j}\psi_{ij}\left[\mathcal{O}(n)\mathcal{O}'(m)\right]_{ii'}\psi_{i'j}. \tag{3.44}$$

However, it is more convenient to select sites n and m on different blocks in order to avoid such complicated matrices.

The effect of open boundaries can be easily demonstrated by analyzing the local bond strength of the nearest-neighbour spin correlation function. In Fig. 3.8 we present (for the system block only) the local bond strength for 60 site Hubbard chain at half-filling. One observes a strong alternation in the bond strength induced by the open boundaries. The local bond strength is strongest at the end of the chain and becomes weaker in the center of the system, since the end pair only has one partner while the bulk pairs have two. In order to reduce such a boundary effect it is necessary to average the correlation function $C(|n-m|) = \langle\psi|\mathcal{O}(n)\mathcal{O}'(m)|\psi\rangle$ over a number of pairs of lattice sites separated by the same displacement $r \equiv |n-m|$ [109]:

$$\bar{C}(r) = \frac{1}{N(r)}\sum_{k=1}^{N(r)}C_k(r). \tag{3.45}$$

Typically one has to take around $N(r) = 9$ number of pairs and put for each r the pairs as close to the center of the chain as possible. For this purpose, it is necessary to store $\mathcal{O}(n)$ for each lattice site. Thus much more memory is required, which strongly depends on the system size L and the number of states m. This

Figure 3.8.: Nearest-neighbour spin correlation function for a 60 site Hubbard chain at half-filling, plotted as a function of site index n.
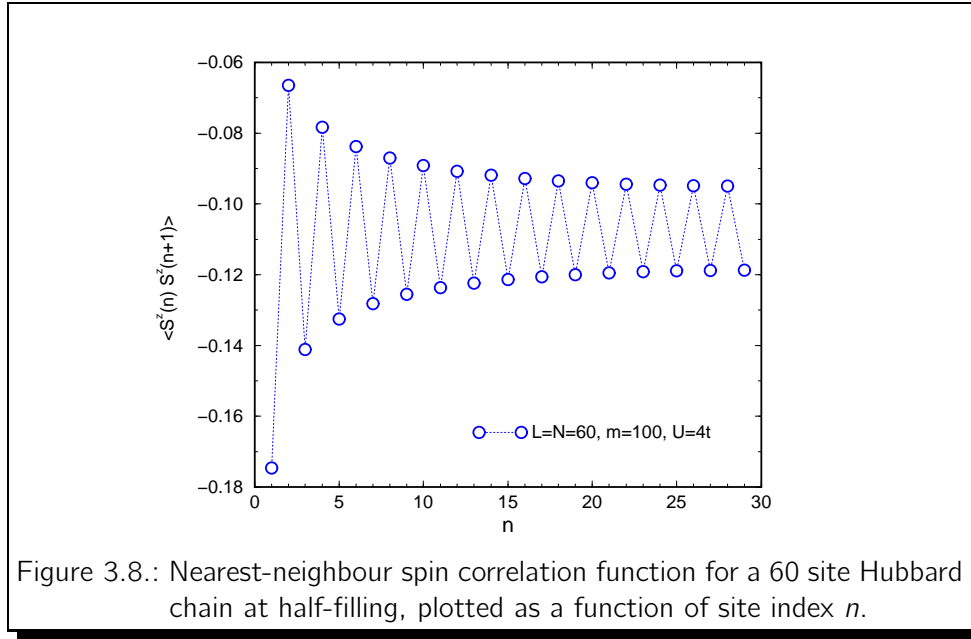
procedure becomes more complex if fermionic operators are involved. In order to evaluate the triplet-pair correlation function

$$C_{\mathsf{TS}}(r) = \langle \psi | \mathcal{O}_{\mathsf{TS}}^{\dagger}(r) \mathcal{O}_{\mathsf{TS}}(0) | \psi \rangle \tag{3.46}$$

with the order parameter

$$\mathcal{O}_{\mathsf{TS}}^{\dagger}(r) = \frac{1}{\sqrt{2}} \left(c_{r,\uparrow}^{\dagger} c_{r+1,\downarrow}^{\dagger} + c_{r,\downarrow}^{\dagger} c_{r+1,\uparrow}^{\dagger} \right) \tag{3.47}$$

it is essential to construct new operators (matrices) of the type

$$d_{r,\sigma\sigma'}^{\dagger} \equiv c_{r,\sigma}^{\dagger} c_{r+1,\sigma'}^{\dagger} \tag{3.48}$$

and then compute the corresponding correlation function. Note that a usual formulation does not provide the correct correlation. In addition, one must take into account that fermions obey anticommutation rules (cf. with Appendix A).

3.2.7. DMRG and the matrix product ansatz (MPA)

The nature of the DMRG as a variational method was studied by Östlund and Rommer. They proved that in the case of a spin-1 chain the DMRG ground state leads under some conditions to a special wavefunction form which is of matrix product type [110]. The authors have shown that one could get very good ground state energy by using the matrix product ansatz (MPA) [111] which corresponds to a small number m of states applied for the renormalization step within the DMRG procedure.

The relation between the DMRG method and the MPA can be understood in the following way [110]: the DMRG scheme proceeds by iteratively adding a single site.

The new set of basis states is then renormalized in order to keep the dimension of the Hilbert space $\mathfrak{H}$ at a manageable size. If $|\alpha\rangle_{\ell-1}$, $|s_\ell\rangle$ and $|\beta\rangle_\ell$ denote the basis of $\mathfrak{H}$ associated to a block $\mathbf{B}_{\ell-1}$ of size $\ell - 1$, a single site block $\mathbf{S}$ and a truncated block $\mathbf{B}'_\ell$, then the relation between these bases is written as follows

$$|\beta\rangle_\ell = \sum_{\alpha,s} \left[\mathcal{P}_\ell\right]_{\beta,\alpha s} |\alpha\rangle_{\ell-1} \otimes |s_\ell\rangle , \qquad (3.49)$$

where the subsript ℓ is associated to the chain position if it is inside of $|\ldots\rangle$, else it will denote the size of the block. The prefactor $\mathcal{P}$ corresponds to the projection matrix (3.29). Note that the expression (3.49) is only a modification of Eq. (3.35).

Changing the notation $\left[\mathcal{P}_\ell\right]_{\beta,\alpha s} \rightarrow \left[\mathcal{P}_\ell(s)\right]_{\beta\alpha}$, one can write the previous matrix of dimension $m \times (m \times d_S)$ as a set of d_S matrices with dimension $m \times m$. Further on, assuming that the procedure leads to a fixed point for $\mathcal{P}$, one can express the projection operator $\mathcal{P}_\ell(s)$ through $\mathcal{P}(s)$.

Iterative application of the renormalization Eq. (3.49) leads then to the following expression

$$|\beta\rangle_\ell = \sum_{s_\ell,\ldots,s_1,\alpha} \left(\left[\mathcal{P}(s_\ell)\right] \left[\mathcal{P}(s_{\ell-1})\right] \ldots \left[\mathcal{P}(s_1)\right] \right)_{\beta\alpha} |\alpha\rangle_0 \otimes |s_1\rangle \ldots |s_\ell\rangle , \qquad (3.50)$$

where $|\alpha\rangle_0$ denotes an initial state. Note that this is already the matrix product form of the wavefunction. However, it becomes more transparent, if one rewrites Eq. (3.50) as a linear combination of boundary conditions defined by $|\beta\rangle_\ell$ on the left and $|\alpha\rangle_0$ on the right, i.e.

$$|Q\rangle_\ell \equiv \sum_{\{s\}} \text{tr} \left(Q \left[\mathcal{P}(s_\ell)\right] \left[\mathcal{P}(s_{\ell-1})\right] \ldots \left[\mathcal{P}(s_1)\right] \right)_{\beta\alpha} |s_1\rangle \ldots |s_\ell\rangle . \qquad (3.51)$$

The special case of $Q = \text{id}$ describes a closed chain with periodic boundary conditions and has the form which was first introduced in [111]. Further information on the MPA and its generalization to two dimensional quantum systems, the so-called *vertex-state* representation, can be found in [112, 113] and references therein. A DMRG study of excitations of spin-1 chains with matrix product ground state can be found in [114].

3.2.8. Extensions of the DMRG technique

Since the introduction of the DMRG procedure in 1992, a large number of investigations using this numerical technique was published and in addition, a lot of improvements to this method as well as other applications based on the DMRG algorithm have been performed. Among other things there are following fields of activity:

❑ The application of the DMRG method to boson systems is difficult because of the large number of states per lattice site. In principle, this number is infinite and therefore one has to truncate this space.

An useful approach was suggested by Jeckelmann and White[115]. They developed a method which exactly transforms a boson site with 2^L levels to L pseudosites, each with two states. The mapping

$$\alpha = \sum_{\ell=1}^{L} 2^{\ell-1} r_\ell \quad \text{with } r_\ell \in \{0, 1\}, \tag{3.52}$$

between a boson level $|\alpha\rangle$ and the L-pseudosite state $|r_1, \ldots, r_L\rangle$ is based on the representation of a number in binary form. The authors implemented the pseudosite as hard-core bosons, in order to avoid fermion anticommutation minus signs. Further on, one has to express all boson operators b in terms of pseudosite operators a in which the boson number operator takes the form

$$N_b = b^\dagger b = \sum_{\ell=1}^{L} 2^{\ell-1} a_\ell^\dagger a_\ell . \tag{3.53}$$

Other boson operators take a more complicated form in the new representation. However, they can easily be determined from Eq. (3.52) and the properties of boson and hard-core boson operators.

❑ Beside the possibility of calculating static properties of ground states and low-lying eigenstates in quantum systems, assumptions for the determination of dynamical properties within the DMRG routine are possible too. However, the calculation of dynamical quantities has proved to be more difficult.

Several approaches have been proposed [116, 117, 118]. One of them calculates dynamical correlation functions by the use of a continued fraction expansion of the Green's function [116], related to the Lanczos algorithm which is implemented in most DMRG routines. More precisely, in order to evaluate the dynamical correlation function $C(t-t') = \langle\psi_0|\mathcal{O}^\dagger(t)\mathcal{O}(t')|\psi_0\rangle$ at zero temperature ($T = 0$) it useful to consider the Fourier transformed version of it, i.e.

$$C(\omega) = \sum_{n} |\langle\psi_n|\mathcal{O}|\psi_0\rangle|^2 \, \delta\big(\omega - (E_n - E_0)\big) , \tag{3.54}$$

where the summation is taken over all the eigenstates $|\psi_n\rangle$ of the Hamiltonian $\mathcal{H}$ with energy E_n. The quantity E_0 denotes the ground state energy. Using the Green's function formalism one can express Eq. (3.54) as
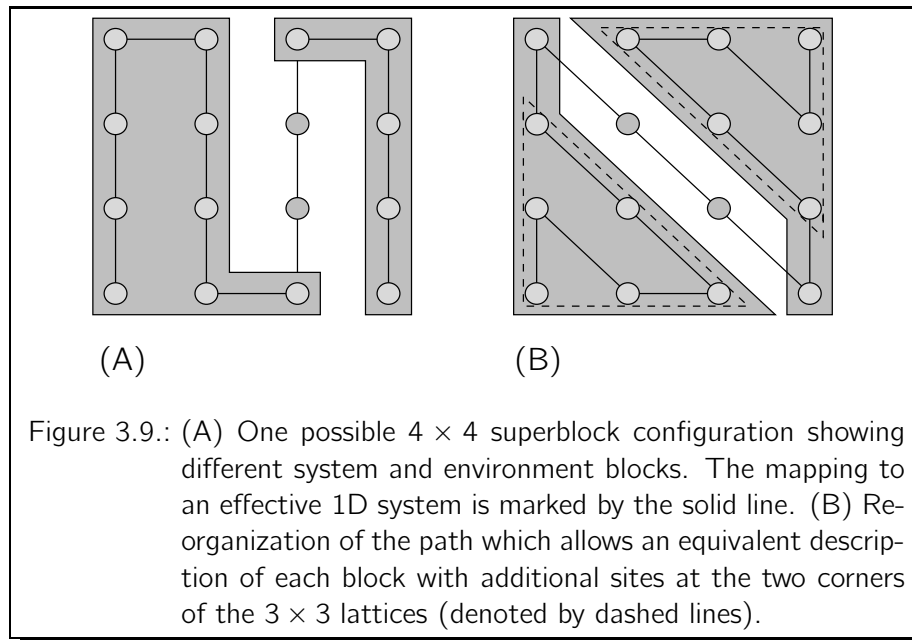
$$C(\omega) = -\frac{1}{\pi} \lim_{\eta \to 0^+} \text{Im} \, G(\omega + i\eta + E_0) , \tag{3.55}$$

where the Green's function G can be written in the form of a continued fraction

$$G = \cfrac{\langle\psi_0|\mathcal{O}^\dagger\mathcal{O}|\psi_0\rangle}{z - \alpha_0 - \cfrac{\beta_1^2}{z - \alpha_1 - \cfrac{\beta_2^2}{z - \cdots}}} . \tag{3.56}$$

The coefficients α_n and β_n can be obtained by the recursion formula (3.5) used in the Lanczos algorithm. In practice, this method works well for simple discrete spectra but it usually fails for more complicated spectra.

❏ Miscellaneous extensions of the DMRG algorithm to higher, in particular two dimensional quantum systems have been performed [108, 119, 120, 121, 122]. The simplest 2D algorithm is the so-called *multi-chain* approach in which the width of the lattice system is fixed and the height is expanded by adding whole rows or partial rows of sites. The implementation is similar to the traditional 1D algorithm by mapping the higher dimensional problem onto an effective 1D problem, simply by tracing a path through the lattice [108]. Apart from the approach used in [120], there is another true[5] 2D algorithm which was developed by Xiang et al. [121], where the initial blocks of a $L \times L$ lattice are built up directly from the previous configuration of $(L-1) \times (L-1)$ lattice sites (see Fig. 3.9). This approach has proved to be

(A) (B)

Figure 3.9.: (A) One possible 4×4 superblock configuration showing different system and environment blocks. The mapping to an effective 1D system is marked by the solid line. (B) Reorganization of the path which allows an equivalent description of each block with additional sites at the two corners of the 3×3 lattices (denoted by dashed lines).

very efficient and excellent results for the ground state energy of the spin-1/2 Heisenberg model on a square and triangular lattices were obtained, but application to fermion models is difficult and is still a subject of development.

❏ The formulation of a DMRG procedure for quantum lattice systems in momentum space was established due to the potential advantages over the real-space approach. The momentum is a good quantum number, since the basis in momentum space is translationally invariant. The use of this quantum number reduces the dimension of the Hilbert space. Moreover, momentum distribution or the dispersion of excitations can be directly calculated.

---

[5]The topological characteristics of a two-dimensional lattice are preserved within the algorithm.

The investigation of the Hubbard model using the momentum space formulation of the DMRG algorithm has shown that this tool is useful for the Hubbard model only at weak to intermediate coupling [123].

❑ The DMRG method has been successfully adapted for the study of two-dimensional classical systems [124] and for the investigation of thermodynamic properties of an 1D quantum system [125], in which the DMRG algorithm is applied onto the quantum transfer matrix and therefore is called (quantum) transfer-matrix DMRG or simply TMRG. An explicit description of the TMRG algorithm as well as its modifications can be found in [82, 94].

Of course, thermodynamic quantities of low-dimensional quantum models can be studied by the pure DMRG routine too. Already White showed formally that the method can be generalized to systems at finite temperature [91, 92]. It is necessary to target several excited states when building the reduced density matrix.

4. The Hubbard model with transverse spin exchange

4.1. Introduction

The discovery of high-temperature superconductivity in cuprates [25] has revived great activity on the research of superconductivity. While searching for new compounds having the same layered perovskite structure as La_2CuO_4, superconductivity in Sr_2RuO_4 with rather unconventional (non-s-wave) pairing[1] was found. Later on, one has proved the triplet nature of this superconducting state with a proximity to a ferromagnetic instability (see [126] for a review). Moreover, compounds like UGe_2 [127] or $ZrZn_2$ [128] even show coexistence of the TS phase with ferromagnetism.

Another group of unconventional superconductors with proximity of magnetic and superconducting ordering belongs to the family of quasi-one-dimensional organic conductors (cf. with Sec. 1.5). In the last few years a lot of measurements have provided evidence that the Bechgaard salts $(TMTSF)_2ClO_4$ and $(TMTSF)_2PF_6$ are triplet superconductors under pressure (see e.g. [129] and references therein). Motivated by these experimental results various models of strongly correlated electron systems showing proximity of (ferro) magnetic and (triplet) superconducting phases have been studied as attempt to construct a theoretical model for new superconducting materials. Usually the models are based on some extended versions of the Hubbard model. In particular, several extended versions of the *repulsive* Hubbard model have been employed as standard models for metal–insulator transitions, antiferromagnetism and high-T_c superconductivity (see [130] for a review). Based on experimental results showing strong easy-plane anisotropy of ferromagnetic spin fluctuations in the triplet superconductor Sr_2RuO_4 [131], we will focus our investigations on a rather simple extension of the Hubbard model including transverse (XY-type) spin exchange between electrons on nearest-neighbour sites, proposed by Japaridze and Müller-Hartmann [132]. They have shown that the 1D version of this model has an extremely rich *weak-coupling* phase diagram (see Fig. 4.1). In particular in the case of a half-filled band the ground state phase diagram is characterized by two insulating antiferromagnetic phases with easy-plane anisotropy and a spin gapful metallic phase with an identical decay of the

---

[1]Superconductivity involves the formation of a quantum condensate state by so-called *Cooper pairs*. Each Cooper pair can be in a state of either total spin $S = 0$ (singlet) or $S = 1$ (triplet). The antisymmetric singlet state is accompanied by a symmetric orbital function (*s*-wave, *d*-wave), whereas the symmetric triplet state is accompanied by an antisymmetric orbital function (*p*-wave, *f*-wave).
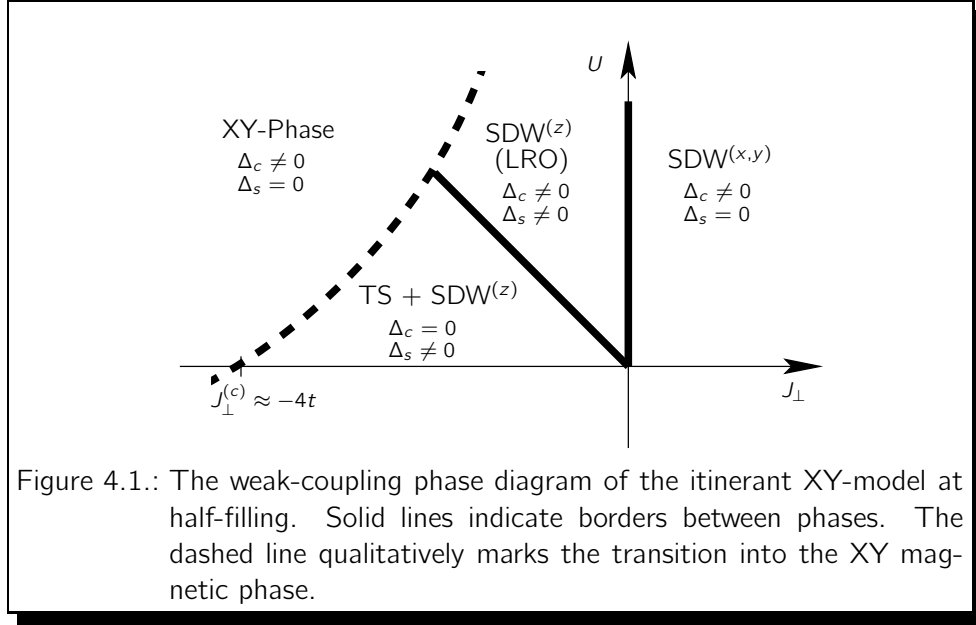
Figure 4.1.: The weak-coupling phase diagram of the itinerant XY-model at half-filling. Solid lines indicate borders between phases. The dashed line qualitatively marks the transition into the XY magnetic phase.

triplet superconducting and spin-density wave (SDW$^{(z)}$) instabilities. Further on, strong evidence for the presence of an additional transition into a *ferromagnetic* XY phase has been given [132].

Beside the hopping amplitude t and the (repulsive) Coulomb interaction U, the 1D Hamiltonian exhibits a transverse spin exchange term characterized by $J_\perp$. The Hamiltonian reads

$$
\mathcal{H}_{t-U-J_\perp} = \quad -t\sum_{\ell=1}^{L}\sum_{\alpha}\left(c^\dagger_{\ell\alpha}c_{\ell+1\alpha} + c^\dagger_{\ell+1\alpha}c_{\ell\alpha}\right) + U\sum_{\ell=1}^{L} n_{\ell\uparrow}n_{\ell\downarrow}
$$

$$
+\frac{J_\perp}{2}\sum_{\ell=1}^{L}(S^+_\ell S^-_{\ell+1} + S^+_{\ell+1}S^-_\ell). \tag{4.1}
$$

One can easily verify that besides the obvious $U(1)$ spin-symmetry in the half-filled case the model is characterized by the $SU(2)$ charge-symmetry.

4.1.1. Analogy to the pair-hopping model

The electron-hole transformation in one spin component

$$
c^\dagger_{\ell,\uparrow} \to c^\dagger_{\ell,\uparrow} \quad \text{and} \quad c^\dagger_{\ell,\downarrow} \to (-1)^\ell c_{\ell,\downarrow} \tag{4.2}
$$

interchanges the charge and spin degrees of freedom and maps (4.1) to the attractive Hubbard model with pair-hopping interaction $Y = J_\perp/2$. Without Coulomb interaction the new Hamiltonian has the following form:

$$
\mathcal{H}_{\text{t-Y}} = \quad - \quad t\sum_{\ell=1}^{L}\sum_{\alpha}\left(c^\dagger_{\ell,\alpha}c_{\ell+1,\alpha} + c^\dagger_{\ell+1,\alpha}c_{\ell,\alpha}\right)
$$

$$
- \quad Y\sum_{\ell=1}^{L}\left(c^\dagger_{\ell,\uparrow}c^\dagger_{\ell,\downarrow}\,c_{\ell+1,\downarrow}c_{\ell+1,\uparrow} + \text{h.c.}\right). \tag{4.3}
$$

The pair-hopping model (4.3) is to be considered as a phenomenological model to describe the dynamics of small size Cooper pairs. Since high-temperature super-conducting materials are known to indicate such pairs, to study this model can be important to capture some of the physics of high-temperature superconductors. Furthermore, the low-energy physics of this model is related in some way to the physics of the attractive Hubbard model, which has an exact solution via Bethe ansatz.

It is important to note that $Y \to -Y$ is not a symmetry of the model, unlike the Hubbard model. Hence, at large $|Y|/t$ the system is different for negative and positive Y [133].

Phase transition in pair-hopping model

Using exact diagonalization calculations for chains up to 10 sites Penson and Kolb [134] found a phase transition at which a spin gap opens for $Y > Y_c \approx 1.4\,t$. Very soon later, Affleck and Marston [133] analysed this model within the framework of the weak-coupling continuum limit approach. They could show that this model is essentially equivalent to the attractive Hubbard model. Accordingly, they predicted that the transition in the pair-hopping model must occur at $Y = 0$ just like in the Hubbard model. A few years later, Hui and Doniach [135] presented some new numerical calculations which show the existence of a phase transition at a finite positive value of Y. They also presented some arguments on why the predictions of the renormalization group analysis could be not valid. Finally, Sikkema and Affleck [136] have investigated the low-energy spectrum using the DMRG technique for open chains up to 60 sites. They concluded that there is no transition at a non-zero positive value of Y and that the standard low-energy picture predicted by Affleck and Marston is valid. In the opposite part of the phase diagram ($Y < 0$), they found a transition into a spin gapped phase at $Y < Y_c \approx -1.5\,t$.

4.2. Weak-coupling results for the half-filled band

4.2.1. Bosonized Hamiltonian

The mapping of the initial lattice Hamiltonian (4.1) into the continuum theory (cf. with Sec. 1.2.3 as well as [132]) of two independent quantum models

$$
\mathcal{H}_c = v_c \int dx \left(\frac{1}{2}[\partial_x \phi_c(x)]^2 + \frac{1}{2}[\partial_x \theta_c(x)]^2 \right.
$$
$$
\left. + \frac{m_c}{a_0^2} \cos\left[\sqrt{8\pi K_c}\,\phi_c(x)\right] \right) \quad \text{and} \tag{4.4}
$$
$$
\mathcal{H}_s = v_s \int dx \left(\frac{1}{2}[\partial_x \phi_s(x)]^2 + \frac{1}{2}[\partial_x \theta_s(x)]^2 \right.
$$
$$
\left. + \frac{m_s}{a_0^2} \cos\left[\sqrt{8\pi K_s}\,\phi_s(x)\right] \right), \tag{4.5}
$$

where we have defined ($\mu \in \{c, s\}$)

$$v_\mu = \frac{v_F}{K_\mu} \quad \text{with} \quad v_F = 2t \left(1 + \frac{J_\perp}{2\pi t} \right) \tag{4.6}$$

and

$$2 \left(K_c - 1 \right) \approx g_c = -\frac{1}{\pi v_F} \left(U + J_\perp \right), \tag{4.7}$$

$$2\pi m_c = g_u = -\frac{1}{\pi v_F} \left(U + J_\perp \right), \tag{4.8}$$

$$2 \left(K_s - 1 \right) \approx g_s = \frac{1}{\pi v_F} \left(U + J_\perp \right), \tag{4.9}$$

$$2\pi m_s = g_\perp = \frac{1}{\pi v_F} \left(U - J_\perp \right) \tag{4.10}$$

allows to study the ground state phase diagram of the system based on the infrared properties of these Hamiltonians.

Depending on the relation between the bare coupling constants g_μ, g_u and $g_\perp$ the system exhibits two different regimes:

❶ For $g_c \geq |g_u|$ ($g_s \geq |g_\perp|$) we are in the weak coupling regime. The effective mass M_μ scales to 0. The low energy (large distance) behaviour of the gapless charge (spin) degrees of freedom is described by a free scalar field. The corresponding correlations show a power law decay

$$\langle e^{i\sqrt{2\pi K}\phi(x)} e^{-i\sqrt{2\pi K}\phi(x')} \rangle \sim \left| x - x' \right|^{-K}, \tag{4.11}$$

$$\langle e^{i\sqrt{2\pi/K}\theta(x)} e^{-i\sqrt{2\pi/K}\theta(x')} \rangle \sim \left| x - x' \right|^{-1/K} \tag{4.12}$$

and the only parameter controlling the infrared behaviour in the gapless regime is the fixed-point value of the effective coupling constants K_μ.

❷ For $g_c < |g_u|$ ($g_s < |g_\perp|$) the system scales to the strong coupling regime; depending on the sign of the bare mass m_μ the effective mass M_μ scales to $\pm\infty$, which signals the crossover to the strong coupling regime and indicates the dynamical generation of a commensurability gap in the charge (spin) excitation spectrum. The fields ϕ_μ get ordered with vacuum expectation values [137, 138]

$$\langle \phi_\mu \rangle = \begin{cases} \sqrt{\pi/(8K_\mu)} & : \quad m_\mu > 0 \\ 0 & : \quad m_\mu < 0 \end{cases}. \tag{4.13}$$

Using the initial values of the coupling constants given in (4.7)-(4.10), we obtain that flow trajectories in the charge sector (due to the $SU(2)$-charge symmetry) are along the separatrix $g_c = g_u$. Therefore, at

$$U + J_\perp > 0 \tag{4.14}$$

there is a gap in the charge excitation spectrum ($\Delta_c \neq 0$) and the charge field ϕ_c is ordered with the vacuum expectation value

$$\langle \phi_c \rangle = 0 , \tag{4.15}$$

while at $U + J_\perp < 0$ the charge sector is gapless and the fixed-point value of the parameter $K_c^\star$ is one.

The $U(1)$ symmetry of the spin channel ensures more alternatives. Depending on the relation between the bare coupling constants there are two different strong-coupling sectors in the spin channel. For

$$U < \min\{0, J_\perp\} \tag{4.16}$$

the spin channel is massive ($\Delta_s \neq 0$) and the field ϕ_s gets ordered with the vacuum expectation value

$$\langle \phi_s \rangle = 0 , \tag{4.17}$$

while for

$$J_\perp < \min\{0, U\} \tag{4.18}$$

the spin channel is massive ($\Delta_s \neq 0$) too, but the field gets ordered with vacuum expectation value

$$\langle \phi_s \rangle = \sqrt{\frac{\pi}{8K_s}} . \tag{4.19}$$

In the present work we restrict our considerations to the case $U > 0$ and hence Eq. (4.18) simplifies to $J_\perp < 0$ while (4.16) has to be neglected.

In all other cases the excitation spectrum in the corresponding channel is gapless. The low-energy behaviour of the system is controlled by the fixed-point value of the Luttinger-liquid parameter $K_s^\star = 1 + \frac{1}{2}g_s^\star$. In the particular case of vanishing on-site interaction ($U = 0$) and antiferromagnetic exchange ($J_\perp > 0$) one has to use a second order RG analysis to define accurately the fixed point value of the parameter K_s (for details, see Ref. [132]).

4.2.2. Order parameters

The order parameters are used to clarify the ground state properties of the model in different sectors. At first we derive exemplarily the boson-field representation of the on-site singlet operator

$$\mathcal{O}_{\mathrm{OS}}(\ell) \quad = \quad c_{\ell,\uparrow} c_{\ell,\downarrow} . \tag{4.20}$$

We use the fermionic field representation, i.e. $c_{\ell,\sigma} \rightarrow \psi_\sigma(x)/\sqrt{a_0}\big|_{x=\ell a_0}$, and continue with

$$
\begin{aligned}
\mathcal{O}_{\mathrm{OS}}(x) \quad &\underset{(1.9)}{=} \quad \prod_\sigma \left(e^{ik_F x} \psi_{R,\sigma}(x) + e^{-ik_F x} \psi_{L,\sigma}(x) \right) \\
&= \quad \psi_{R,\uparrow}\psi_{L,\downarrow} + \psi_{L,\uparrow}\psi_{R,\downarrow} + e^{2ik_F}\psi_{R,\uparrow}\psi_{R,\downarrow} + e^{-2ik_F}\psi_{L,\uparrow}\psi_{L,\downarrow} \\
&\underset{(1.17)}{=} \quad \frac{1}{2\pi\alpha} \left(F_{R,\uparrow}F_{L,\downarrow}\, e^{i(\Phi_{R,\uparrow}+\Phi_{L,\downarrow})} + F_{L,\uparrow}F_{R,\downarrow}\, e^{i(\Phi_{R,\downarrow}+\Phi_{L,\uparrow})} \right. \\
&\qquad + F_{R,\uparrow}F_{R,\downarrow}\, e^{2ik_F}\, e^{i(\Phi_{R,\uparrow}+\Phi_{R,\downarrow})} \\
&\qquad \left. + F_{L,\uparrow}F_{L,\downarrow}\, e^{-2ik_F}\, e^{i(\Phi_{L,\uparrow}+\Phi_{L,\downarrow})} \right) ,
\end{aligned}
$$

Now we set $k_F = \pi/(2a_0)$ which is valid for a half-filled band. This leads to $\exp(i\pi x/a_0) = exp(i\pi\ell) = (-1)^\ell$ and in particular

$$
\mathcal{O}_{OS}(x) \underset{(1.19)}{=} \frac{1}{2\pi\alpha} \left(F_{R,\uparrow}F_{L,\downarrow}e^{i\sqrt{2\pi}(\theta_c - \phi_s)} + F_{L,\uparrow}F_{R,\downarrow}e^{i\sqrt{2\pi}(\theta_c + \phi_s)} \right.
$$
$$
+ (-1)^\ell F_{R,\uparrow}F_{R,\downarrow}e^{i\sqrt{2\pi}(\theta_c - \phi_c)}
$$
$$
\left. + (-1)^\ell F_{L,\uparrow}F_{L,\downarrow}e^{i\sqrt{2\pi}(\theta_c + \phi_c)} \right) .
$$

Using commutation relation (1.20) in combination with the Campbell-Baker-Hausdorff formula $\exp(A)\exp(B) = \exp(A + B)\exp([A, B]/2)$ gives

$$
\mathcal{O}_{OS}(x) = \frac{1}{2\pi\alpha} \left(F_{R,\uparrow}F_{L,\downarrow}e^{-i\sqrt{2\pi}\phi_s} + F_{L,\uparrow}F_{R,\downarrow}e^{i\sqrt{2\pi}\phi_s} \right.
$$
$$
- i(-1)^\ell F_{R,\uparrow}F_{R,\downarrow}e^{-i\sqrt{2\pi}\phi_c}
$$
$$
\left. + i(-1)^\ell F_{L,\uparrow}F_{L,\downarrow}e^{i\sqrt{2\pi}\phi_c} \right) e^{i\sqrt{2\pi}\theta_c}
$$
$$
\approx \frac{1}{\pi\alpha} \left(\cos\left[\sqrt{2\pi}\phi_s\right] - (-1)^\ell \sin\left[\sqrt{2\pi}\phi_c\right] \right) e^{i\sqrt{2\pi}\theta_c} .
$$

The last step was performed without the Klein factors $F_{\eta,\sigma}$. Note that the exponent of a correlation function will be unaffected as long as logarithmic corrections will not be involved [69]. Finally, transforming the phase fields as $\phi_\mu \to \sqrt{K_\mu}\phi_\mu$ and $\theta_\mu \to \theta_\mu/\sqrt{K_\mu}$ leads to the expression

$$
\mathcal{O}_{OS}(x) \approx \left(\cos\left[\sqrt{2\pi K_s}\phi_s(x)\right] - (-1)^\ell \sin\left[\sqrt{2\pi K_c}\phi_c(x)\right] \right) e^{i\sqrt{\frac{2\pi}{K_c}}\theta_c(x)} , \quad (4.21)
$$

where the factor $1/(\pi\alpha)$ has been omitted. Note that the remaining order parameters can be computed in an analogous manner. The other superconducting order parameters are

❑ the extended-singlet

$$
\mathcal{O}_{ES}(\ell) = \frac{1}{\sqrt{2}} \left(c_{\ell,\uparrow}c_{\ell+1,\downarrow} - c_{\ell,\downarrow}c_{\ell+1,\uparrow} \right) \tag{4.22}
$$
$$
\mathcal{O}_{ES}(x) \approx (-1)^\ell \cos\left[\sqrt{2\pi K_c}\phi_c(x)\right] e^{i\sqrt{\frac{2\pi}{K_c}}\theta_c(x)} \tag{4.23}
$$

❑ and the triplet pairing

$$
\mathcal{O}_{TS}(\ell) = \frac{1}{\sqrt{2}} \left(c_{\ell,\uparrow}c_{\ell+1,\downarrow} + c_{\ell,\downarrow}c_{\ell+1,\uparrow} \right) \tag{4.24}
$$
$$
\mathcal{O}_{TS}(x) \approx \sin\left[\sqrt{2\pi K_s}\phi_s(x)\right] e^{i\sqrt{\frac{2\pi}{K_c}}\theta_c(x)} . \tag{4.25}
$$

Additionally we will use

❑ the longitudinal on-site spin-density operator

$$S^z(\ell) \quad \propto \quad \sum_\sigma \sigma \, c^\dagger_{\ell,\sigma} c_{\ell,\sigma} \tag{4.26}$$

$$
\begin{aligned}
S^z(x) \quad \approx \quad & \sqrt{\frac{K_s}{2\pi}} \partial_x \phi_s(x) \\
& + (-1)^\ell \cos\left[\sqrt{2\pi K_c}\phi_c(r)\right] \sin\left[\sqrt{2\pi K_s}\phi_s(r)\right],
\end{aligned} \tag{4.27}
$$

❑ the transverse on-site spin-density operators

$$S^x(\ell) \quad \propto \quad \sum_\sigma c^\dagger_{\ell,\sigma} c_{\ell,-\sigma} \tag{4.28}$$

$$
\begin{aligned}
S^x(x) \quad \approx \quad & i\cos\left[\sqrt{2\pi K_s}\phi_s(x)\right] \sin\left[\sqrt{\frac{2\pi}{K_s}}\theta_s(x)\right] \\
& + i(-1)^\ell \cos\left[\sqrt{2\pi K_c}\phi_c(x)\right] \sin\left[\sqrt{\frac{2\pi}{K_s}}\theta_s(x)\right],
\end{aligned} \tag{4.29}
$$

$$S^y(\ell) \quad \propto \quad i\sum_\sigma \sigma \, c^\dagger_{\ell,\sigma} c_{\ell,-\sigma} \tag{4.30}$$

$$
\begin{aligned}
S^y(x) \quad \approx \quad & -i\cos\left[\sqrt{2\pi K_s}\phi_s(x)\right] \cos\left[\sqrt{\frac{2\pi}{K_s}}\theta_s(x)\right] \\
& - i(-1)^\ell \cos\left[\sqrt{2\pi K_c}\phi_c(x)\right] \sin\left[\sqrt{\frac{2\pi}{K_s}}\theta_s(x)\right]
\end{aligned} \tag{4.31}
$$

❑ and the on-site density operator

$$\rho(\ell) \quad = \quad \sum_\sigma \left(c^\dagger_{\ell,\sigma} c_{\ell,\sigma} - 1\right) \tag{4.32}$$

$$
\begin{aligned}
\rho(x) \quad \approx \quad & \sqrt{\frac{2K_c}{\pi}} \partial_x \phi_c(x) \\
& + (-1)^\ell \sin\left[\sqrt{2\pi K_c}\phi_c(x)\right] \cos\left[\sqrt{2\pi K_s}\phi_s(x)\right].
\end{aligned} \tag{4.33}
$$

4.2.3. The weak-coupling phase diagram

With the results of the previous section for the excitation spectrum and the behaviour of the corresponding fields Eqs. (4.11)–(4.13) we now analyze the *weak-coupling* ground state phase diagram (cf. with Fig. 4.1) of the model (4.1) .
Let us first consider the case $U = 0$, where the weak-coupling analysis shows the existence of two different phases: in the case of antiferromagnetic exchange, at $J_\perp > 0$, there is a gap in the charge excitation spectrum while the spin sector is gapless. Ordering of the field ϕ_c with vacuum expectation value $\langle\phi_c\rangle = 0$ leads to a suppression of the CDW and *superconducting* correlations. The SDW and *Peierls* correlations show a power-law decay at large distances (see [132] for details). Due to the $U(1)$-spin symmetry, $K_s^\star > 1$ and the transverse correlations dominate in the ground state

$$\langle S^+(x)S^-(0)\rangle \sim x^{-K_s^\star - 1/K_s^\star} + (-1)^\ell x^{-1/K_s^\star}, \tag{4.34}$$

while the longitudinal spin correlations

$$\langle S^z(x)S^z(0)\rangle \sim x^{-2} + (-1)^\ell x^{-K_s^\star} \tag{4.35}$$

and *Peierls* correlations decay faster.

We now focus on the case of ferromagnetic exchange between spins. At $U = 0$ and $J_\perp < 0$ there is a gap in the spin excitation spectrum while the charge excitation spectrum is gapless. As common in the half-filled band case, the gapless charge excitation spectrum opens a possibility for the realization of a superconducting instability in the system. Moreover, due to the $U(1)$-symmetry of the system, ordering of the ϕ_s with vacuum expectation value $\langle \phi_s \rangle = \sqrt{\pi/8K_s}$ leads to a suppression of the CDW and singlet correlations. In this case the SDW$^{(z)}$ and triplet correlations show an identical power-law decay

$$\langle S^z(x)S^z(0)\rangle = \langle \mathcal{O}_{\mathsf{TS}}(x)\mathcal{O}_{\mathsf{TS}}(0)\rangle \sim (-1)^\ell x^{-1} \tag{4.36}$$

at large distances and are the *dominating instabilities* in the system.

Let us now consider the effect of the on-site Coulomb repulsion. At $J_\perp > 0$ the easy-plane antiferromagnetic phase remains unchanged at $U > 0$. However, at $J_\perp < 0$ the TS+SDW$^{(z)}$ phase is stable only towards influence of a weak $U < -J_\perp$ on-site coupling. In the case of repulsive Hubbard interaction, at $U > -J_\perp$ a charge gap opens. This regime corresponds to the appearance of a long-range ordered *antiferromagnetic (Néel)* phase

$$\langle S^z(x)S^z(0)\rangle \sim (-1)^\ell \text{ constant} \tag{4.37}$$

in the ground state.

The ferromagnetic transition

Let us now discuss the ferromagnetic transition in the itinerant XY model ($U = 0$). The very presence of this transition can already been seen within the weak-coupling studies, however detailed analysis of the phase diagram close to transition is out of scope of the continuum-limit approach. As we obtained, at $J_\perp < 0$, $|J_\perp| \ll t$, the charge excitation spectrum is gapless and the spin excitation spectrum is massive. However, in the limit of strong ferromagnetic exchange $|J_\perp| \gg t$, the model is equivalent to the XY spin chain. Therefore, with increasing coupling one has to expect a transition from the regime with massive spin and massless charge excitation spectrum into a insulating magnetic phase with gapless spin excitations. On the other hand, in the case of antiferromagnetic exchange $J_\perp > 0$ the weak coupling study shows a phase with gapless spin, gapped charge and dominating easy-plane spin correlations. One expects that this phase evolves smoothly to the strong coupling limit.

The $J_\perp \leftrightarrow -J_\perp$ asymmetry is already seen on the level of the Hartree regularization of the band-width cut-off parameter $W = 2\pi t$ as given by the Eqs. (4.6)

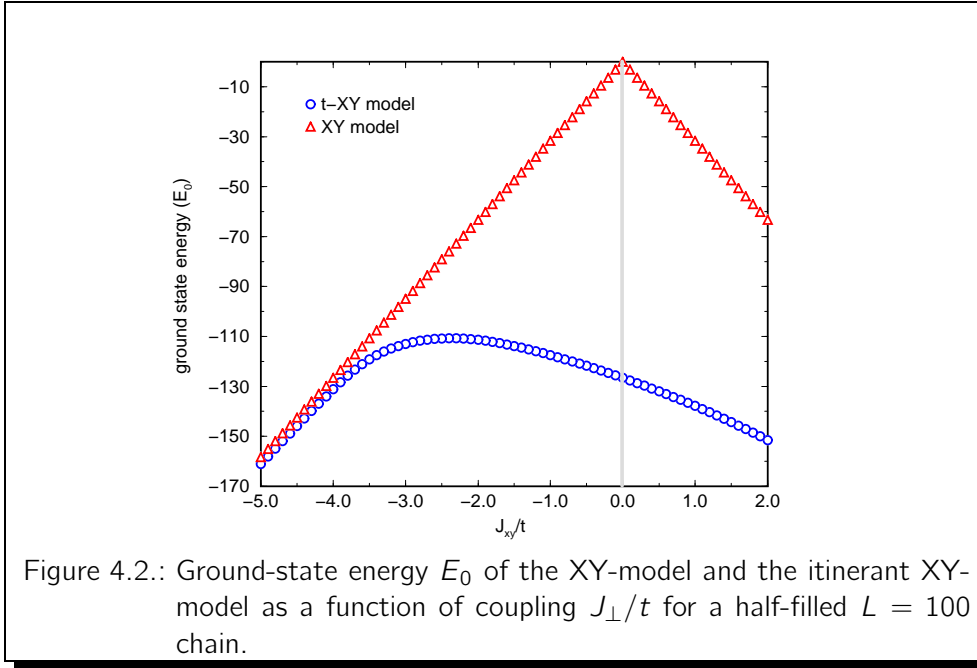$$W_{\text{eff}} = 2\pi \left(1 + \frac{J_\perp}{2\pi t}\right) . \tag{4.38}$$

The weak coupling approaches fail when the effective dimensionless coupling constant $|g_i| = J_\perp/(2\pi t) = |g_i^c| \simeq 1$. This condition immediately gives $J_\perp^{(c)} = -\pi t$. As we show below, using the DMRG studies of chains up to $L = 120$ sites, indeed the transition into the ferromagnetic easy-plane ordering discussed above takes place at $J_\perp^{(c)} \sim -4t$.

4.3. Numerical results at half-filling and $U = 0$

We used the DMRG method to study the ground-state properties of this model. Our calculations have been performed for open chains up to 120 sites using the *infinite-size* version of the DMRG routine. A comparison with the *finite-size* algorithm, which requires more CPU time and memory, does not give a substantial improvement of the results. For most of the numerical results reported here we have kept 400 states in each block, which produces truncation errors smaller than 10^{-7}.

4.3.1. Ground state energy

The asymmetry of this model is clearly seen in Fig. 4.2, where the ground state energy as a function of $J_\perp$ is presented.

Figure 4.2.: Ground-state energy E_0 of the XY-model and the itinerant XY-model as a function of coupling $J_\perp/t$ for a half-filled $L = 100$ chain.

As we observe from Fig. 4.2 in the case of ferromagnetic exchange the ground state energy of the itinerant model becomes very close to that of the spin-$\frac{1}{2}$ XY chain. Further on, Fig. 4.2 indicates a smooth evolution to the limiting case of spin-1/2 antiferromagnetic XY chain at $J_\perp \to \infty$.

4.3.2. Excitation spectrum

Let us start from the limiting case of the itinerant XY model ($U = 0$) and analyse its excitation spectrum. The charge and spin gap for a half-filled L-site system are evaluated by

$$\Delta_c(L) = \frac{1}{2}\left[E_0\left(\frac{L}{2}+1, \frac{L}{2}+1\right) + E_0\left(\frac{L}{2}-1, \frac{L}{2}-1\right)\right.$$
$$\left. -2E_0\left(\frac{L}{2}, \frac{L}{2}\right)\right], \tag{4.39}$$

$$\Delta_s(L) = E_0\left(\frac{L}{2}+1, \frac{L}{2}-1\right) - E_0\left(\frac{L}{2}, \frac{L}{2}\right), \tag{4.40}$$

respectively, where $E_0(N_\uparrow, N_\downarrow)$ is the ground-state energy for $N_\uparrow$ up-spin and $N_\downarrow$ down-spin electrons. The extrapolation for $L \to \infty$ is then performed by fitting a polynomial in $1/L$ to the calculated finite-chain results.

Figure 4.3 displays the extrapolated values as a function of $J_\perp$. We observe the
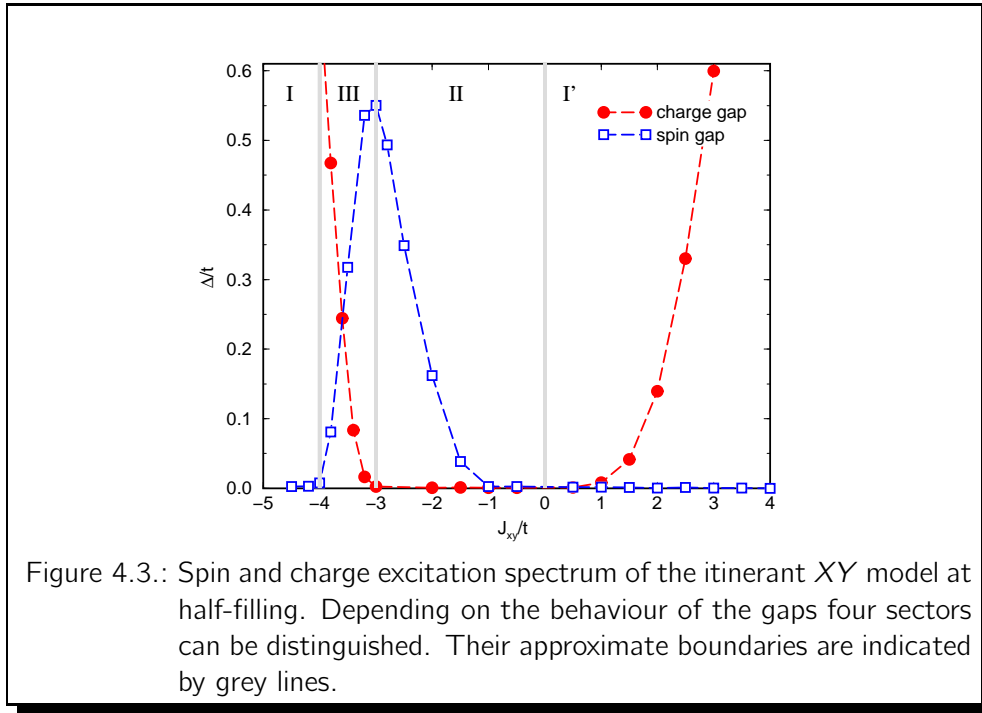
Figure 4.3.: Spin and charge excitation spectrum of the itinerant XY model at half-filling. Depending on the behaviour of the gaps four sectors can be distinguished. Their approximate boundaries are indicated by grey lines.

following four sectors: at $J_\perp > 0$ the system is characterized by gapless spin and gapped charge excitation spectrum, while the weak-coupling ferromagnetic sector exhibits gapless charge and gapful spin degrees of freedom. Moreover, our numerical results show the presence of two new regions. At $J_\perp^{(c1)} \approx -3t$ a charge gap opens, while the spin gap starts to decrease and finally closes at $J_\perp^{(c2)} \approx -4t$. This defines two new sectors: for $J_\perp^{(c2)} < J_\perp < J_\perp^{(c1)}$ both the spin and charge sectors are gapped, while at $J_\perp < J_\perp^{(c2)}$ the spin sectors become gapless. There are no indications for further transitions in the system. Note that similar behaviour

of the gaps, with interchange of spin and charge degrees of freedom, was first observed by Sikkema and Affleck in the pair-hopping model (4.3) [136].

4.3.3. Correlation functions

To investigate the nature of ordering in the different phases we study the behaviour of the correlation functions. In the sectors with gapless excitation spectrum and at half-filling we expect the usual expression for correlation functions

$$C(r) \equiv \langle \mathcal{O}^\dagger(r)\mathcal{O}(0)\rangle \sim A_1 r^{-\theta_1} + (-1)^r A_2 r^{-\theta_2} \qquad (4.41)$$

consisting of a smooth part decaying with exponent θ_1 and an oscillating part decaying with θ_2. In determining the asymptotics of correlation functions (see Sec. 1.2.4 and Sec. 1.3) we focus on the dominating part given by $\theta = \min\{\theta_1, \theta_2\}$. In addition, we average the correlation functions over typically nine numbers of pairs of lattice sites which are separated by the same distance (cf. with Sec. 3.2.6). In the following we will present results for correlation functions in different sectors of the phase diagram.

Sectors I and I' ($\Delta_c \neq 0$, $\Delta_s = 0$): The XY-phases

In Fig. 4.4 we have plotted the longitudinal and transverse spin-spin correlations in the case of strong easy-plane exchange. Although the amplitudes of the trans-
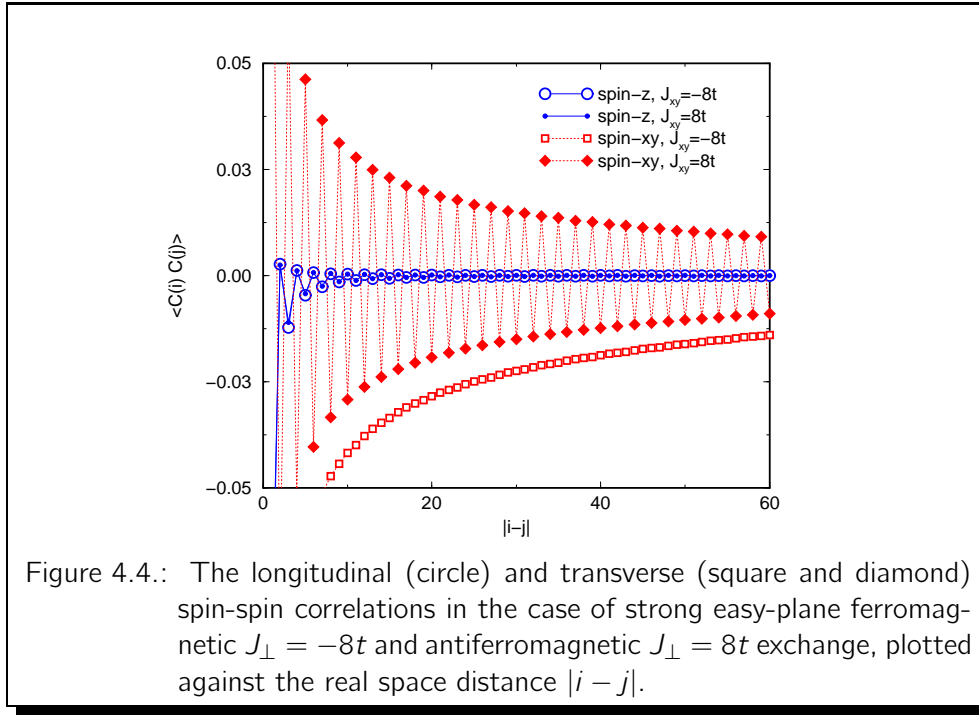
Figure 4.4.: The longitudinal (circle) and transverse (square and diamond) spin-spin correlations in the case of strong easy-plane ferromagnetic $J_\perp = -8t$ and antiferromagnetic $J_\perp = 8t$ exchange, plotted against the real space distance $|i - j|$.

verse correlation functions are different, the estimated exponents are similar[2]. In

[2]Note that the influence of finite size effects on the evaluated exponents is relevant. The determined exponent values for the full set of the data are approximately 5% larger than those which have been calculated for a suitable subset of the data ($10 < |i - j| < 40$).

the case of ferromagnetic exchange we obtained $\theta \approx 0.57$, whereas for the anti-ferromagnetic exchange we have $\theta \approx 0.61$. The results are in a good agreement with the exact value $\theta = 0.5$ obtained for the XY-model [139]. The longitud-inal correlation functions decay faster. The calculated exponents $\theta \approx 1.79$ (for $J_\perp = -8t$) and $\theta \approx 1.66$ (for $J_\perp = 8t$) are close to the exact XY-value $\theta = 2$.

Sector II ($\Delta_c = 0$, $\Delta_s \neq 0$): The TS+SDW$^{(z)}$ regime

Let us now focus on the case of ferromagnetic exchange $J_\perp < 0$ at $U = 0$. The bosonization results predict a suppression of the CDW and singlet correlations, whereas SDW$^{(z)}$ and triplet correlators show identical power-law decay (cf. with Eq. (4.36)). Furthermore, both correlation functions are the dominating instabil-ities in this phase.

Figure 4.5 displays DMRG results for the singlet- and triplet-pair correlation func-tion. One can clearly observe a strong triplet-pair correlation. Note that the
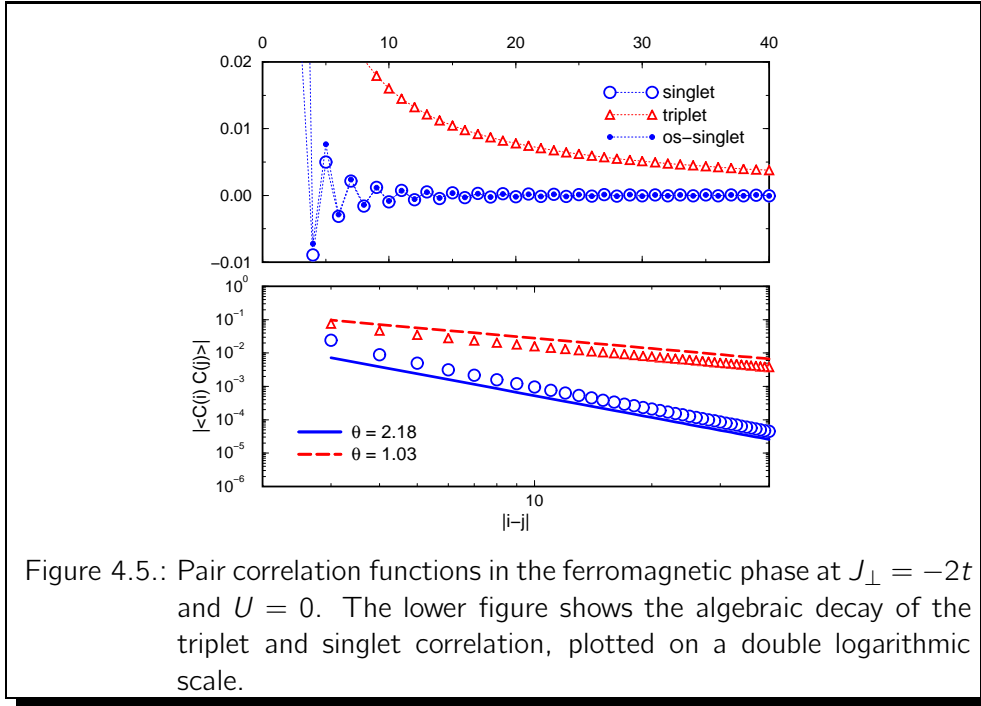
Figure 4.5.: Pair correlation functions in the ferromagnetic phase at $J_\perp = -2t$ and $U = 0$. The lower figure shows the algebraic decay of the triplet and singlet correlation, plotted on a double logarithmic scale.

on-site and extended singlet-pair correlations show an almost identical behaviour. This is expected from the bosonization results (4.21) and (4.22) since the smooth part of the on-site singlet correlations (4.21) does not contribute due to (4.19). In the double logarithmic plot (see lower figure) all correlation functions indicate a power-law decay with fast decaying singlet-pairing correlators ($\theta \approx 2.18$) and a slowly decaying triplet correlation function ($\theta \approx 1.03$). The results are in a good agreement with those predicted by bosonization.

In Fig. 4.6 we show calculations for the longitudinal and transverse spin-spin cor-relation for ferromagnetic exchange ($J_\perp = -2t$). We observe that the correlation functions exhibit an algebraic decay in which the transverse spin-spin correlation

Figure 4.6.: The longitudinal and transverse spin correlation function, plot-
ted at $J_\perp = -2t$ and $U = 0$ (upper figure). The exponents θ
(lower figure) were calculated using a suitable subset of the data
to reduce finite size effects and numerical inaccuracies at large
distances.
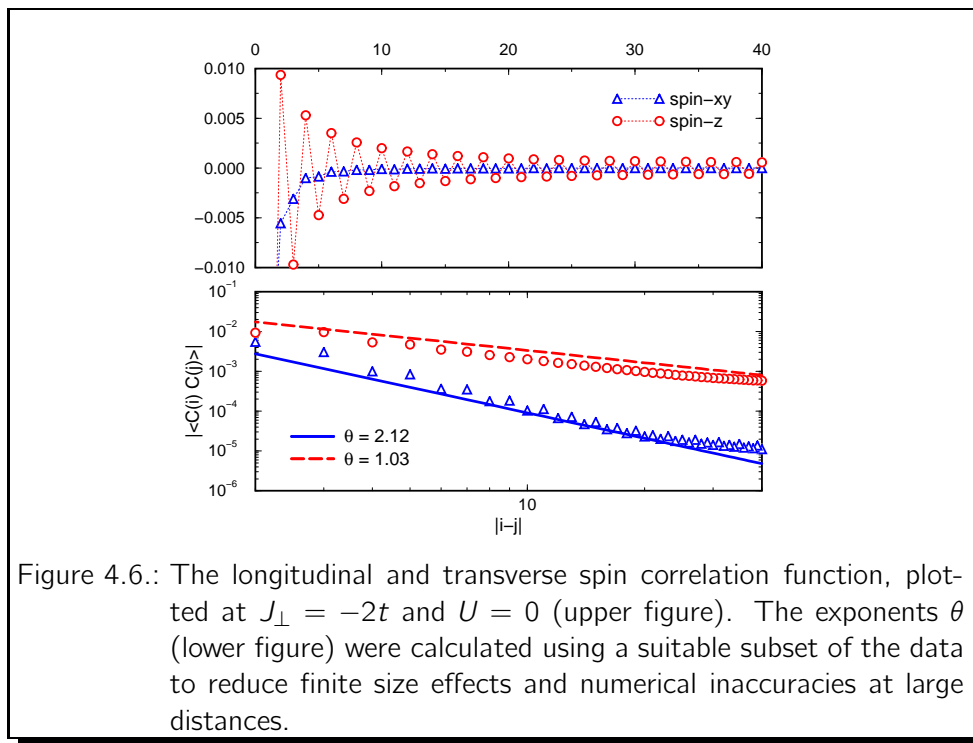
function decays faster. The calculated exponent of the longitudinal spin correl-
ation function is, in agreement with bosonization results, close to that of the
triplet-pairing correlations.

To complete the weak-coupling picture of sector II, we performed calculations for
the density-density correlation. The results are shown in Fig. 4.7. Since in the

Figure 4.7.: The density-density correlation function at $J_\perp = -2t$ and $U = 0$
including the average value of this correlation which removes the
even-odd-r oscillations.
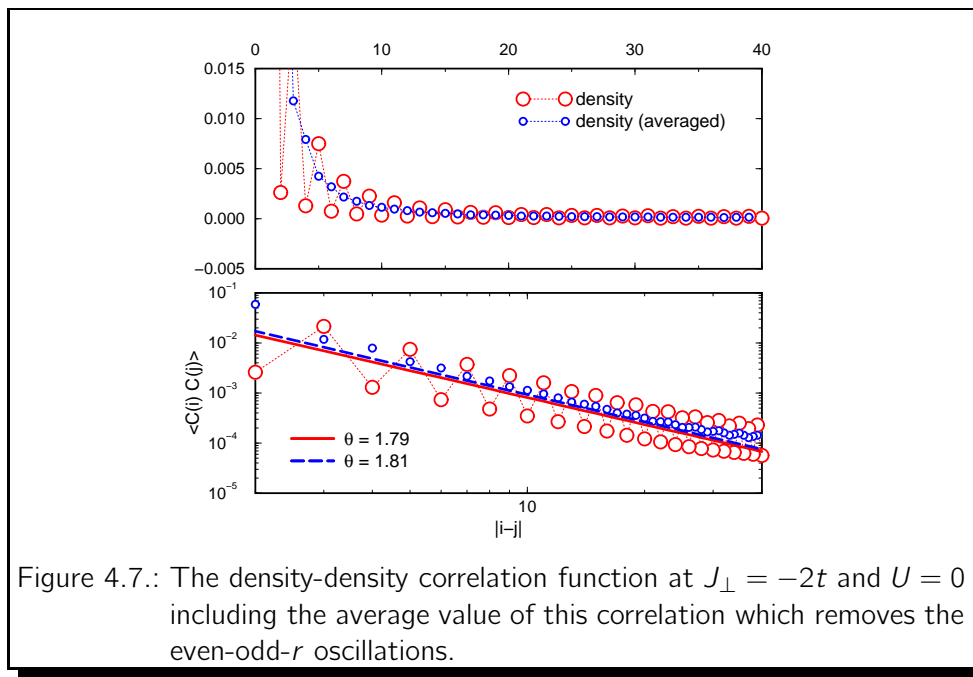
double logarithmic plot we observe strong oscillations we additionally calculate the average value [140]

$$\bar{C}(r) = \frac{1}{4}[C(r-1) + 2C(r) + C(r+1)] \tag{4.42}$$

to smoothen the curve. As its clearly seen from the lower part of Fig. 4.7 the oscillations are removed, but the estimated exponent remains almost unchanged. Thus the DMRG result indicates a fast decay of density-density correlations, in agreement with the bosonization results.

We can conclude that coexisting triplet-pairing and antiferromagnetic SDW$^{(z)}$ ordering are the dominating instabilities in this sector.

Sector III ($\Delta_c \neq 0$, $\Delta_s \neq 0$): The intermediate phase

In this subsection we analyze the asymptotic behaviour of the superconducting and spin-spin correlations in the intermediate phase at $J_\perp = -3.5t$, where $\Delta_c \approx \Delta_s \neq 0$. Note that this phase is absent in the weak-coupling phase diagram (cf. with Fig. 4.1).

In Fig. 4.8 we present DMRG data for the pairing correlation functions (left figure). As is clearly seen from the left figure, especially from the logarithmic plot, the superconducting correlations decay exponentially in agreement with the presence of a charge gap. In addition, we plot the spin-spin correlation functions (right

Figure 4.8.: Pair (left figure) and spin (right figure) correlation functions at $J_\perp = -3.5t$ and $U = 0$, plotted against the real space distance (upper part) and on a logarithmic scale (lower part).
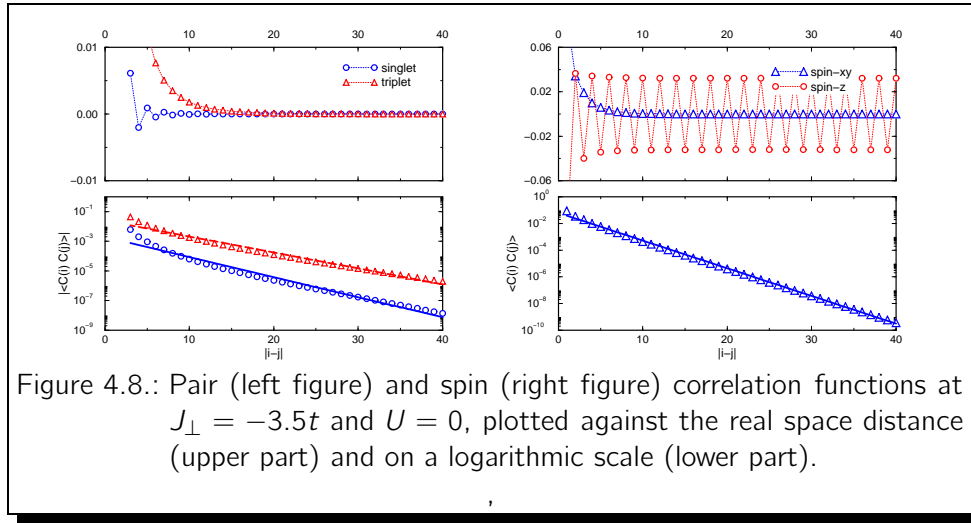
figure). From the logarithmic plot follows that the transverse spin correlation function decay exponentially. In contrast, the longitudinal spin correlation show well-established long-range order. The appearance of LRO is consistent with the $U(1) \otimes Z_2$ spin-symmetry of the present model (4.1). The continuous $U(1)$ symmetry is generated by the operators S^x and S^y, while the discrete Z_2 symmetry comes from the invariance with respect to the $S^z \rightarrow -S^z$ transformation. Since the SDW^z ordering violates the discrete Z_2 and translation symmetries, the true LRO state is not forbidden.

4.4. Numerical results at half-filling and $U \neq 0$

Let us now consider the effects of a repulsive Coulomb interaction on the ground state phase diagram of the model starting with the excitation spectrum.

4.4.1. Excitation spectrum

From the bosonization results we know the general effect of the Coulomb repulsion on the phase diagram which displays itself in an enlargement of the charge gap sectors at the expense of the spin gap sector. Fig. 4.9 shows charge and spin gaps
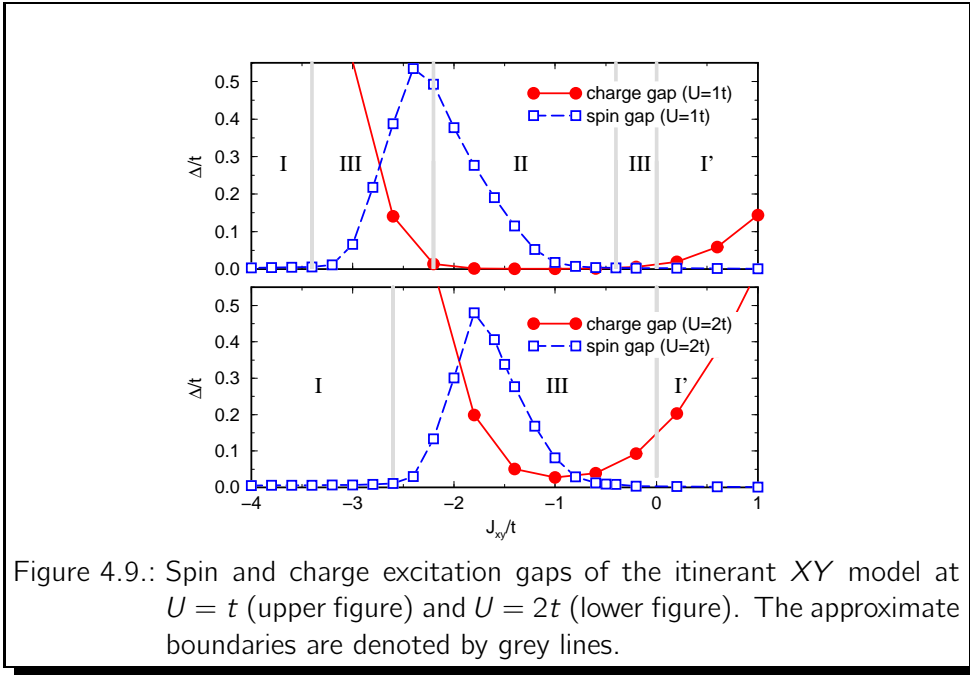

Figure 4.9.: Spin and charge excitation gaps of the itinerant XY model at $U = t$ (upper figure) and $U = 2t$ (lower figure). The approximate boundaries are denoted by grey lines.

for $U = t$ and $U = 2t$. One can clearly see that sectors I and I', where we have a finite charge gap $\Delta_c > 0$, are enlarged. As a consequence the spin-gapped phase (sector II) becomes smaller with increasing U and finally vanishes completely. Already at $U = 2t$ the charge gap is always finite. Thus the main effect of the presence of Coulomb interactions is the suppression of sector II, i.e. a reduction of the region with dominating superconducting correlations. In analogy with the $U = 0$ case we conclude that the sectors with magnetic correlations become dominating.

4.4.2. Correlation functions

In the following we analyze the effect of the Coulomb interactions on pair and spin correlation functions. We will focus on the behaviour in sectors II and III where $\Delta_c = 0$, $\Delta_s \neq 0$ and $\Delta_c \neq 0$, $\Delta_s \neq 0$, respectively.

The TS + SDW$^{(z)}$ phase

In this subsection as a representative point we consider the coupling $J_\perp = -1.5t$ at $U = t$. The phase is characterized by a spin gap of magnitude $\Delta_s \approx 0.13t$ and
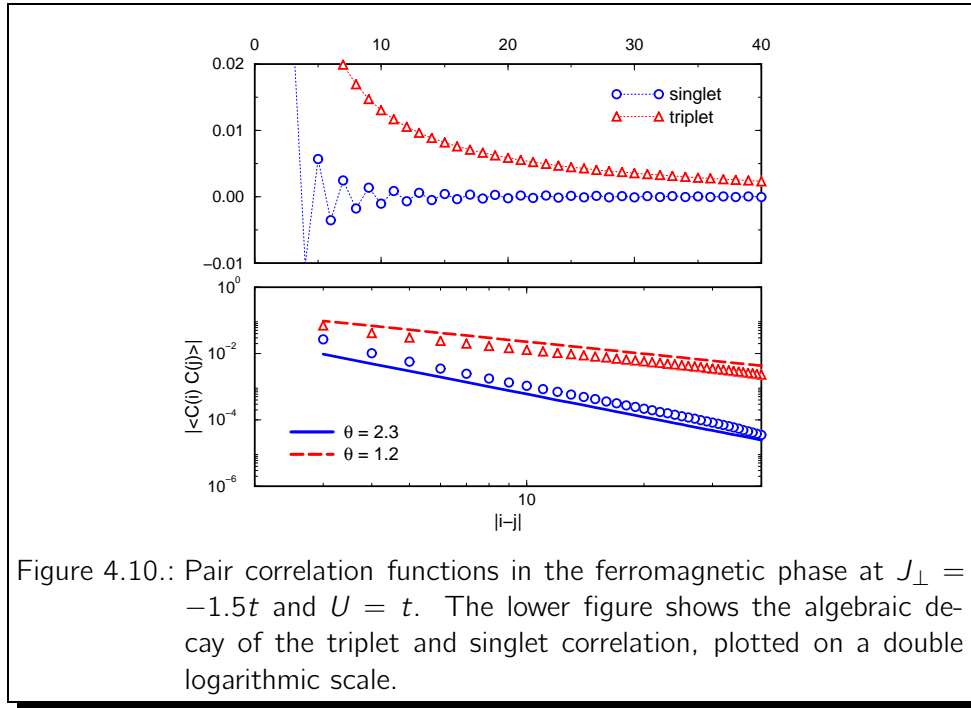

Figure 4.10.: Pair correlation functions in the ferromagnetic phase at $J_\perp = -1.5t$ and $U = t$. The lower figure shows the algebraic decay of the triplet and singlet correlation, plotted on a double logarithmic scale.
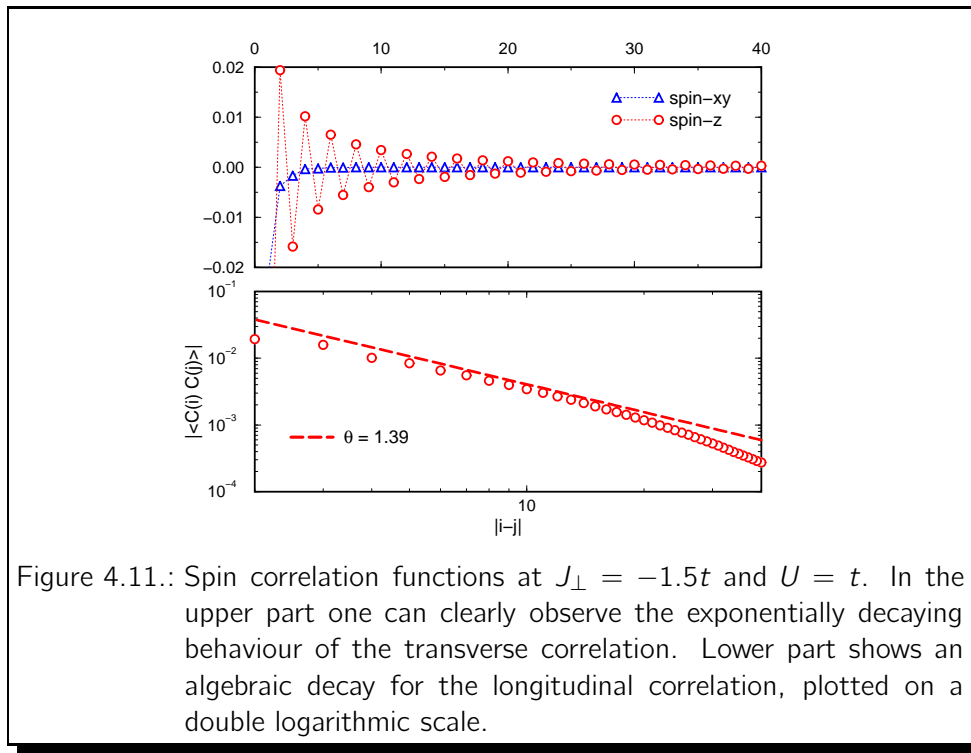

Figure 4.11.: Spin correlation functions at $J_\perp = -1.5t$ and $U = t$. In the upper part one can clearly observe the exponentially decaying behaviour of the transverse correlation. Lower part shows an algebraic decay for the longitudinal correlation, plotted on a double logarithmic scale.

massless charge mode. The asymptotic behaviour of the pair and spin correlation functions is plotted in Fig. 4.10 and Fig. 4.11, respectively. One can clearly see that the triplet-pairing and longitudinal spin-spin correlations represent the dominating instabilities in the system. Unfortunately the accuracy of the numerics is not sufficient in this case to verify that the exponents are still exactly identical. Instead, we find $\theta \approx 1.2$ (triplet pairing) and $\theta \approx 1.39$ (longitudinal spin).

The LRO SDW$^{(z)}$ phase

In this subsection we compute the correlation functions at $U = 2t$ and $J_\perp = -2t$. The presence of a charge gap $\Delta_c \approx 0.38t$ leads now to an exponential decay of superconducting correlations. On the other hand, as is clearly seen from Fig. 4.12,
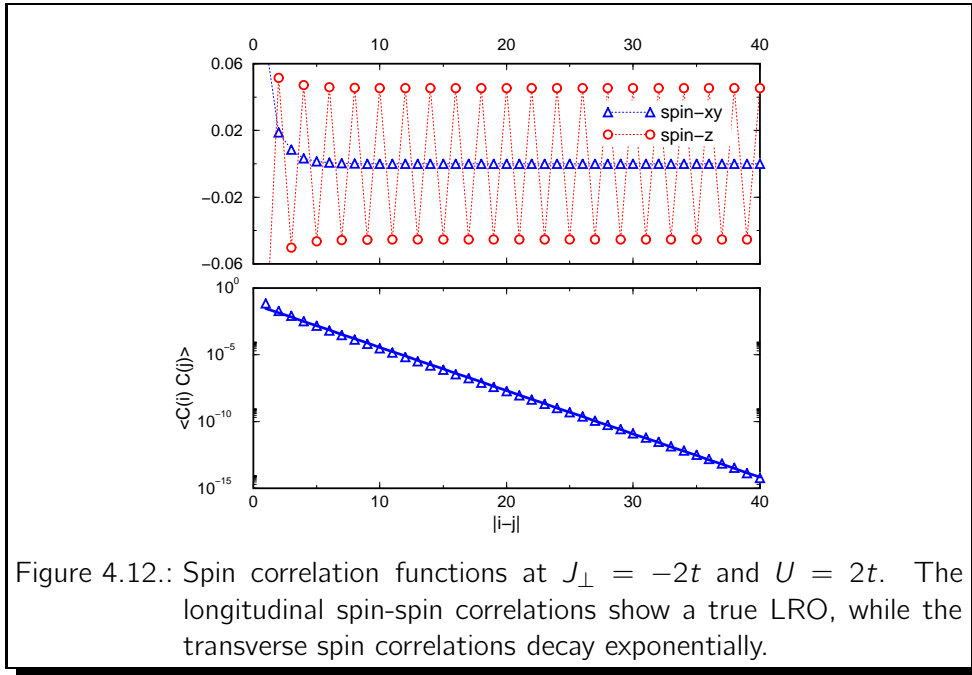
Figure 4.12.: Spin correlation functions at $J_\perp = -2t$ and $U = 2t$. The longitudinal spin-spin correlations show a true LRO, while the transverse spin correlations decay exponentially.

the longitudinal spin-spin correlations show a true LRO while the transverse spin correlations decay exponentially.

Note that this phase is equivalent to the intermediate sector at $-4t \leq J_\perp \leq -3t$ and $U = 0$, showing true LRO SDW$^{(z)}$ and exponentially decaying transverse spin and pair correlations.

The ferromagnetic phase

In this subsection we use as an representative point $U = 2t$ and in addition $J_\perp = -4t$. As one can observe from Fig. 4.13 the spin-spin correlation functions exhibit an algebraic decay in which the longitudinal correlation decays faster. The transverse ferromagnetic spin correlation is almost identical to that of the standard XY-chain.

Figure 4.13.: Spin correlation functions at $J_\perp = -4t$ and $U = 2t$ showing a power-law decay in which the longitudinal correlation decays faster.
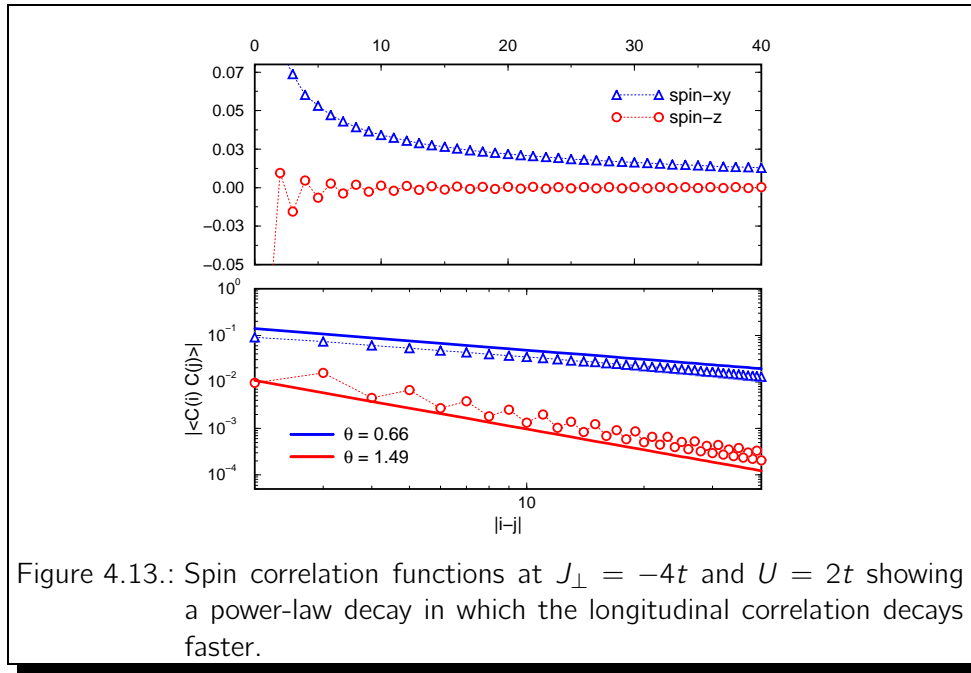
4.5. Physical properties at quarter-filling

In this section we will extend our analysis to the case of a quarter-filled band. Let us start from the limiting case of the itinerant XY model ($U = 0$) and analyse its excitation spectrum.
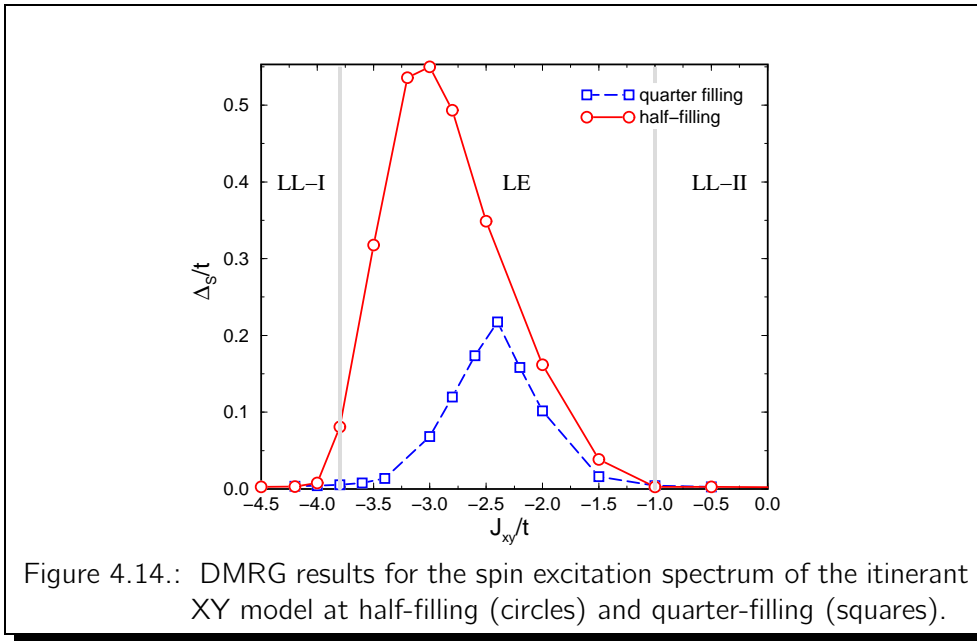
4.5.1. Excitation spectrum at $U = 0$

Depending on the value of $J_\perp/t$ the quarter-filled model (4.1) belongs either to a TL liquid with gapless excitation spectrum or to a LE phase described by a spin gap and gapless charge degrees of freedom. But the charge excitation spectrum is always gapless, as in the Hubbard model with $n < 1$.

Figure 4.14 displays the extrapolated values as function of $J_\perp$. We observe two transitions: up to $J_\perp \geq -t$ the system belongs to the TLL universality class with gapless excitation spectrum. With increasing ferromagnetic exchange the spin gap increases and the system is described by the LE phase. Below $J_\perp \approx -3.7t$ the gap is closed and once again the system is represented by a TL liquid. In contrast to the half-filled case the spin gaps are much smaller.

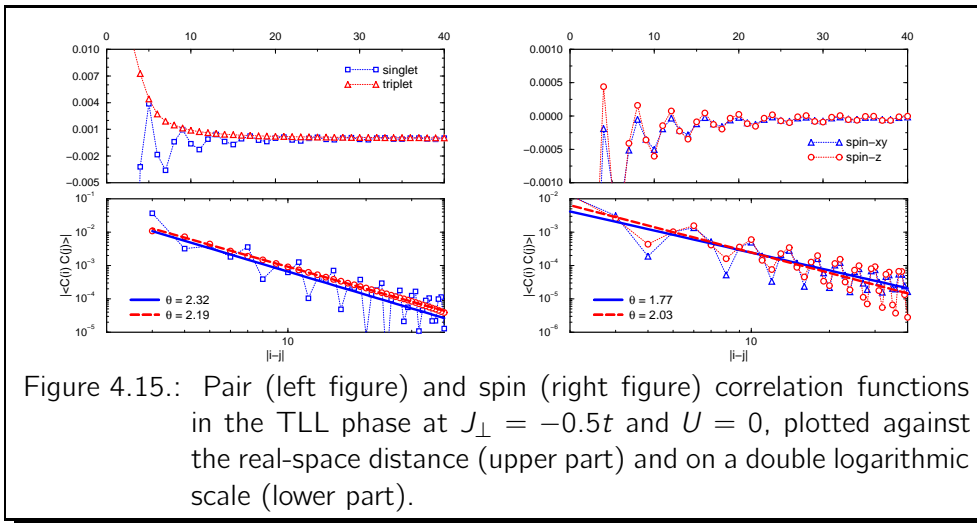Now we are going to analyze the behaviour of pair and spin correlation functions.

4.5.2. Correlation functions

At first, we focus our study on the gapless phase expecting a power-law behaviour for all correlation functions.

Figure 4.14.: DMRG results for the spin excitation spectrum of the itinerant XY model at half-filling (circles) and quarter-filling (squares).

The TL phases ($\Delta_c = 0$, $\Delta_s = 0$):

The TL liquid is characterized by a gapless excitation spectrum with algebraically decaying correlation functions. Fig. 4.15 shows the numerical data for the pair and spin correlations at $J_\perp = -0.5t$. In agreement with the TL liquid prediction,

Figure 4.15.: Pair (left figure) and spin (right figure) correlation functions in the TLL phase at $J_\perp = -0.5t$ and $U = 0$, plotted against the real-space distance (upper part) and on a double logarithmic scale (lower part).

one can clearly observe the power-law behaviour of all correlation functions. The LE phase is more interesting, because the presence of a spin gap favours pair correlations. Thus, next we will focus on the spin gapped phase.

The LE phase ($\Delta_c = 0$, $\Delta_s \neq 0$):

We concentrate on the case of ferromagnetic exchange $J_\perp = -2t$ with $U = 0$.
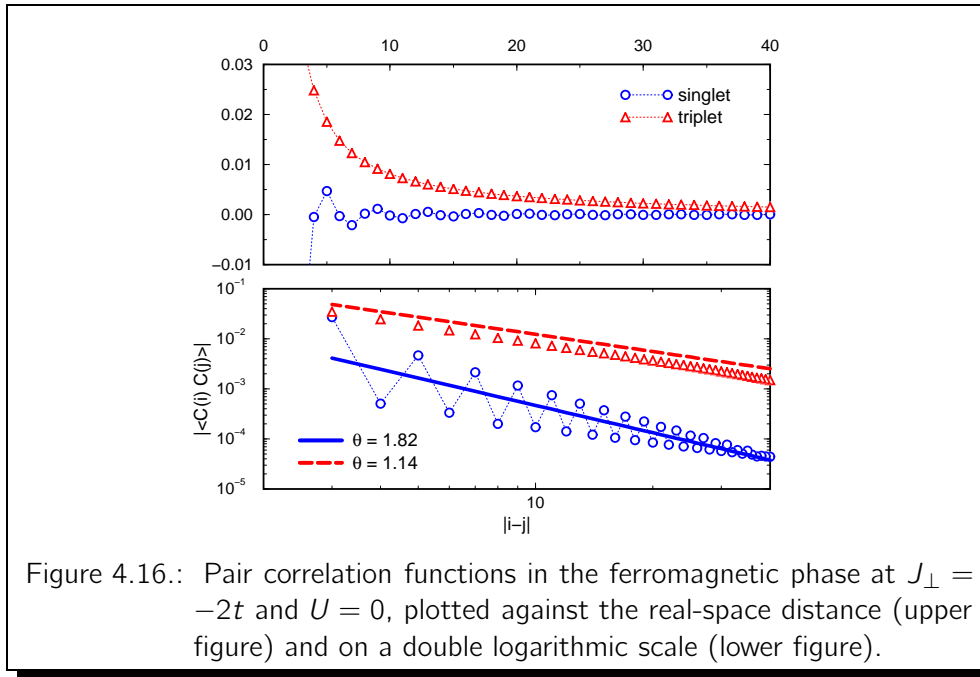
Figure 4.16.: Pair correlation functions in the ferromagnetic phase at $J_\perp = -2t$ and $U = 0$, plotted against the real-space distance (upper figure) and on a double logarithmic scale (lower figure).
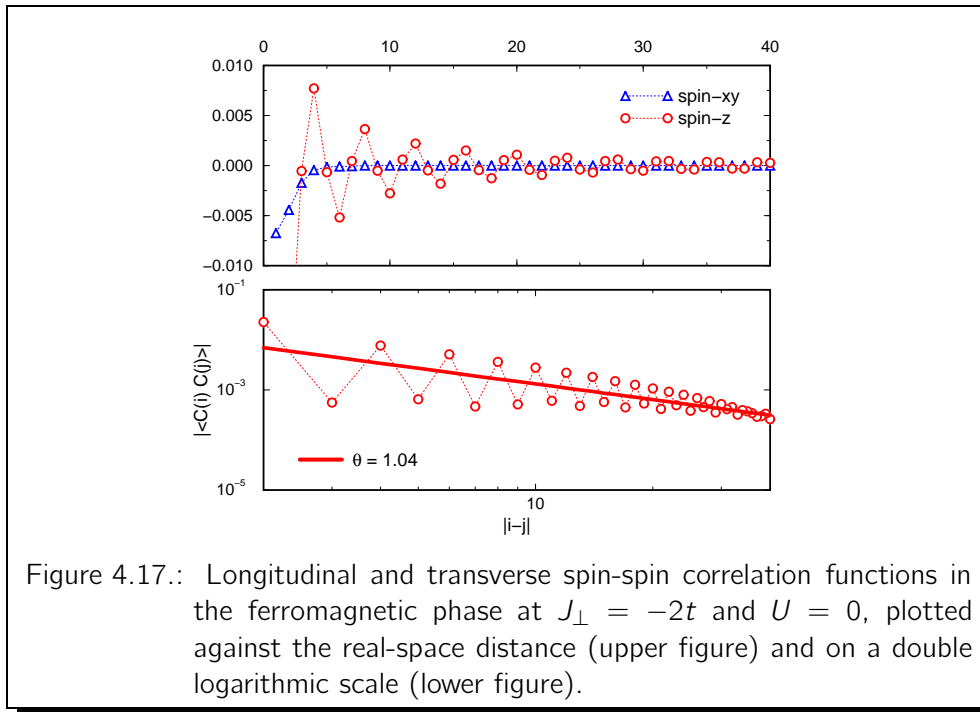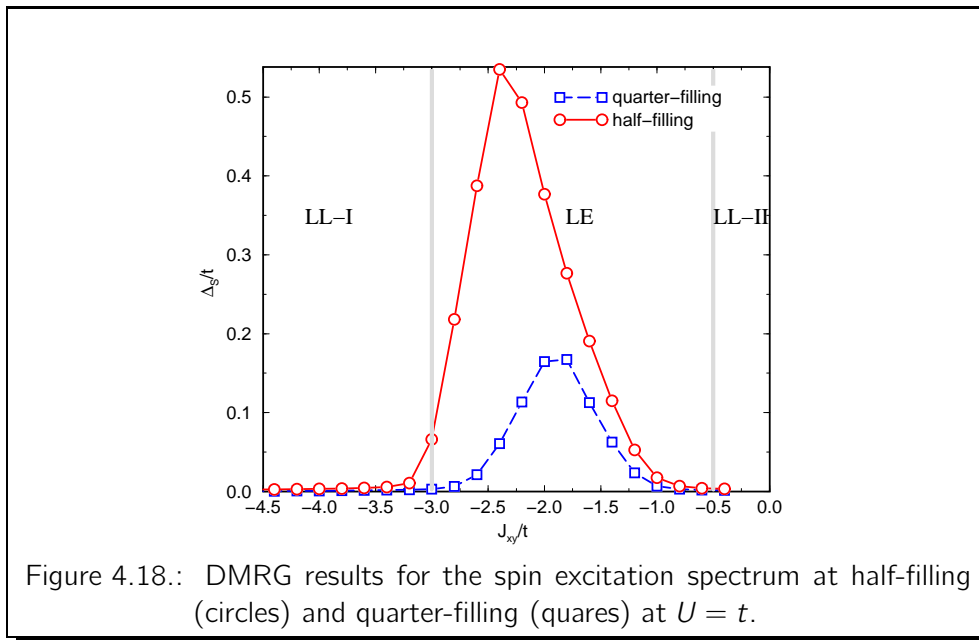

Figure 4.17.: Longitudinal and transverse spin-spin correlation functions in the ferromagnetic phase at $J_\perp = -2t$ and $U = 0$, plotted against the real-space distance (upper figure) and on a double logarithmic scale (lower figure).

The ground state of the $SU(2)$ spin-symmetric LE model is characterized by exponentially decaying SDW and triplet-pair correlation functions and by CDW and singlet-pairing correlators showing power-law behaviour. However, in contrast to the LE model, the model of interest possesses only the ordinary $U(1)$ spin-symmetry. Therefore, differences in the decay behaviour are expected. Already Fig. 4.16 indicates a quite different picture. One can clearly observe that the

triplet-pair correlator decays algebraically and definitively not exponentially. The singlet-paring correlation function however shows an unchanged correlation behaviour, i.e. it has a power-law decay. In Fig. 4.17 we display the spin-spin correlations, where the transverse spin-spin correlations decay exponentially while the longitudinal spin-spin correlations exhibit power-law decay. Note that the estimated exponents of the triplet pair and the longitudinal spin correlations are quite similar.

4.5.3. Excitation spectrum at $U = t$

Due to the absence of a charge gap, the influence of the Coulomb interaction U leads only to quantitative effects. Therefore, we investigate the $U = t$ case. Fig. 4.18 depicts the excitation spectrum at $U = t$, with a shift of all boundaries
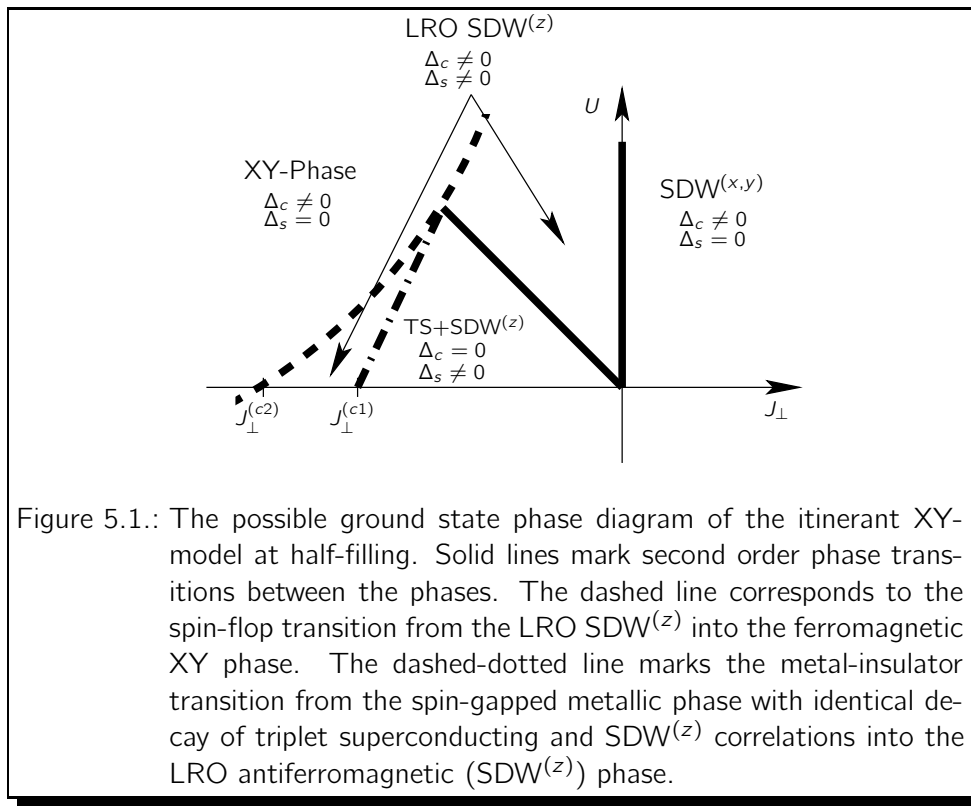

Figure 4.18.: DMRG results for the spin excitation spectrum at half-filling (circles) and quarter-filling (quares) at $U = t$.

which separates the phases. Additionally, one can clearly observe a small spin gapped region in the quarter-filled case.

5. Conclusion and Outlook

Recent experimental findings show evidence for the competition or even coexistence of triplet superconductivity and ferromagnetism. Based on these observations various models of strongly correlated electron systems showing proximity of (ferro) magnetic and (triplet) superconducting phases have been studied as attempt to construct a theoretical model for new superconducting materials.

We focused our investigations on a rather simple extension of the Hubbard model including transverse spin exchange between electrons on nearest-neighbour sites. The one-dimensional version of this model has an extremely rich weak-coupling phase diagram (see Fig. 4.1). In the case of a half-filled band the ground state phase diagram is characterized by two insulating antiferromagnetic phases with easy plane anisotropy and the spin gapful metallic phase with an identical decay of the triplet superconducting and spin-density wave ($SDW^{(z)}$) instabilities.

Our numerical results from the density matrix renormalization group calculations show that the phase diagram obtained in the weak-coupling limit using the bosonization technique has to be modified (see Fig. 5.1). In the case of vanishing

LRO $SDW^{(z)}$

$\Delta_c \neq 0$
$\Delta_s \neq 0$

U

XY-Phase

$\Delta_c \neq 0$
$\Delta_s = 0$

$SDW^{(x,y)}$

$\Delta_c \neq 0$
$\Delta_s = 0$

$TS+SDW^{(z)}$
$\Delta_c = 0$
$\Delta_s \neq 0$

$J_\perp^{(c2)}$ $J_\perp^{(c1)}$ $J_\perp$

Figure 5.1.: The possible ground state phase diagram of the itinerant XY-model at half-filling. Solid lines mark second order phase transitions between the phases. The dashed line corresponds to the spin-flop transition from the LRO $SDW^{(z)}$ into the ferromagnetic XY phase. The dashed-dotted line marks the metal-insulator transition from the spin-gapped metallic phase with identical decay of triplet superconducting and $SDW^{(z)}$ correlations into the LRO antiferromagnetic ($SDW^{(z)}$) phase.

on-site Coulomb interactions,the behaviour of spin and charge gaps as function of the spin-coupling $J_\perp$ allows to distinguish four different phases:
For antiferromagnetic interactions $J_\perp > 0$ only one phase is present.

❶ The spin gap vanishes, but the charge gap is always finite. The observed behaviour of the correlation functions indicates a smooth evolution to the limiting case of spin-1/2 antiferromagnetic XY chain at $J_\perp \to \infty$.

For ferromagnetic couplings $J_\perp < 0$ three different phases appear.

❷ Already for weak interactions a spin gap opens, but the charge sector is gapless. Here SDW$^{(z)}$ and triplet correlations, which decay with similar power-laws, are dominating, i.e. this regime exhibits a coexistence of anti-ferromagnetic ordering and triplet superconductivity.

❸ At $J_\perp^{(c1)} \approx -3t$ the spin gap is maximal and a charge gap opens. This intermediate phase, that extends up to $J_\perp^{(c2)} \approx -4t$ shows long-range order in the longitudinal spin correlation, whereas superconducting correlations are surpressed and decay exponentially as expected for the case of a finite charge gap.

❹ Finally, at $J_\perp > -4t$ via a spin-flop transition the system again enters a XY phase characterized by vanishing spin but finite charge gap. Here the behaviour is similar to the ferromagnetic XY model.

The presence of a repulsive on-site Coulomb interaction U has a strong effect on the phase diagram. Generically it leads to an enlargement of the sectors with nonvanishing charge gap at the expense of the sectors with spin gap. Already at $U = 2t$ the charge gap is finite for all values of the exchange coupling $J_\perp$. Therefore the phase where antiferromagnetism and triplet superconductivity coexist is no longer observed and magnetic correlations become dominant everywhere. Only for small values of the Coulomb interaction there is still a finite window of coexistence possible.
We extend our analysis to the case of a quarter-filled band. Depending on the value $J_\perp/t$ the model belongs either to a gapless excitation phase or to a spin gapped phase with gapless charge degrees of freedom. In the spin gapped phase we have shown that this regime is characterized by the coexistence of antiferro-magnetic ordering and triplet superconductivity. Preliminary results indicate that the Coulomb interactions only lead to a quantitative modification.
Further studies have to clarify if the two gapless phases exhibit similar physical properties. In addition, the influence of the Coulomb interaction has to be ex-amined in more detail. And finally, the nature of superconducting pairs (e.g. hole or electron) has to be analyzed.

A. Implementation of the fermion sign in the DMRG method

A common approach to numerically treating a quantum lattice system is to diagonalize the Hamiltonian matrix in which the basis states are written in the second quantization, i.e. the occupation number formalism. A system with N identical fermions and L sites is described by the basis states

$$|n_1, \ldots, n_\ell, \ldots, n_L) \equiv |n_1) \otimes \ldots \otimes |n_\ell) \otimes \ldots \otimes |n_L) \tag{A.1}$$

telling how many particles $n_\ell = n_{\ell,\uparrow} + n_{\ell,\downarrow}$ are in each single particle state. Within this formalism all operators may be expressed in terms of creation ($c_{\ell,\sigma}^\dagger$) and annihilation ($c_{\ell,\sigma}$) operators obeying the important anticommutation rules

$$\left[c_{\ell,\sigma}, c_{\ell',\sigma'}^\dagger \right] = c_{\ell,\sigma} c_{\ell',\sigma'}^\dagger + c_{\ell',\sigma'}^\dagger c_{\ell,\sigma} = \delta_{\ell\ell'} \delta_{\sigma\sigma'}, \tag{A.2}$$

$$\left[c_{\ell,\sigma}, c_{\ell',\sigma'} \right] = \left[c_{\ell,\sigma}^\dagger, c_{\ell',\sigma'}^\dagger \right] = 0. \tag{A.3}$$

A minus sign is introduced whenever places of two operators are interchanged. Consequently, this sign should be carefully tracked during the DMRG procedure. It is useful to define new creation and annihilation operators which already include the fermion sign.

Let us assume following alignment of up- and down-spin particles

$$|\uparrow\downarrow) = c_{\ell,\uparrow}^\dagger c_{\ell,\downarrow}^\dagger |0) \tag{A.4}$$

in the case when the single site state $|n_\ell)$ is occupied by two particles with opposite spins. When applying $c_{\ell,\sigma}^\dagger$ to $|n_1, \ldots, n_\ell, \ldots, n_L)$, the number of particles in front of position ℓ and n_ℓ determine the fermion sign. More precisely, in the left block
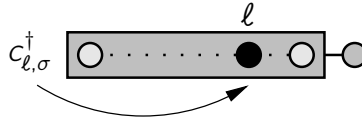
we define

$$c_{\ell,\uparrow}^\dagger |n_1, \ldots, n_{\ell-1}, 0, \ldots) = (-1)^{\sum_{k<\ell} n_k} |n_1, \ldots, n_{\ell-1}, \uparrow, \ldots), \tag{A.5}$$

$$c_{\ell,\uparrow}^\dagger |n_1, \ldots, n_{\ell-1}, \downarrow, \ldots) = (-1)^{\sum_{k<\ell} n_k} |n_1, \ldots, n_{\ell-1}, \uparrow\downarrow, \ldots), \tag{A.6}$$

$$c_{\ell,\downarrow}^\dagger |n_1, \ldots, n_{\ell-1}, 0, \ldots) = (-1)^{\sum_{k<\ell} n_k} |n_1, \ldots, n_{\ell-1}, \downarrow, \ldots), \tag{A.7}$$
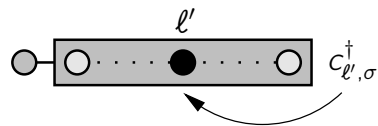
$$c_{\ell,\downarrow}^\dagger |n_1, \ldots, n_{\ell-1}, \uparrow, \ldots) \underset{(A.4)}{=} (-1)^{\sum_{k<\ell} n_k + 1} |n_1, \ldots, n_{\ell-1}, \uparrow\downarrow, \ldots). \tag{A.8}$$

The new creation operators of the *left block* are then given by

$$\tilde{c}^\dagger_{\ell,\uparrow} \;\equiv\; c^\dagger_{\ell,\uparrow}(-1)^{N_{\ell-1}} \qquad \text{and} \tag{A.9}$$

$$\tilde{c}^\dagger_{\ell,\downarrow} \;\equiv\; c^\dagger_{\ell,\downarrow}(-1)^{N_{\ell-1}+n_{\ell,\uparrow}}\,, \tag{A.10}$$

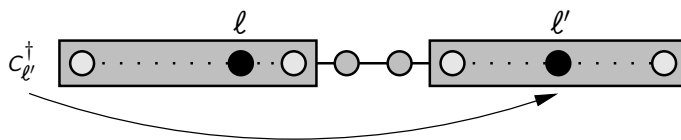where we have defined $N_\ell = \sum_{k=1}^{\ell} n_k$. However, in the right block

one gets

$$(\ldots,0,n_{\ell'-1},\ldots,n_1|\,c^\dagger_{\ell',\uparrow} \;=\; (-1)^{N_{\ell'-1}}\,(\ldots,\uparrow,n_{\ell'-1},\ldots,n_1|, \tag{A.11}$$

$$(\ldots,\downarrow,n_{\ell'-1},\ldots,n_1|\,c^\dagger_{\ell',\uparrow} \;\underset{(A.4)}{=}\; (-1)^{N_{\ell'-1}+1}\,(\ldots,\uparrow\downarrow,n_{\ell'-1},\ldots,n_1|, \tag{A.12}$$

$$(\ldots,0,n_{\ell'-1},\ldots,n_1|\,c^\dagger_{\ell',\downarrow} \;=\; (-1)^{N_{\ell'-1}}\,(\ldots,\downarrow,n_{\ell'-1},\ldots,n_1|, \tag{A.13}$$

$$(\ldots,\uparrow,n_{\ell'-1},\ldots,n_1|\,c^\dagger_{\ell',\downarrow} \;=\; (-1)^{N_{\ell'-1}}\,(\ldots,\uparrow\downarrow,n_{\ell'-1},\ldots,n_1|. \tag{A.14}$$

Thus connecting left and right block together

only the sign of the *right block* operators has to be modified, i.e.

$$\tilde{\tilde{c}}^\dagger_{\ell',\uparrow} \;\equiv\; \tilde{c}^\dagger_{\ell',\uparrow}(-1)^{N_{\text{tot}}} = c^\dagger_{\ell',\uparrow}(-1)^{N_{\text{tot}}}(-1)^{N_{\ell'-1}} \quad \text{and} \tag{A.15}$$

$$\tilde{\tilde{c}}^\dagger_{\ell',\downarrow} \;\equiv\; \tilde{c}^\dagger_{\ell',\downarrow}(-1)^{N_{\text{tot}}} = c^\dagger_{\ell',\downarrow}(-1)^{N_{\text{tot}}}(-1)^{N_{\ell'-1}+n_{\ell',\uparrow}}\,, \tag{A.16}$$

with N_{tot} describing the particle number of the superblock.
A fermionic correlation function like

$$C(|\ell - \ell'|) = \left\langle \tilde{c}^\dagger_{\ell,\sigma}\,\tilde{\tilde{c}}_{\ell',\sigma'} \right\rangle \tag{A.17}$$

has to be computed in terms of these new operators. Note that all these types of correlations give wrong behaviour if the implementation of the fermionic sign is neglected.

B. Noninteracting fermions

In the limiting case $U = 0$ the 1D Hubbard model reduces to that of free fermions. The Hamiltonian with open boundary conditions (OBC) then reads

$$\mathcal{H} = -t \sum_{\ell=1}^{L-1} \sum_{\sigma=\pm 1} \left(c_{\ell,\sigma}^{\dagger} c_{\ell+1,\sigma} + c_{\ell+1,\sigma}^{\dagger} c_{\ell,\sigma} \right) , \tag{B.1}$$

where t represents the strength of the hopping and L the length of the chain. This model is completely equivalent to the model of spinless free fermions (SFF) due to the fact that the two spin projections $\sigma = \uparrow$ and $\sigma = \downarrow$ are independent. The SFF model, which can be mapped to the spin-1/2 XX chain by means of the Jordan-Wigner transformation, is the simplest exactly solvable strongly correlated model [139, 141]. The main advantage of this model is that its physical quantities like the energy spectrum or the ground-state correlation functions can be calculated rather easily for any finite chain length, even for OBC, as in the standard DMRG algorithm. Therefore, we will use the model of noninteracting fermions, which is also a limiting case of our model, as a test system in order to analyze the accuracy of our DMRG routine.

B.1. Ground-State energy

We can diagonalize the Hamiltonian (B.1) by means of Fourier transformation to obtain

$$
\begin{aligned}
\mathcal{H} &= -t \sum_{\ell,\sigma} \frac{1}{L} \left(\sum_{k_1,k_2} e^{-i(k_1-k_2)\ell} \, e^{ik_2} + \sum_{k_1,k_2} e^{-i(k_1-k_2)\ell} \, e^{-ik_1} \right) c_{k_1,\sigma}^{\dagger} c_{k_2,\sigma} \\
&= -t \sum_{k,\sigma} \left(e^{ik} + e^{-ik} \right) c_{k,\sigma}^{\dagger} c_{k,\sigma} \\
&= \sum_{k,\sigma} \varepsilon(k) \, c_{k,\sigma}^{\dagger} c_{k,\sigma} \quad \text{with} \quad \varepsilon(k) = -2t \, \cos(k) .
\end{aligned} \tag{B.2}
$$

The ground-state energy is then given by

$$
\begin{aligned}
E_0 &= \langle \mathcal{H} \rangle = \sum_{k,\sigma} \varepsilon(k) \, \langle c_{k,\sigma}^{\dagger} c_{k,\sigma} \rangle = \sum_{k,\sigma} \varepsilon(k) \, n_\sigma(k) \\
&= -4t \sum_{k<k_F} \cos(k) ,
\end{aligned} \tag{B.3}
$$

where $n_\sigma(k)$ denotes the momentum distribution for spin σ with $n_\sigma(k) = 1$ for all $k < k_F = \pi N/(2L)$ and zero otherwise. Due to the OBC, the momentum k takes the values $k = \pi m/(L+1)$ with $m = 1, \ldots, N_\sigma/L.,$

In Figure B.1 the exact ground-state energy $e_0 = E_0/L$ is compared with DMRG results for the half-filled band (left figure) and quarter-filled band (right figure). The DMRG calculations were performed with the *infinite-system* algorithm for chains up to $L = 160$ lattice sites with $m = 400$ states retained. The discrep-
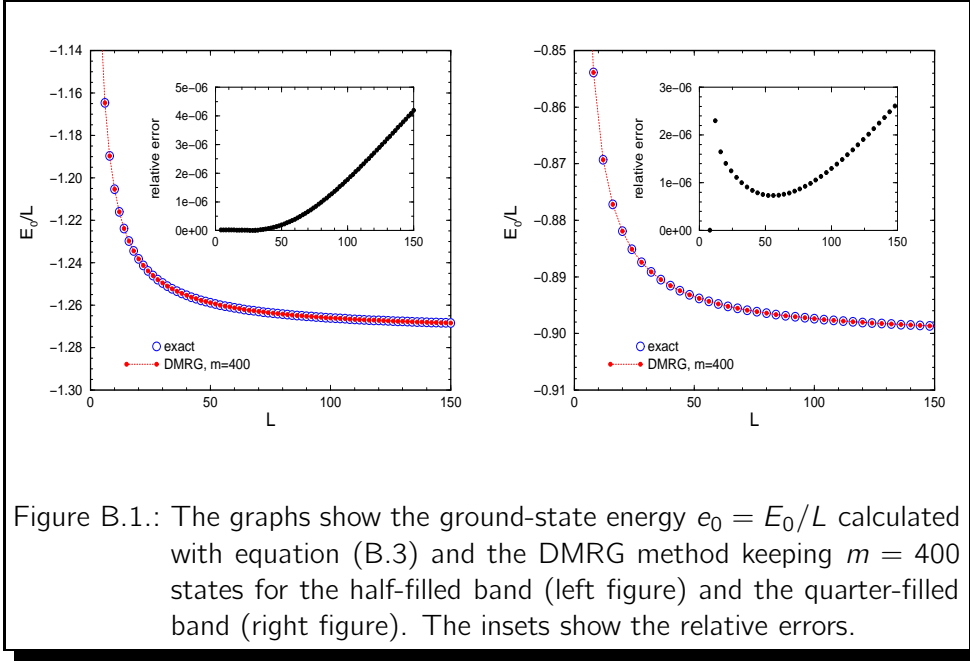

Figure B.1.: The graphs show the ground-state energy $e_0 = E_0/L$ calculated with equation (B.3) and the DMRG method keeping $m = 400$ states for the half-filled band (left figure) and the quarter-filled band (right figure). The insets show the relative errors.

ancies $\Delta e_0 \equiv e_0(\text{DMRG}) - e_0(\text{exact})$ are always positive in accordance with the statement that the DMRG is a variational method. Due to the truncation error in the DMRG procedure, the relative errors $\delta e \equiv \Delta e_0/|e_0(\text{exact})|$, plotted in the insets, increase with increasing chain length. Nevertheless, the agreement with the exact results is quite good.

B.2. Two-point correlations functions

In order to evaluate correlation functions, we make use of the Wick theorem. For instance, the triplet-pair correlation function

$$C_{TS}(|n - m|) \;=\; \langle \psi | \mathcal{O}_{TS}^\dagger(n) \mathcal{O}_{TS}(m) | \psi \rangle \tag{B.4}$$

separates into a product of pairs:

$$
\begin{aligned}
C_{TS}^{\text{free}}(|n - m|) \;=\;& \frac{1}{2} \left(\langle c_{n,\uparrow}^\dagger c_{m,\uparrow} \rangle \langle c_{n+1,\downarrow}^\dagger c_{m+1,\downarrow} \rangle - \langle c_{n,\uparrow}^\dagger c_{m+1,\uparrow} \rangle \langle c_{n+1,\downarrow}^\dagger c_{m,\downarrow} \rangle \right. \\
& \left. - \langle c_{n,\downarrow}^\dagger c_{m+1,\downarrow} \rangle \langle c_{n+1,\uparrow}^\dagger c_{m,\uparrow} \rangle + \langle c_{n,\downarrow}^\dagger c_{m,\downarrow} \rangle \langle c_{n+1,\uparrow}^\dagger c_{m+1,\uparrow} \rangle \right) \\
\equiv\;& \langle q_{r,\uparrow} \rangle \langle q_{r,\downarrow} \rangle - \frac{1}{2} \left(\langle q_{r+1,\uparrow} \rangle \langle q_{r-1,\downarrow} \rangle + \langle q_{r+1,\downarrow} \rangle \langle q_{r-1,\uparrow} \rangle \right) \\
\equiv\;& \langle q_r \rangle^2 - \langle q_{r+1} \rangle \langle q_{r-1} \rangle \,, \tag{B.5}
\end{aligned}
$$

where the vacuum expectation value $\langle q_{r,\sigma} \rangle = \langle c_{n,\sigma}^\dagger c_{m,\sigma} \rangle$ denotes a propagator with distance $r \equiv |n - m|$ and spin σ.

The singlet-pair, on-site singlet-pair, density-density and spin-spin correlations can be obtained in a similar way:

$$C_{ES}^{free}(r) \equiv \langle q_r \rangle^2 + \langle q_{r+1} \rangle \langle q_{r-1} \rangle \,, \tag{B.6}$$

$$C_{OS}^{free}(r) = 2\, C_{SDW}^{free}(r) \equiv -\langle q_r \rangle^2 \,, \tag{B.7}$$

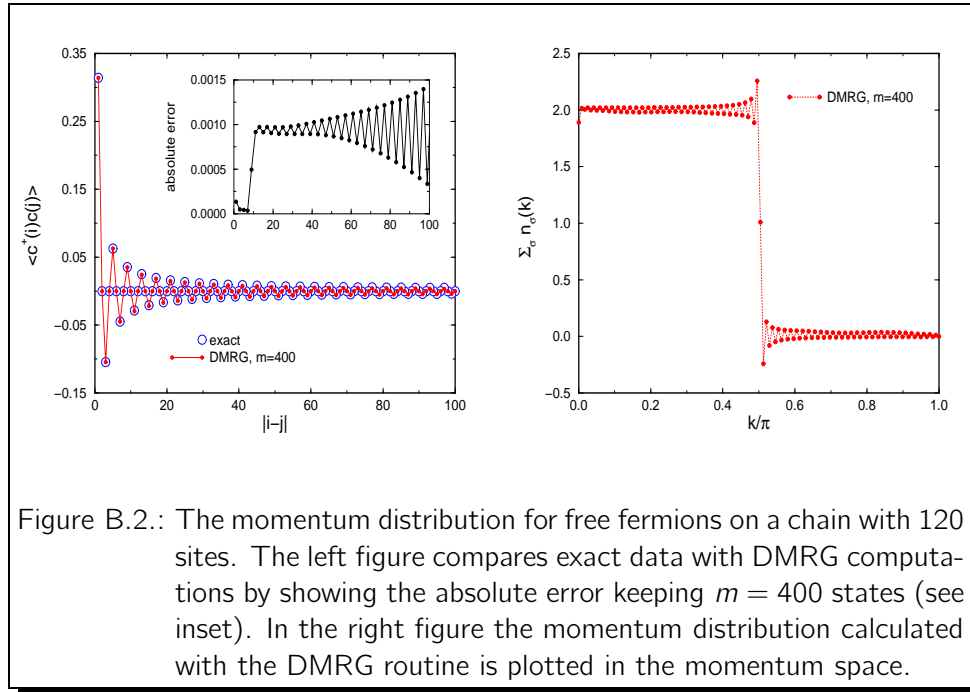$$C_{CDW}^{free}(r) \equiv n^2 - 2\langle q_r \rangle^2 \,. \tag{B.8}$$

The propagator $\langle q_r \rangle$ can be calculated in the following way [142]: Let $|\ell\rangle$ be a state at site ℓ. Then the corresponding orthonormal momentum states read

$$|k_m\rangle = \sqrt{\frac{2}{L+1}} \sum_{\ell=1}^{L+1} \sin(k_m \ell)|\ell\rangle \,, \tag{B.9}$$

where the discret momenta take the values $k_m = \pi m/(L+1)$ with $m = 1, \ldots, N_\sigma/L$. The propagator is then given by

$$\langle k_m | q_r | k_m' \rangle = \frac{2}{L+1} \sin(k_m\, i) \sin(k_m'\, j) \tag{B.10}$$

In the following figures we diplay various correlation functions of the free fermion model (B.1) and compare the exact results with the DMRG results. Note that already 400 states lead to a good agreement with the exact results.

Figure B.2.: The momentum distribution for free fermions on a chain with 120 sites. The left figure compares exact data with DMRG computations by showing the absolute error keeping $m = 400$ states (see inset). In the right figure the momentum distribution calculated with the DMRG routine is plotted in the momentum space.
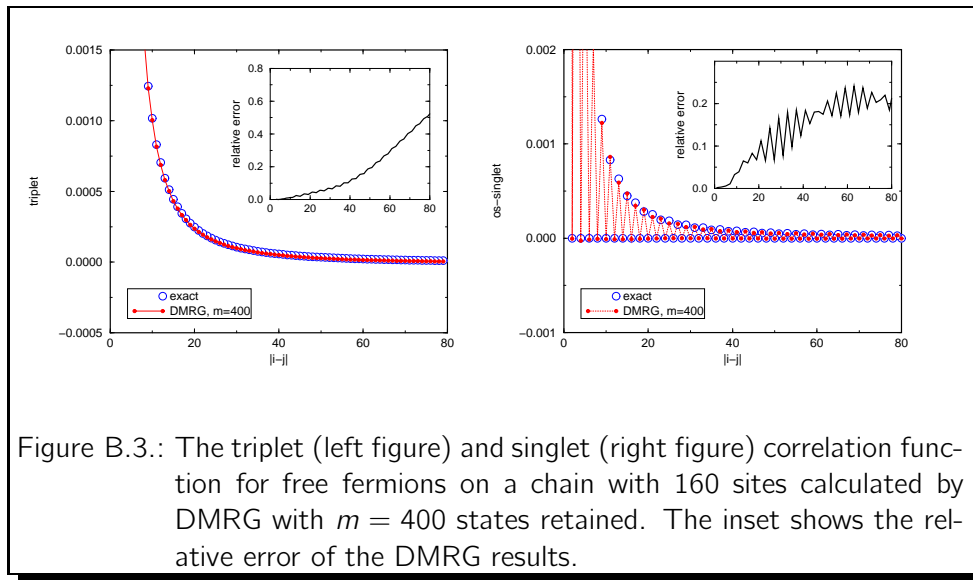
Figure B.3.: The triplet (left figure) and singlet (right figure) correlation function for free fermions on a chain with 160 sites calculated by DMRG with $m = 400$ states retained. The inset shows the relative error of the DMRG results.
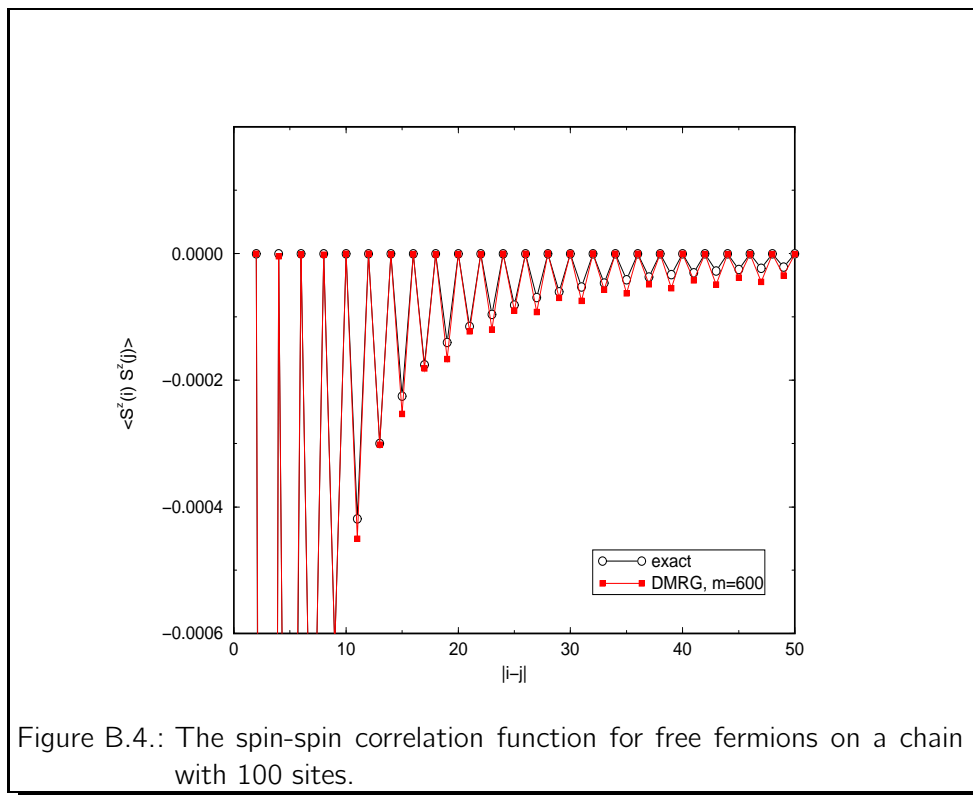

Figure B.4.: The spin-spin correlation function for free fermions on a chain with 100 sites.

Bibliography

[1] L. D. Landau, Sov. Phys. JETP **3**, 920 (1957).

[2] L. D. Landau, Sov. Phys. JETP **5**, 101 (1957).

[3] L. D. Landau, Sov. Phys. JETP **8**, 70 (1958).

[4] F. D. M. Haldane, Phys. Rev. Lett. **47**, 1840 (1981).

[5] S. Tomonaga, Prog. Theor. Phys. **5**, 544 (1950).

[6] J. M. Luttinger, J. Math. Phys. **4**, 1154 (1963).

[7] D. C. Mattis and E. H. Lieb, J. Math. Phys. **6**, 304 (1965).

[8] A. Luther and V. J. Emery, Phys. Rev. Lett. **33**, 589 (1974).

[9] J. Sólyom, Adv. Phys. **28**, 209 (1979).

[10] A. O. Gogolin, A. A. Nersesyan, and A. M. Tsvelik, *Bosonization and Strongly Correlated Systems*, Cambridge University Press, Cambridge, 1998.

[11] M. Quaisser, *Untersuchungen zu Fermionenmodellen mit korreliertem Hüpfen in niedrigen Dimensionen*, PhD thesis, Universität Köln, 1995.

[12] H. J. Schulz, Phys. Rev. Lett. **64**, 2831 (1990).

[13] N. D. Mermin and H. Wagner, Phys. Rev. Lett. **17**, 1133 (1966).

[14] S. Takada, Prog. Theor. Phys. **54**, 1039 (1975).

[15] J. Voit, Rep. Prog. Phys. **57**, 977 (1994).

[16] N. Kawakami and S. K. Yang, Phys. Rev. B **44**, 7844 (1991).

[17] H. Frahm and V. E. Korepin, Phys. Rev. B **42**, 10553 (1990).

[18] K. Bechgaard, C. S. Jacobsen, K. Mortensen, H. J. Pedersen, and N. Thorup, Solid St. Commun. **33**, 1119 (1980).

[19] D. Jérome, A. Mazaud, M. Ribault, and K. Bechgaard, J. Phys. Lett., Paris **41** (1980).

[20] K. Bechgaard, K. Carneiro, M. Olsen, and F. B. Rasmussen, Phys. Rev. Lett. **46**, 852 (1981).

[21] H. Wilhelm et al., Eur. Phys. J. B **21**, 175 (2001).

[22] J. Hubbard, Proc. Roy. Soc. A **276**, 238 (1963).

[23] M. C. Gutzwiller, Phys. Rev. Lett. **10**, 159 (1963).

[24] J. Kanamori, Prog. Theor. Phys **30**, 275 (1963).

[25] J. G. Bednorz and K. A. Müller, Z. Phys. B **64**, 189 (1986).

[26] P. W. Anderson, Science **235**, 1196 (1987).

[27] F. C. Zhang and T. M. Rice, Phys. Rev. B **37**, 3759 (1988).

[28] H. Tasaki, J. Phys.: Condens. Matter **10**, 4353 (1998).

[29] Y. Nagaoka, Phys. Rev. **147**, 392 (1966).

[30] H. Tasaki, Phys. Rev. B **40**, 9192 (1989).

[31] A. Mielke and H. Tasaki, Commun. Math. Phys. **158**, 341 (1993).

[32] E. H. Lieb, Phys. Rev. Lett. **62**, 1201 (1989).

[33] U. Brandt and A. Giesekus, Phys. Rev. Lett. **68**, 2648 (1992).

[34] M. Kollar, R. Strack, and D. Vollhardt, Phys. Rev. B **53**, 9225 (1996).

[35] C. N. Yang, Phys. Rev. Lett. **63**, 2144 (1989).

[36] R. Strack and D. Vollhardt, Phys. Rev. Lett. **70**, 2637 (1993).

[37] J. de Boer, V. E. Korepin, and A. Schadschneider, Phys. Rev. Lett. **74**, 789 (1995).

[38] E. H. Lieb, *Advances in Dynamical Systems and Quantum Physics*, page 173, World Scientific, Singapore, 1995.

[39] A. Montorsi, *The Hubbard Model – A Reprint Volume*, World Scientific, Singapore, 1992.

[40] M. Rasetti, *The Hubbard Model, Recent Results*, World Scientific, Singapore, 1991.

[41] D. Baeriswyl, D. K. Campbell, J. M. P. Carmelo, F. Guinea, and E. Louis, *The Hubbard Model: Its Physics and Mathematical Physics*, Plenum Press, New York, 1995.

[42] C. N. Yang and S. C. Zhang, Mod. Phys. Lett. B **4**, 759 (1990).

[43] C. N. Yang, Phys. Rev. Lett. **19**, 1312 (1967).

[44] E. H. Lieb and F. Y. Wu, Phys. Rev. Lett. **20**, 1445 (1968).

[45] M. Takahashi, Prog. Theor. Phys. **47**, 69 (1972).

[46] M. Takahashi, Prog. Theor. Phys. **52**, 103 (1974).

[47] F. Woynarovich, J. Phys. C **15**, 85 (1982).

[48] F. Woynarovich, J. Phys. C **15**, 97 (1982).

[49] F. Woynarovich, J. Phys. C **16**, 5293 (1983).

[50] F. Woynarovich, J. Phys. C **16**, 6593 (1983).

[51] A. Ovchinnikov, Soviet Phys. JETP **30**, 1160 (1970).

[52] C. Coll, Phys. Rev. B **9**, 2150 (1974).

[53] A. Klümper, A. Schadschneider, and J. Zittartz, Z. Phys. B **78**, 99 (1990).

[54] F. H. L. Eßler and V. E. Korepin, Phys. Rev. Lett. **72**, 908 (1994).

[55] B. S. Shastry, Phys. Rev. Lett. **56**, 2453 (1986).

[56] M. Shiroishi and M. Wadati, J. Phys. Soc. Jpn. **64**, 57 (1995).

[57] P. B. Ramos and M. J. Martins, J. Phys. A **30** (1997).

[58] G. Jüttner, A. Klümper, and J. Suzuki, Nucl. Phys. B **512**, 581 (1998).

[59] F. H. L. Eßler and V. E. Korepin, *Exactly Solvable Models of Strongly Correlated Electrons*, World Scientific, Singapore, 1994.

[60] T. Deguchi et al., Phys. Rep. **331**, 197 (2000).

[61] R. J. Baxter, *Exactly Solved Models in Statistical Mechanics*, Academic Press, London, 1982.

[62] H. Schulz, J. Phys. C **18**, 581 (1985).

[63] H. Asakawa and M. Suzuki, J. Phys. A **29**, 225 (1996).

[64] T. Deguchi and R. Yue, cond-mat/9704138.

[65] M. Shiroishi and M. Wadati, J. Phys. Soc. Japan **66**, 1 (1997).

[66] G. Bedürftig, B. Brendel, H. Frahm, and R. M. Noack, Phys. Rev. B **58**, 10225 (1998).

[67] see e.g. `http://www.vni.com/products/imsl`.

[68] V. J. Emery, *Highly Conducting One-Dimensional Solids*, page 327, Plenum Press, New York, 1979.

[69] J. Voit, Phys. Rev. B **45**, 4027 (1992).

[70] J. E. Hirsch, Phys. Rev. Lett. **53**, 2327 (1984).

[71] K. Penc and F. Mila, Phys. Rev. B **49**, 9670 (1994).

[72] H. Q. Lin, E. R. Gagliano, D. K. Campbell, E. H. Fradkin, and J. E. Gubernatis, *The Hubbard Model – Its Physics and Mathematical Physics*, page 315, Plenum Press, New York, 1995.

[73] S. Kneer, *Dichte-Matrix Renormierungsgruppen Analyse am eindimensionalen extended Hubbard-Modell*, Diplomarbeit, Universität Würzburg, 1997.

[74] M. Nakamura, Phys. Rev. B **61**, 16377 (2000).

[75] J. E. Hirsch, Phys. Lett. A **134**, 452 (1989).

[76] J. E. Hirsch, Physica C **158**, 326 (1989).

[77] R. Bariev, J. Phys. A: Math. Gen. **24** (1991).

[78] A. Schadschneider, Phys. Rev. B **51**, 10386 (1995).

[79] M. Quaisser, A. Schadschneider, and J. Zittartz, Europhys. Lett. **32**, 179 (1995).

[80] L. Arrachea and A. A. Aligia, Phys. Rev. Lett. **73**, 2240 (1994).

[81] F. Dolcini and A. Montorsi, Phys. Rev. B **66**, 75112 (2002).

[82] A. Kemper, *Transfermatrix-DMRG for dynamics of stochastic models and thermodynamics of fermionic models*, PhD thesis, Universität Köln, 2003.

[83] A. Kemper and A. Schadschneider, Phys. Rev. B **68**, 235102 (2003).

[84] P. A. Bares and G. Blatter, Phys. Rev. Lett. **64**, 2567 (1990).

[85] N. Kawakami and S. K. Yang, Phys. Rev. Lett. **65**, 2309 (1990).

[86] C. S. Hellberg and E. J. Mele, Phys. Rev. B **48**, 646 (1993).

[87] M. Ogata, M. U. Luchini, S. Sorella, and F. F. Asaad, Phys. Rev. Lett. **66**, 2388 (1991).

[88] M. Nakamura, K. Nomura, and A. Kitazawa, Phys. Rev. Lett. **79**, 3214 (1997).

[89] E. Anderson et al., *LAPACK Users' Guide*, SIAM, 1995.

[90] C. Lanczös, J. Res. Natl. Bur. Stand. **45**, 255 (1950).

[91] S. R. White, Phys. Rev. Lett. **69**, 2863 (1992).

[92] S. R. White, Phys. Rev. B **48**, 10345 (1993).

[93] M. Suzuki, *Quantum Monte Carlo Methods In Condensed Matter Physics*, World Scientific, Singapore, 1993.

[94] I. Peschel, X. Wang, M. Kaulke, and K. Hallberg, *Density-Matrix Renor-malization – A New Numerical Method in Physics*, Lecture Notes in Physics 528, Springer, Berlin, 1999.

[95] K. G. Wilson, Phys. Rev. B **4**, 3174 (1971).

[96] K. G. Wilson, Rev. Mod. Phys. **47**, 773 (1975).

[97] J. W. Bray and S. T. Chui, Phys. Rev. B **19**, 4876 (1979).

[98] T. Xiang and G. A. Gehring, Phys. Rev. B **48**, 303 (1993).

[99] R. Raupach, *On the spin-Peierls phase transition of frustrated Heisenberg chains*, PhD thesis, Universität Köln, 2000.

[100] F. Zhang, *Matrix Theory, Basic Results and Techniques*, Springer, 1999.

[101] L. Chen and S. Moukouri, Phys. Rev. B **53**, 1866 (1995).

[102] S. Moukouri and L. G. Caron, Phys. Rev. Lett. **77**, 4640 (1996).

[103] I. Peschel, M. Kaulke, and O. Legeza, Ann. Physik (Lpz.) **8**, 153 (1999).

[104] K. Hamacher, *Untersuchung quantenmechanischer Korrelationseffekte mit der Dichtematrix-Renormierungsgruppe*, PhD thesis, Universität Dortmund, 2001.

[105] E. R. Davidson, J. Comput. Phys. **17**, 87 (1975).

[106] U. Schollwöck, Phys. Rev. B **58**, 8194 (1998).

[107] U. Schollwöck, Phys. Rev. B **59**, 3917 (1999).

[108] S. R. White, Phys. Rev. Lett. **77**, 3633 (1996).

[109] R. M. Noack, S. R. White, and D. J. Scalapino, Phys. Rev. Lett. **73**, 882 (1994).

[110] S. Östlund and S. Rommer, Phys. Rev. Lett. **75**, 3537 (1995).

[111] A. Klümper, A. Schadschneider, and J. Zittartz, Z. Phys. B **87**, 281 (1992).

[112] H. Niggemann, *Exact ground states for one- and two-dimensional quantum spin systems*, PhD thesis, Universität Köln, 1998.

[113] M. A. Ahrens, *Exakte Grundzustände der Spin-2-Kette*, Diplomarbeit, Universität Köln, 2001.

[114] E. Bartel, *Numerische Untersuchungen von Spin-1-Ketten*, Diplomarbeit, Universität Köln, 2002.

[115] E. Jeckelmann and S. R. White, Phys. Rev. B **57**, 6376 (1998).

[116] K. A. Hallberg, Phys. Rev. B **52** (1995).

[117] T. D. Kühner and S. R. White, Phys. Rev. B **60**, 335 (1999).

[118] E. Jeckelmann, Phys. Rev. B **66**, 45114 (2002).

[119] T. Xiang, Phys. Rev. B **53** (1996).

[120] P. Henelius, Phys. Rev. B **60**, 9561 (1999).

[121] T. Xiang, J. Lou, and Z. Su, Phys. Rev. B **64**, 104414 (2001).

[122] S. Moukouri and L. G. Caron, Phys. Rev. B **67**, 92405 (2003).

[123] S. Nishimoto, E. Jeckelmann, F. Gebhard, and R. M. Noack, Phys. Rev. B **65**, 165114 (2002).

[124] T. Nishino, J. Phys. Soc. Jpn. **64**, 3598 (1995).

[125] X. Wang and T. Xiang, Phys. Rev. B **56**, 5061 (1997).

[126] A. P. Mackenzie and Y. Maeno, Rev. Mod. Phys. **75**, 657 (2003).

[127] S. S. Saxena et al., Nature **406**, 587 (2001).

[128] C. Pfleiderer et al., Nature **412**, 58 (2001).

[129] S. E. Brown, M. J. Naughton, I. J. Lee, E. I. Chashechkina, and P. M. Chaikin, *More is Different: Fifty Years of Condensed Matter Physics*, page 151, Princeton Series in Physics, 2001.

[130] E. Dagotto, Rev. Mod. Phys. **66**, 763 (1994).

[131] H. Mukuda et al., Physica B **944**, 259 (1999).

[132] G. I. Japaridze and E. Müller-Hartmann, Phys. Rev. B **61**, 9019 (1999).

[133] I. Affleck and J. B. Marston, J. Phys. C **21**, 2511 (1988).

[134] K. A. Penson and M. Kolb, Phys. Rev. B **33**, 1663 (1986).

[135] A. Hui and S. Doniach, Phys. Rev. B **48**, 2063 (1993).

[136] A. Sikkema and I. Affleck, Phys. Rev. B **52**, 10207 (1995).

[137] K. A. Muttalib and V. J. Emery, Phys. Rev. Lett. **57**, 1370 (1986).

[138] T. Giamarchi and H. J. Schulz, Phys. Rev. B **33**, 2066 (1986).

[139] E. H. Lieb, T. Schulz, and D. Mattis, Ann. Phys. (N.Y.) **16**, 417 (1961).

[140] K. A. Hallberg, P. Horsch, and G. Martinez, Phys. Rev. B **52** (1995).

[141] S. Katsura, Phys. Rev. **127**, 1508 (1962).

[142] C. Kollath and U. Schollwöck, private communications.

Danksagungen

□ Zunächst danke ich Herrn Prof. Dr. J. Zittartz herzlich, der die Durchführung der vorliegenden Arbeit ermöglicht und unterstützt hat.

□ Desweiteren möchte ich Herrn Priv.-Doz. Dr. A. Schadschneider für die wissenschaftliche Betreuung der Arbeit und für die unzähligen Hinweise und Tips während der guten Zusammenarbeit danken.

□ Besonderer Dank gilt Frau Corinna Kollath, Herrn Prof. Dr. U. Schollwöck und Herrn Prof. Dr. G. I. Japaridze, deren zahlreiche Hilfestellungen die Entwicklung dieser Arbeit vorangebracht haben. Insbesondere die Zusammenarbeit mit Herrn Prof. Dr. G. I. Japaridze lieferte wichtige Bestandteile dieser Arbeit.

□ Bei meinen Kollegen, insbesondere Marc André Ahrens, Erik Bartel, Dr. Andreas Kemper, Dr. Ansgar Kirchner, Alireza Namazi und Dr. Frank Zielen bedanke ich mich ganz herzlich für die angenehme Arbeitsatmosphäre und für die diversen Aktivitäten jenseits der Wissenschaft. In diesem Zusammenhang danke ich auch der Fussballmannschaft des Instituts.

□ Den Korrektoren Erik Bartel und Dr. Andreas Kemper danke ich für die Durchsicht des Manuskripts und den damit verbundenen Zeitaufwand.

□ Ganz herzlich möchte ich mich bei meinen Eltern bedanken, die mein langes Studium überhaupt erst ermöglicht haben und mich in jeder Hinsicht unterstützten.

□ Schließlich danke ich ganz besonders meiner Freundin Nina für die schönen Stunden jenseits der Arbeit und für ihre Geduld während der Entstehung dieser Arbeit.

English Abstract

In the present work the numerical density matrix renormalization group (DMRG) algorithm is used to analyze the ground state properties of the Hubbard model with transverse spin-exchange.

The DMRG algorithm, which was developed by White in 1992, is based on the following simple but effective concept: the ground-state wavefunction as well as the low energy excitations of a large interacting chain are obtained by increasing the lattice size iteratively, starting with a small one that can be diagonalized exactly. The exponentially growing Hilbert space is controlled by a renormalization procedure in which 'less important' degrees of freedom are integrated out.

Motivated by recent experimental findings showing evidence for the competition or even coexistence of triplet superconductivity and ferromagnetism we focused our investigations on a rather simple extension of the Hubbard model including transverse spin exchange between electrons on nearest-neighbour sites.

In the half-filled case, we showed that the phase diagram obtained in the weak-coupling limit has to be modified. A new phase, described by spin and charge excitation gap, shows long-range order in the longitudinal spin correlation, whereas superconducting correlations are surpressed and decay exponentially as expected for the case of a finite charge gap.

In general, the presence of a repulsive on-site Coulomb interaction U leads to an enlargement of the sectors with nonvanishing charge gap at the expense of the sectors with spin gap.

We extend our analysis to the case of a quarter-filled band. Depending on the value $J_\perp/t$ the model belongs either to a gapless excitation phase or to a spin gapped phase with gapless charge degrees of freedom.

Deutsche Kurzzusammenfassung

In der vorliegenden Arbeit verwendeten wir den Algorithmus der Dichte-Matrix-Renormierungsgruppe (DMRG), um Grundzustandseigenschaften des Hubbard-Models mit transversalem Spin-Austausch zu analysieren.

Dem DMRG-Algorithmus, der 1992 von White entwickelt wurde, liegt ein einfaches, aber sehr effektives Konzept zugrunde: die Grundzustands-Wellenfunktion sowie die tiefliegenden Anregungen einer groen, wechselwirkenden Kette erhält man durch sukzessiver Verlängerung einer kurzen, exakt diagonalisierbaren Kette. Der hierbei exponentiell anwachsende Hilbertraum wird mit Hilfe einer Renormierungsprozedur, die 'weniger wichtige' Freiheitsgrade ausintegriert, kontrolliert.

Neue, experimentell gewonnene Daten weisen auf eine Konkurrenz oder sogar eine Koexistenz von Triplet-Supraleitung und Ferromagnetismus hin. Geleitet von diesen Ergebnissen konzentrierten wir unsere Untersuchungen auf eine elementare, generische Art des Hubbard-Models mit transversalem Spin-Austausch zwischen Elektronen benachbarter Gitterplätze, das ein reichhaltiges Phasendiagramm aufweist.

Für das halbgefllte Band konnten wir zeigen, dass das Phasendiagram, berechnet im Limes schwacher Kopplung, modifiziert werden muss. Eine neue Phase charakterisiert durch Spin- und Ladungs-Lücke weist langreichweitige Anregungen in der longitudinalen Spin-Korrelationsfunktion, wohingegen supraleitende Korrelationen exponentiell abfallen.

Im Allgemeinen führt die Präsenz einer repulsiven 'on-site' Coulomb-Wechselwirkung zur Ausdehnung der Sektoren mit nicht-verschwindender Ladungslücke auf Kosten von Sektoren mit einer Spinanregungslücke.

Wir erweiterten unsere Untersuchung für den Fall des viertelgefüllten Bandes. Abhängig von $J_\perp/t$ wird das Modell entweder durch eine Phase mit lückenloser Energieanregung beschrieben oder es gehört einer Phase an, die durch eine Spinanregungslücke charakterisiert ist.

Erklärung

Ich versichere, dass ich die von mir vorgelegte Dissertation selbständig angefertigt, die benutzten Quellen und Hilfsmittel vollständig angegeben und die Stellen der Arbeit – einschließlich Tabellen, Karten und Abbildungen –, die anderen Werken im Wortlaut oder Sinn nach entnommen sind, in jedem Einzelfall als Entlehnung kenntlich gemacht habe; dass diese Dissertation noch keiner anderen Fakultät oder Universität zur Prüfung vorgelegen hat; dass sie – abgesehen von unten angegebenen Teilpublikationen – noch nicht veröffentlicht worden ist, dass ich eine solche Veröffentlichung vor Abschluss des Promotionsverfahrens nicht vornehmen werde. Die Bestimmungen dieser Promotionsordnung sind mir bekannt. Die von mir vorgelegte Dissertation ist von Herrn Prof. Dr. Johannes Zittartz betreut worden.

Köln, den 16. März 2004

Teilpublikationen

1. C. Dziurzik, A. Schadschneider, J. Zittartz, *Optimum ground states of generalized Hubbard models with next-nearest neighbour interaction*, Eur. Phys. J. B **12**, Seite 209 (1999)

2. C. Dziurzik, G. J. Japaridze, A. Schadschneider, J. Zittartz, *Triplet superconductivity vs. easy-plane ferromagnetism in a 1D itinerant electron system with transverse spin anisotropy*, zur Veröffentlichung eingereicht bei Eur. Phys. J. B

3. C. Dziurzik, G. J. Japaridze, A. Schadschneider, J. Zittartz, *Triplet superconductivity in a 1D Luther-Emer liquid*, in Vorbereitung

Lebenslauf

Persönliche Daten

Name:	Christian Dziurzik
Geburtsdatum:	12. Juli 1969
Geburtsort:	Dramatal (Polen)
Familienstand:	ledig
Staatsangehörigkeit:	deutsch

Schulbildung

1976–1981	Grundschule
1982–1987	Max-Planck-Realschule in Köln-Porz
1988–1991	Stadtgymnasium Köln-Porz

Hochschulstudium

10/1992–09/1998	Studium der Physik an der Universität zu Köln
	Diplomarbeit am Institut für Theoretische Physik über *Exakte Grundzustände von verallgemeinerten Hubbard-Modellen*
seit 10/1998	Promotion am Institut für Theoretische Physik an der Universität zu Köln

Wissenschaftliche Anstellungen

10/1997–09/1998	Studentische Hilfskraft am Institut für Theoretische Physik der Universität zu Köln
10/1998–07/1999	Wissenschaftliche Hilfskraft am Institut für Theoretische Physik der Universität zu Köln
seit 08/1999	Wissenschaftlicher Mitarbeiter am Institut für Theoretische Physik der Universität zu Köln